

Diss. ETH No. 23885

**Adaptive matching of radiofrequency
transmitters for magnetic resonance imaging**

A dissertation submitted to
ETH ZURICH

for the degree of
DOCTOR OF SCIENCES

presented by
Georgios Katsikatsos
M.Sc. ETH Zurich,
Dipl.-Eng. Aristotle University of Thessaloniki
born on May 2nd, 1981
citizen of Hellenic Republic

accepted on the recommendation of
Prof. Dr. Klaas P. Pruessmann, examiner
Prof. Dr. Harald H. Quick, co-examiner

Zurich 2016

*Μην καταδέχεσαι να ρωτάς: «Θα νικήσουμε; Θα νικηθούμε;»
Πολέμα.*

Νίκος Καζαντζάκης, «Ασκητική»

Summary

The trend in magnetic resonance imaging (MRI) towards higher static field strengths is urged by the derived surplus of signal-to-noise ratio (SNR). Yet, the higher field strength reduces the radiofrequency (RF) wavelength to dimensions proportionate to the human body, raising wave phenomena in it. This complex behavior is patient-specific, it degrades the uniformity of the excitation fields and impairs the contrast of the MR images. The use of multiple independent transmitters introduces spatial degrees of freedom to generate RF pulses tailored for the imaging anatomy. However, in the increasing working frequency, the quasi-static approximation assumed for the coils is gradually violated, rendering coils sensitive to load variations and, consequently, altering their electrical characteristics. Correcting the consequent transmission inefficiency by adaptive electric networks is of great importance.

The present work addresses the issue of coil array inefficiency by applying novel array matching methods. Based on a novel variable capacitor module, a set of optimization criteria is explored for performing array matching by employing capacitor-specific intelligence that comes in the form of position dependent scattering parameters.

In the lack of the appropriate tools and in the need to develop equipment to enable research in the field, the novel high-power and low-loss variable capacitor is presented. It is actuated by a piezoelectric motor and positioned accurately by an optical encoder. The contradicting requirements for large range, small size and high power handling are resolved by the use of a high permittivity dielectric

material with high dielectric strength. The planar design offers increased per unit area of electrode, leading to reduced demand on the material permittivity. A drawback of high permittivity is the exerted stress in terms of voltage holding at the material boundaries, where electric field may build up greatly. Accounting for this phenomenon, electrode shapes are rounded and a thin film of dielectric material is applied to mitigate the extreme electric field at these boundaries. After assembling the capacitor module, its electrical characteristics are verified and the scattering parameters are stored in the form of lookup tables. These are used to analytically calculate, in scattering parameter nomenclature, the condition of reflectionless matching for a single channel case. The matching strategy performance was evaluated with MR-based methods both *in-vitro* and *in-vivo*.

The modularity of the design enables the synthesis of networks capable of performing matching of multiple coil elements concurrently. Nevertheless, multi-channel matching poses hardware and algorithmic challenges. Coupling between array elements enables additional pathways for power to be scattered and dissipated. The matching system is compelled to tackle the complexity by introducing control over these pathways. The necessary degrees of freedom grow quadratically with the number of coil elements, rendering the approach for reasonably sized coil arrays prohibitive. A radiofrequency device that blends or isolates the signals at its input, called Butler matrix, is introduced to decouple the array elements, thus reducing the otherwise necessary cross-element adaptivity. To this end, two layers of matching networks surround the Butler matrix in order to match the system. The complexity of the necessary adaptive elements for the proposed system is of linear order, making the problem computationally tractable. Alongside, a matching algorithm introduces two novel matching strategies and elements of randomization. The matching strategies account for the losses in the matching network and for the power maximization to the load, while randomization aims to reduce the optimization space size.

The algorithmic aspects of the proposed methods are evaluated in a next step. The dimensionality of the derived system motivated its exploration in terms of efficiency. A Monte Carlo simulation was employed to provide insights to the behavior of the matching system for the proposed objective functions. On one hand, visualizations of a reduced space prove the complexity of the matching problem, while revealing ways of algorithmic optimization. On the other hand, statistics about the algorithmic performance advocate for the application of the proposed objective functions in terms of matching efficiency and convergence speed.

Finally, the coil array matching performance was investigated for typical loading scenarios. The array matching methods, based on the prior knowledge stored in the lookup tables and guided by the proposed algorithm and optimization criteria, were validated *in-vitro*. The newly introduced optimization criteria outperform the conventional method of reflection minimization in the holistic array matching approach. For completeness, the conventional method of per-port reflection minimization with the absence of the Butler matrix was performed as well. The per-port matching also improves matching performance. The marginal gains of the conventional against the holistic method indicate the presence of losses in the matching network.

In conclusion, this work fills a technology gap for efficient array transmission by developing novel instrumentation and methodology for performing adaptive array matching.

Zusammenfassung

Der Trend in der Magnetresonanztomographie (MRT) zu höheren statischen Feldstärken ist motiviert durch den Gewinn im Signal-Rausch-Verhältnis (SNR). Eine höhere Feldstärke führt zu reduzierter Radiofrequenz-(RF) Wellenlänge, die in der Grössenordnung des menschlichen Körpers liegt und damit zu Wellenphänomenen im Körper führen kann. Dieses komplexe Verhalten ist patientenspezifisch und verschlechtert die Homogenität der Anregungsfelder, was sich negativ auf den Kontrast in MR-Bildern auswirkt. Die Verwendung mehrerer unabhängiger Sender führt zu zusätzlichen räumlichen Freiheitsgraden und erlaubt die Erzeugung von RF-Pulssequenzen je nach Anatomie. Die Annahme eines quasistatischen Operationsregimes der Spulen wird jedoch mit zunehmender Arbeitsfrequenz allmählich verletzt. Spulen reagieren empfindlich auf Lastveränderungen, die ihre elektrischen Eigenschaften verändern, was unter anderem zu ineffizienter Energieübertragung führt. Die Korrektur der sich daraus ergebenden Sendeeffizienzeinbussen mittels elektrischer Anpassungsnetzwerke ist demnach von grosser Bedeutung.

Die vorliegende Arbeit beschäftigt sich mit der Effizienzverbesserung von Spulenarrays durch die Anwendung neuartiger Anpassungsmethoden. Basierend auf einem neuartigen variablen Kondensatormodul wird eine Auswahl an Optimierungskriterien zur Array-Anpassung erforscht. Dazu werden kondensatorspezifische Eigenschaften, hier in der Form von positionsabhängigen Streuparametern, angewendet.

In Ermangelung von geeigneten Instrumenten und des Bedarfs, neue Geräte für die Forschung in diesem Gebiet zu entwickeln, wird der

neuartige verlustarme und variable Hochleistungskondensator vorge stellt. Er wird von einem piezoelektrischen Motor angetrieben und präzise optisch positioniert. Die unvereinbaren Anforderungen an einen grossen Wertebereich, kleine Grösse und hohe Belastbarkeit werden durch die Verwendung eines dielektrischen Materials mit hoher Dielektrizitätskonstante und Dielektrizitätsfestigkeit gelöst. Das planare Design bietet eine erhöhte Elektrodendichte pro Flächeneinheit, was zu einer verringerten Bedarf an Dielektrizität des Materials führt. Ein Nachteil von einer hohen Dielektrizitätskonstante ist die Belastung im Hinblick auf Spannungsfestigkeit an den Grenzen des Materials, wo sich starke elektrische Felder aufbauen können. Um dieses Problem zu berücksichtigung, werden Elektroden abgerundet und ein dünner Film aus dielektrischem Material wird aufgetragen, sodass extreme elektrische Felder an diesen Grenzen reduziert werden können. Nach der Montage des Kondensatormoduls, werden dessen elektrische Eigenschaften überprüft und die Streuparameter in Form von Look-up Tabellen gespeichert. Die Tabellen werden verwendet, um den Zustand der reflexionsfreien Anpassung für den Fall des Einzelkanals in der Streuparameter-Nomenklatur analytisch zu berechnen. Die Leistungsfähigkeit der Anpassungsstrategie wurde anhand von MR-basierten Methoden sowohl *in-vitro* als auch *in-vivo* evaluiert.

Die Modularität des Entwurfs ermöglicht die Synthese von Netzwerken, welche zur gleichzeitigen Anpassung von mehreren Spulenelementen fähig sind. Die Mehrkanal-Anpassung stellt allerdings Herausforderungen in Bezug auf die Hardware und die Algorithmen. Kopplung zwischen Spulenelementen führt zur Bildung von Leistungspfaden, welche Streuung und Verluste verursachen. Das Anpassungssystem bewältigt diese Komplexität durch die Einführung von Kontrollmechanismen für diese Pfade. Die Anzahl der erforderlichen Freiheitsgrade nimmt quadratisch mit der Anzahl der Spulenelemente zu. Dies hat zur Folge, dass der Entwurf für realistische Spulengrössen untragbar wird. Ein Radiofrequenzgerät, die so genannte

Butler-Matrix, welches die Signale an seinem Eingang mischt oder trennt, wird zwecks Entkopplung der Arrayelemente eingeführt. Somit wird die sonst erforderliche Adaptivität der Zwischenelemente reduziert. Demnach umgeben zwei Schichten von Anpassungsnetzwerke die Butler-Matrix, sodass das System angepasst wird. Die Komplexität der notwendigen adaptiven Elemente des vorgeschlagenen Systems ist linearer Ordnung, was dazu führt, dass das Problem rechnerisch lösbar wird. Des Weiteren, führt ein Anpassungsalgorithmus zwei neue Anpassungsstrategien mit randomisierten Elementen ein. Diese berücksichtigen die Verluste im Anpassungsnetzwerk und die Maximierung der Leistungslieferung an die Last. Die Randomisierung zielt auf die Verringerung der Grösse des Optimierungsraum ab.

Die algorithmischen Aspekte der vorgeschlagenen Methoden wurden in einem nächsten Schritt evaluiert. Die Dimensionalität des resultierenden Systems motivierte seine Untersuchung hinsichtlich der Effizienz. Eine Monte-Carlo-Simulation wurde eingesetzt, um Erkenntnisse über das Verhalten des Anpassungssystems für die vorgeschlagenen Zielfunktionen gewinnen zu können. Auf der einen Seite, weisen Visualisierungen des reduzierten Raumes die Komplexität des Anpassungsproblems nach, während sie Hinweise zur algorithmische Optimierung liefern. Auf der anderen Seite, befürworten Statistiken bezüglich der algorithmischen Leistungsfähigkeit die Anwendung der vorgeschlagenen Zielfunktionen hinsichtlich Anpassungseffizienz und Konvergenzgeschwindigkeit.

Abschliessend wurde die Leistungsfähigkeit der Spulenarrayanpassung anhand typischer Belastungsszenarien untersucht. Die Arrayanpassungsmethoden, welche auf Vorwissen in den Look-up Tabellen basieren und welche vom vorgeschlagenen Algorithmus und den Optimierungskriterien abhängen, wurden *in-vitro* validiert. Die neu eingeführten Optimierungskriterien übertreffen die konventionelle Methode der Reflexionsminierung im ganzheitlichen Arrayan-

passungsansatz. Der Vollständigkeits halber wurde die konventionelle Methode der pro-Port Reflexionsminimierung ohne die Butler-Matrix auch ausgeführt. Die pro-Port Anpassung verbessert ebenfalls die Anpassungsleistungsfähigkeit. Die geringfügige Gewinne der konventionellen Methode gegenüber der ganzheitlichen Methode deuten auf die Präsenz von Verlusten im Anpassungssystem hin.

Zusammenfassend kann man sagen, dass die vorliegende Arbeit eine technologische Lücke der Effizienz von Arraysendens durch die Entwicklung von neuen Geräten und Methodologien für die adaptive Arrayanpassung überbrückt.

Acknowledgements

The present work was realized due to the generous support of numerous people, who, either deliberately or not, paved the way for its completion. My gratitude for their invaluable aid, from the bare scientific matters to the important life lessons, will hopefully be re-funded throughout the life long journey.

At first I would like to gratefully acknowledge Prof. Klaas Prüssmann for his tireless advice and support through the good and the difficult times over the years. His scientific vigor and the posed challenges undoubtedly revamped my personality.

I am grateful to Prof. Harald Quick, co-examiner of this thesis, for his prompt and thorough inspection of the work presented here, along with his valuable feedback.

I feel honored to have worked at the Institute for Biomedical Engineering with exceptional scientists. I am thankful to Dr. David Brunner, Thomas Schmid, Dr. Mustafa Çavuşoğlu, Franciszek Hennel and Dr. Christoph Barmet for their meticulous approach and fruitful discussions.

I would like to deeply thank Roger Lüchinger and Urs Sturzenegger for keeping the scanner site operational with tremendous zeal, Stephan Wheeler for his unceasing support and strenuous passion and diligence for everything mechanical, Michael Wyss for helping me plan experimental scan protocols for my experiments, Dr. Martin Bühner for the prompt support of the reconstruction software, Bruno Willi for keeping the IT infrastructure up and running, Mari-

anne Berg and Isabel Spiess for quietly running administrative issues in the background.

Thank you is not enough to express my gratitude to my fellow office mates Vlad, Dian, Lars, Manuela, Johanna, Max and Hyo for the great atmosphere, companionship, fun and vivid discussions over the years.

I am thankful to the members of the MR group for the resonant environment they created with their distinct personalities at the coffee corner and up in the mountains. Atop, I am deeply indebted to Matteo, Niklaus, Jonas, Josip, Jan, Claudio and Constantin for significantly shaping my scientific rigor, my character and for being good friends. There are no words.

The rest of my dearest friends in Zurich; David, Eliane, Regi, Dimitra, Kostis, Viton, Stavroula, Dimitris, Christos, Anthi, Ilias, Andreas, Kimon, Xenofon, Lena, Giorgos and Zoe. Thank you for everything.

This work is devoted to my family; my sister, Maria, for her enormous support over the years, my parents, Nikos and Clio, for their unconditional love and for providing everything for developing myself and my companion in life, Maria, who means the world to me.

Zürich, May 2017
Georgios Katsikatsos

Contents

Summary	v
Zusammenfassung	viii
1 Introduction	1
1.1 Motivation of the thesis	3
1.2 Contribution of the thesis	5
1.3 Outline	6
2 Fundamental concepts	9
2.1 Radiofrequency fields in MRI	10
2.2 MRI methods	12
2.3 Microwave theory	15
2.4 Matching and decoupling	20
3 Single channel automatic matching	29
3.1 Introduction	30
3.2 Material	32
3.3 Methods	38
3.4 Results	45

3.5	Discussion & Conclusion	53
4	Multiple channel matching system	59
4.1	Multiple channel system description	59
4.2	Objective functions	68
5	Evaluation of matching strategies	75
5.1	Methods	76
5.1.1	Simulation setup	76
5.1.2	Scattering parameter surfaces	77
5.1.3	Monte Carlo simulation metrics	78
5.2	Results	79
5.2.1	Scattering parameter surfaces	79
5.2.2	Monte Carlo simulation results	94
6	Multiple channel matching experiments	105
6.1	Results	107
6.2	Discussion & Conclusion	134
7	Discussion	137
	Appendix	141
A.1	Circulant matrices	141
A.2	Simulation statistics of individual capacitors	143
	Notation	145

List of Figures	147
List of Tables	150
References	151
Curriculum Vitae	161

Chapter 1

Introduction

“There the snow lay around my
doorstep — great heaps of protons
quietly precessing in the earth’s
magnetic field.”

Edward M. Purcell

Magnetic resonance imaging (MRI) is the art of sensing the coherent precession of the magnetic moments or spins of the nuclei in matter in order to obtain tomographic images of significant informational richness. It builds upon the property of nuclei to absorb and re-emit electromagnetic energy when being in an electromagnetic field. This intrinsic property of the nuclear magnetic spins, known as Nuclear Magnetic Resonance (NMR), offers the great opportunity to systematically manipulate them and reveal physical and chemical properties of the matter otherwise inaccessible.

The sensing of the electromagnetic signal emanating from the spins for acquiring tomographic images is preceded by a number of indispensable steps. Initially, the imaging sample is placed in an external, homogeneous static magnetic field, denoted by B_0 . This leads to the polarization of the spin population. The development of the polarization is owed to the distinct states that single spin nuclear

magnetic moments of MR-active nuclei possess due to the Zeeman effect. Hence, spins acquire a set of different orientations at different energy levels. The vectorial sum of the individual magnetic moments results in a macroscopic bulk magnetization.

For the hydrogen nucleus ^1H , the Zeeman splitting results in two spin states, where spins are oriented either parallel or antiparallel to the main magnetic field. The surplus of spins in the lower energy state results in a longitudinal macroscopic net magnetization oriented along the static magnetic field. In the transverse plane perpendicular to B_0 , the spins precess like a spinning top about the axis of the static magnetic field at angular frequency, called Larmor frequency. Nonetheless, the transverse net magnetization remains zero due to their random phase in thermal equilibrium. This state is defined as the steady state of the experiment to follow.

The randomly precessing magnetic moments are irradiated by an electromagnetic field, denoted by B_1^+ . The field oscillates at Larmor frequency and has polarization that coincides with the precessing spins. The exerted radiation carries energy which is absorbed by the spin system. This causes the macroscopic magnetization to be rotated coherently and be forced to precess in the transverse plane. The longitudinal magnetization reduces and the spin system establishes phase coherence in the transverse plane.

After the oscillating B_1^+ -field is switched-off, the magnetization vector relaxes back to the steady state. The recovery of the longitudinal magnetization is described by the time constant T_1 , whereas the time constant of the exponential decay of the transverse magnetization is called T_2 . Several mechanisms influence this transient phenomenon, leading to different relaxation time constants depending on the microscopic environment of the nuclei. The relaxation process by precession of the rotating magnetization of the nuclear spin population results in an oscillating magnetic flux that is measurable by inducing voltage in a conducting loop, called coil in magnetic resonance

experiments.

The phenomenon of inducing coherence in the spin ensemble by proper excitation and the ability to receive electromagnetic signals from it during relaxation to thermal equilibrium was independently observed by Bloch [1] and Purcell et al. [2] in 1946. It is captured by the Bloch equations. Still, it suggests nothing about the way to acquire the MR images we are accustomed to today. In 1973 Lauterbur [3], Mansfield and Grannell [4] and Mansfield [5] established the relationship between frequency encoding and position by superimposing magnetic field gradients onto the static field. In a subsequent step, Kumar et al. [6] introduced frequency analysis to the received signal to obtain the encoded spatial information.

MRI is nowadays of indisputable importance in manifold biological applications, such as medical research and diagnosis. Contrary to other imaging modalities, MRI uses non-ionizing radiation and has large dynamic range for soft-tissue contrast, making it a safe and powerful tomographic technique.

1.1 Motivation of the thesis

Conventionally, the B_1^+ -field that excites the spins is generated by large volume coils. While these fulfill the requirement for field uniformity in the sample, they suffer from reduced sensitivity due to their distance from it. In order to detect the spin signal emanating from the sample efficiently, coil arrays with smaller surface coils placed close to the sample are preferable.

Ideally, the power generated by the amplifier should be transferred to the sample by electromagnetic radiation and used for spin excitation efficiently. The magnitude of the rotating radiofrequency field, B_1^+ , is an essential MR-based figure of merit for efficient power transmission. In low-frequency, single-channel MR coil experiences

negligible load variations owed to the long wavelength. The wave travels through the body nearly unsusceptible to the effects of dielectric boundaries. Thus, the B_1^+ -field is not disturbed significantly. The practical engineering task to maximize power transfer to the load is dealt by microwave networks, called matching networks, inserted between the amplifier and the coil. With these, the impedance of different devices can be matched to the system impedance. For low-field MR systems, existing methods are sufficient, as the conventional approach of maximizing power transfer to the load emanating from the microwave theory is routinely employed with satisfactory results.

MRI machines have always been evolving by a constant increase in static field strength, in the pursuit of higher signal-to-noise ratio (SNR) which can, in turn, be traded for image resolution and image acquisition speed. Currently, an estimate of around 40'000 MRI scanners are installed worldwide with field strengths ranging from ultra-low ($\leq 0.1\text{T}$) to ultra-high (11.75T, [7]) according to [8, 9], with the ultra-high field units ($\geq 4\text{T}$) making up only a small fraction of the whole.

Nevertheless, the shift towards higher magnetic fields comes with new challenges. The dependency between precessional frequency and the magnetic field, fused in the Larmor equation, infers that the wavelength in the working radiofrequency shortens. As a result, the radio waves become comparable to the imaging subject and give rise to wave phenomena within it. Their propagation cannot be assumed quasi-static anymore and reflections and interferences owed to the sudden changes of the dielectric properties of the sample emerge.

Moreover, the lack of the quasi-static property has an immediate effect on the electrical properties of the coil in the event of load variation. Spatial characteristics of the load are coming into play, changing unpredictably the matching condition. Hence, matching is considered load specific and demands adaptivity of the matching

system to correct for such changes.

The B_1^+ non-uniformity effects in ultra-high fields are mitigated by the use of transmit coil arrays with independent channel transmission and the employment of novel methods for pulse sequence design. Vaughan et al. [10], Katscher et al. [11], Zhu [12] and Adriany et al. [13] proposed techniques which are capable of establishing spatially selective RF fields that counteract for the general problem of B_1^+ -field inhomogeneity. Nevertheless, coil array elements inherently couple to each other, leading to enhanced requirements in comparison to the single coil case as far as matching is concerned. Additionally, the wave phenomena established in the sample further hinder the matching condition, as coupling depends also on its spatial characteristics. In essence, the introduction of coil arrays give rise to additional pathways for power to be scattered or dissipated and a matching system with additional degrees of freedom is compelled.

The present work fills a technology gap for efficient array transmission by developing novel instrumentation and methodology for performing adaptive array matching.

1.2 Contribution of the thesis

The present thesis addresses coil array matching in the transmit path of MRI scanners. An adaptive matching system with a newly developed capacitor design, based on a pre-characterization scheme and an algorithm containing randomization, realizes matching on a set of different optimization criteria.

In the lack of the appropriate tools and in the need to develop equipment to enable research in the field, a novel design of high-power and low-loss variable capacitor is presented. Its variability is empowered by a piezoelectric motor and its accurate position is controlled by a high-resolution optical encoder. The module is capable of operat-

ing in the ultra-high field of 7 Tesla and is controlled remotely by a computer. The modularity of the design enables the synthesis of networks capable of performing matching of multiple coil elements concurrently.

Using the scattering parameters' formalism, novel array matching algorithms are developed. In this regard, the methods employ an one-time matching system characterization stored in lookup tables. Following, multiple channel matching algorithms for different optimization criteria are explored based on the prior knowledge stored in the lookup tables. The matching procedure is not applied solely to perform the conventional zero-reflection per-channel matching. Instead, an holistic approach, called array matching, is engaged, taking into account close coupling of the array elements and total system losses, in order to maximize the power delivered to the sample.

A computational evaluation of the proposed matching criteria is conducted for examining the matching algorithm's performance. Different stages of the algorithm are assessed in terms of efficiency and insights concerning the underlying mechanisms of coupling and loss in the array setup are drawn.

Finally, the investigations are validated *in-vitro* and *in-vivo* by MR-based quantitative methods in conjunction with bench measurements and numerical evaluation to quantify the effects of the developed methodology.

1.3 Outline

The thesis is structured revolving about its bulk part in chapters written mainly in journal mode. The necessary intermediate work that has been undertaken is presented in separate chapters obligated by the subject separation.

Chapter 2 provides a presentation of the mathematical and methodological tools, hence forming the basis for what is discussed throughout the present work. Relevant MR-based measurement strategies are reviewed along with required elements of microwave theory and underlying mathematics. Finally, the matching problem and the theoretical parts essential for the completeness of this work are introduced.

Chapter 3 introduces the first original contribution of this work; the development of the automatic variable capacitor for adaptive matching. This constitutes the basic module which is omnipresent in the chapters to follow. Its requirements, design principles and verification measurements are presented here, along with a presentation of the peripheral hardware. Regarding the matching methodology, a single channel algorithm is introduced and the associated MR-based experiments are conducted.

Chapter 4 shifts towards the multiple channel paradigm. The material scaling process and method development are presented here. The developed matching system consists of two layers of single channel modules, surrounding a radiofrequency device which blends or isolates the signals of its ports, called Butler matrix. The chapter concludes with the algorithm's and objective functions' description.

Chapter 5 evaluates the operation of the objective functions in a visually admissible sub-space. The effect of the underlying coupling mechanism emerges to the depictions that span over a set of positions and suggest ways of algorithmic optimizations. Consequently, statistics concerning the algorithmic behavior and performance are presented, advocating for the selected mode of operation.

In Chapter 6 the multiple channel experimental results are presented. A set of matching conditions are compared against the case of lack of adaptivity, along with their pairwise comparisons. The quantification is based on a B_1^+ mapping technique, accompanied by a standard imaging method. The study is performed both in per-channel

level and as a whole. Theoretical and methodological aspects are put into practice, yielding the results of the multiple channel adaptive matching.

The thesis concludes in Chapter 7 with a discussion, along with the outlook of what may be further pursued in the realm of matching of MRI transmitters.

Chapter 2

Fundamental concepts

MR, being a multidisciplinary scientific field, combines theory from physics, engineering, mathematics and computer science. At the foundations of the MR experiment lie three fields, namely the static magnetic field B_0 establishing the polarization of the nuclei, the gradient electromagnetic field providing the spatial encoding and the RF electromagnetic field B_1^+ responsible for the excitation of the nuclei. The latter emanates from a single coil or a coil array and, regardless the case, mediates near-field coupling to the spins, with its magnitude being a figure of merit for the transmit path efficiency. With efficiency being a key consideration, matching is a requirement. For a single coil, matching in low-field proves to be a benign task. It complicates substantially when coil arrays or higher static field strength are used due to their inherent coupling at any field strength or the development of wave phenomena in higher static field, respectively. These hurdles make matching a key technology aspect for both single coil and coil array efficiency. In the present chapter, the aforementioned issues are considered in more detail, along with MR methodological aspects and microwave theory used throughout the present work.

2.1 Radiofrequency fields in MRI

MR imaging is sensitive to a set of parameters, which are responsible for the diversity of MR imaging techniques capable of producing images with different information content.

In order to create contrast in the final image, one needs to have access to the controllable parameters that give information about the intrinsic spin properties, such as different types of relaxation or proton density of the imaging subject. Among these parameters is the flip angle of the magnetization, called nutation angle, which creates the M_{xy} component of magnetization. The flip angle is proportional to the pulse duration and the amplitude of the B_1^+ field exciting the nuclei and is expressed by the formula

$$\alpha = \int_0^{t_p} \omega_{\text{nut}}(t) dt = \int_0^{t_p} \gamma B_1^+(t) dt, \quad (2.1)$$

where $\omega_{\text{nut}}(t)$ is the nutation frequency, t_p is the pulse duration, γ is the gyromagnetic ratio and $B_1^+(t)$ is the envelope of the transmit B-field for a pulse $\pi(t)$ [14, 15].

With the creation of meaningful contrast on the image being the objective, the uniformity of the tipping of the magnetization across the imaging region is a prerequisite. Equation 2.1 shows that this requirement is directly controlled by B_1^+ . Hence, information about the B_1^+ and potential means to control it promptly affect the image quality.

The magnetic fields for excitation and detection are represented by the complex vectors B_1^+ and B_1^- , respectively. The instantaneous component of B-field in the laboratory frame a coil produces per unit driving voltage $\hat{V}(t)$ is resolved in the Cartesian coordinates x , y and z as $\hat{B}(\vec{r}, t) = [\hat{B}_x \ \hat{B}_y \ \hat{B}_z]^T$. The B-field that oscillates at Larmor frequency ω_0 modulated by a pulse $\pi(t)$ is given by $\vec{B}_1(\vec{r}, t) = \pi(t)\hat{B}(\vec{r}, t)e^{i\omega_0 t}$. The complex vector B_1^+ responsible for

the transmission is expressed in the rotating frame as

$$B_1^+ = \frac{1}{2} (B_{1,x} + jB_{1,y}), \quad (2.2)$$

whereas the detectable signal, based on the reciprocity principle [16], is proportional to the negative rotating B-field, B_1^- , expressed by the formula

$$B_1^- = \frac{1}{2} (B_{1,x} - jB_{1,y})^*, \quad (2.3)$$

where $*$ is the complex conjugate operator. The amplitudes of the field rotating components that interact with the rotating bulk magnetization depend on coil geometry, tuning and matching.

Specific absorption rate

Similarly to the preceding, a coil driven with the reference voltage is primarily designed to generate the B-field associated with the excitation scheme described previously. Nevertheless, according to the Maxwell equations, the accompanied instantaneous E-field, $\vec{E}(\vec{r}, t) = \pi(t)\hat{E}(\vec{r}, t)e^{i\omega_0 t}$, is developed as a result of the B-field's temporal variation and is the cause for the power deposited on the sample as heat. This heating effect is the predominant risk in RF transmission for harmful physiological effects on living tissue. Hence, monitoring the output power and computing the yielded deposited power, either by numerically solving the Maxwell equations or by simpler models, is performed by all clinical MR scanners, which are configured to prevent a temperature rise in a volume of tissue of more than 1°C [17]. The relevant quantity to constrain is the specific absorption rate (SAR) and is calculated for the volume of the sample by the ratio of the instantaneous absorbed power P_{abs} over

its mass:

$$\begin{aligned} \text{SAR}(t) &= \frac{P_{\text{abs}}}{m} = \int_{\text{sample}} \frac{\vec{J}(\vec{r}, t) \cdot \vec{E}^*(\vec{r}, t)}{2\rho(\vec{r})} d\vec{r} = \\ &= \frac{1}{V} \int_{\text{sample}} \frac{\sigma(\vec{r}) |\vec{E}(\vec{r}, t)|^2}{2\rho(\vec{r})} d\vec{r}, \end{aligned} \quad (2.4)$$

where \vec{J} the current density, \vec{E} the electric field produced by the modulating pulse $\pi(t)$, σ the electric conductivity, ρ the sample density and V the sample volume.

Since both electric and magnetic fields are proportional to the driving input and $E = \omega B$ holds for coils producing B-field at low-frequency, then

$$\text{SAR} \propto \omega^2 B_1^2, \quad (2.5)$$

where B_1 is the amplitude of the transmit pulse and ω is the working frequency. Equation 2.5 reveals that SAR increases quadratically to the B_1 transmit field and suggests its ample control.

2.2 MRI methods

As previously presented, B_1^+ field has a spatial distribution depicted in a B_1^+ map, whose multiplication with the driving voltage results in the transmit B-field and the associated flip angles in the sample. The quantitative nature of B_1^+ motivates, in the present work, the use of B_1^+ -field maps as a measure of matching performance, since it suggests that the net coil efficiency can be readily validated with MR imaging methodology.

B_1^+ mapping methodology

The key challenge of B_1^+ -mapping to disambiguate large dynamic ranges of flip angle and spin density require lengthy experiments

which are SAR-intensive. Hence, B_1^+ -mapping methods prove demanding when dealing with these contradictory requirements.

The method applied in the present work for generating the B_1^+ maps uses an interferometric approach for overcoming the problem of large dynamic range of the transmit B_1^+ -field in a static field of 7 Tesla [18]. In this approach, magnetization is tipped to the large flip angle regime using a SAR-efficient, non-selective block pre-pulse for all elements of the array, that corresponds to the equivalent of a quadrature configuration. This method differs from the common element-by-element approach in that it sets the spins in a sensitive for the array baseline B_1^+ -field. By selectively inverting one coil's driving waveform at a time, a system of equations is filled. The system is over-determined by including both single channel and all-but-one channel inversions of the selected waveforms. Subsequently, the system can be solved for the B_1^+ -field contribution of each of the coil elements by a least square fitting. In a final step, failures of the fitting algorithm to a handful of pixels are corrected with a 2D median filter, under the assumption of the smoothness of the B_1^+ -field.

The accuracy of the method is enhanced by the signal model that additionally accounts for static field offsets and T_1 relaxation. To construct the aforementioned system of equations, a B_0 map is acquired prior to the pulse sequences and a set of pre-calculated lookup tables, based on parameter ranges that are suited for the experiment, are fed to a model, in order to correct for any deviations from ideal assumptions.

Towards creating B_0 maps, channel combination is performed in the following fashion. Two standard gradient echo sequences without saturation, with different echo times are acquired for each channel combination, giving rise to a system of equations and are followed by a singular value decomposition to extract the phase difference by the optimum channel combination. From these phase differences,

the B_0 maps are calculated. This method ensures that all parts of the image are excited at least once, hence prohibiting nulls in the B_0 maps that would render subsequent model calculations difficult. Details of the image acquisition method follow in the next section.

When employing RF shimming, the coil array can be driven with an arbitrary configuration from the independent amplifiers, such that the B_1^+ of the individual channels superimpose constructively. Therefore, the total B_1^+ of the coil array is calculated by adding the B_1^+ magnitudes of the individual elements and depicts the coil array capability on per-pixel basis.

SNR maps

As an alternative metric of matching performance, SNR maps are generated by a similar method to the aforementioned B_0 calculation. To this end, for all pairwise driving configurations, an image is acquired using the aforementioned standard gradient echo method with nominal flip angle of 15° . After reconstruction, the images are noise-normalized by dividing with the standard deviation of the noise acquired from a region that lies outside the imaging object, hence the resulted data are in arbitrary SNR units. The data from all combinations fill in a 4×4 matrix with complex entries, called transceive (TR) matrix, on per-pixel basis. To find the optimum linear combination of the coils that maximize SNR, an SVD is performed for the system, whose largest singular value is a measure of the maximum SNR achievable when the coil array is driven with the optimum transmit and receive channel combination. Hence, the left singular vector gives the optimum transmit channel combination for performing RF shimming on per-pixel basis, whereas the right singular vector suggests the optimum weighting coefficients for data combination upon reception. Both singular vectors are inherent characteristics of the coil array.

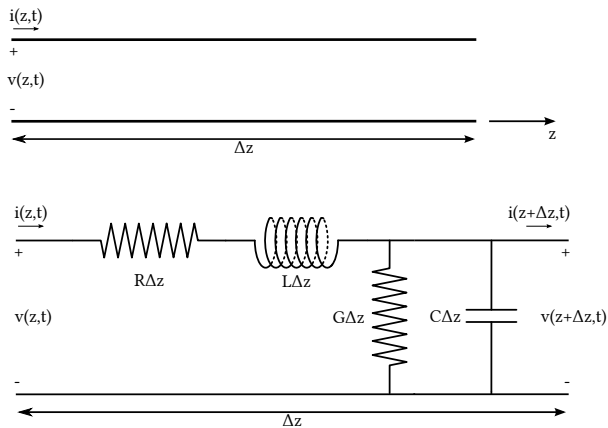


Figure 2.1: Lumped-element model of a piece of a transmission line.

2.3 Microwave theory

The Maxwell equations provide a complete picture of the electric and magnetic fields in space and the interactions of matter through electromagnetic waves. Nevertheless, they remain very complex and computationally costly descriptions of these interactions. Usually, one is interested only in simpler electric quantities describing a circuit, such as the current or voltage at a specific point of a device or the power the device reflects, consumes or transmits. When these quantities can be easily calculated for simple structures and the rules that govern the interconnection of these structures are also known, then the calculation of the network under investigation is becoming a less daunting task. This need for simplification gave birth to microwave theory, which provides simple formulas for the analysis and design of high frequency networks very much alike to circuit theory [19, 20, 21].

Microwave theory is based on the propagation of waves in mediums that are characterized by size comparable to their wavelength. Thus,

in the simplest model of such a distributed system, the transmission line voltage and current are not only time-varying functions, but dependent also on the position. The distributed system can be described by applying Kirchhoff's laws on a piece of the transmission line of sufficiently short length Δz , as shown in 2.1, from which the telegrapher's equations are derived for $\Delta z \rightarrow 0$ and assuming the sinusoidal steady state:

$$\frac{dV(z)}{dz} = -(R + j\omega L)I(z), \quad (2.6)$$

$$\frac{dI(z)}{dz} = -(G + j\omega C)V(z). \quad (2.7)$$

By substitution, Equations 2.6 and 2.7 become the reduced wave equations or Helmholtz equations

$$\frac{d^2V(z)}{dz^2} - \gamma^2V(z) = 0, \quad (2.8)$$

$$\frac{d^2I(z)}{dz^2} - \gamma^2I(z) = 0, \quad (2.9)$$

with γ being the complex propagation constant encapsulating the attenuation and the phase constant of an electromagnetic wave. The general solution of the wave traveling in the transmission line is given by

$$V(z) = V_0^+ e^{-\gamma z} + V_0^- e^{\gamma z}, \quad (2.10)$$

$$I(z) = I_0^+ e^{-\gamma z} + I_0^- e^{\gamma z}, \quad (2.11)$$

with $e^{-\gamma z}$ being the wave propagating in forward direction $+z$ and $e^{+\gamma z}$ being the wave propagating in reverse direction $-z$. Equations 2.10 and 2.11 constitute the basis of all derived quantities, such as impedance and reflection coefficient.

Despite the simplicity of the aforementioned formulas, voltage and current cannot be directly measured at high frequencies due to their distributed nature that changes across the geometry of the device

and the inherent difficulty to properly terminate the networks with short and open circuit conditions. Instead, a traveling wave for a propagation direction is measured at a reference port by means of its incident and reflected power. Given the characteristic impedance, a full description of a network's behavior is provided by the frequency dependent scattering parameters which relate the incident and reflected voltages when ports are terminated at matched loads. The scattering parameters of an n -port network compose a square matrix, called S-matrix, and are directly measured with a network analyzer [20, 21, 22].

The network analyzer is the most useful instrument in measuring the properties of electrical networks at high frequencies. Its basic principle is to measure the amplitude and phase of the waves transmitted through a device under test (DUT) and reflected from it simultaneously from multiple ports. The measurements are compared against a reference signal transmitted from an internal RF source and split with directional couplers for measuring the reflected waves. Finally, all signals are fed into coherent receivers and, after been mathematically processed, the S-parameters are obtained. The S-parameters of an n -port network are defined in relation to the aforementioned solution of the voltage wave in Equation 2.10 and are given from the ratios of incident and reflected waves on the network ports according to the formula

$$\begin{bmatrix} v_1^- \\ v_2^- \\ \vdots \\ v_n^- \end{bmatrix} = \begin{bmatrix} s_{11} & s_{12} & \cdots & s_{1n} \\ s_{21} & s_{22} & \cdots & s_{2n} \\ \vdots & \vdots & \ddots & \vdots \\ s_{n1} & s_{n2} & \cdots & s_{nn} \end{bmatrix} \begin{bmatrix} v_1^+ \\ v_2^+ \\ \vdots \\ v_n^+ \end{bmatrix}, \quad (2.12)$$

where

$$s_{ij} = \left. \frac{v_i^-}{v_j^+} \right|_{v_k^+ = 0 \text{ for } k \neq j} \quad (2.13)$$

implies that all ports other than i and j must be terminated with

matched loads. That imposes the requirement of defining reference planes at each network port.

To simplify Equations 2.12 and 2.13 from signs at superscripts, the following convention for incident and reflected waves at the ports will be used correspondingly:

$$a = \begin{bmatrix} a_1 \\ a_2 \\ \vdots \\ a_n \end{bmatrix} = v^+ = \begin{bmatrix} v_1^+ \\ v_2^+ \\ \vdots \\ v_n^+ \end{bmatrix}, \quad (2.14)$$

and

$$b = \begin{bmatrix} b_1 \\ b_2 \\ \vdots \\ b_n \end{bmatrix} = v^- = \begin{bmatrix} v_1^- \\ v_2^- \\ \vdots \\ v_n^- \end{bmatrix}, \quad (2.15)$$

and therefore

$$b = Sa, \quad (2.16)$$

where the non-indexed letters correspond to matrices when uppercase and to vectors when lowercase.

Summing up, the s_{ij} entry of the S-matrix corresponds to the voltage transmission coefficient from port j to port i when all other ports are terminated with matched loads, whereas it must be noted that the S-parameters are normalized to the system's characteristic impedance. In the following, the characteristic impedance is set to unity, but any other value would be applicable with the relevant scaling. Moreover, under the assumption of equal characteristic impedance to all ports, the S-matrix can be expressed in terms of the impedance matrix and vice versa as follows

$$[S] = \frac{([Z] + [I])^{-1}}{[Z] - [I]} \quad (2.17)$$

$$[Z] = \frac{[I] + [S]}{([I] - [S])^{-1}}, \quad (2.18)$$

where I is the unitary matrix.

From theory, it follows that the forward power crossing the cross-section of port i for the normalized impedance is

$$p_i^+ = \frac{1}{2} |a_i|^2 \quad (2.19)$$

and consequently the reflected power is

$$p_i^- = \frac{1}{2} |b_i|^2. \quad (2.20)$$

Hence, the total power flowing through port i is

$$p_i = \frac{1}{2} (|a_i|^2 - |b_i|^2). \quad (2.21)$$

For a passive n -port network with real reference impedance, the incident power is non-negative:

$$\sum_{i=1}^n p_i \geq 0 \quad (2.22)$$

and since

$$\begin{aligned} \sum_{i=1}^n (|a_i|^2 - |b_i|^2) &= a^H a - b^H b = \\ &= a^H a - a^H S^H S a = \\ &= a^H (I - S^H S) a, \end{aligned} \quad (2.23)$$

where H denotes the Hermitian transpose (complex conjugate of the transpose), then

$$\Re \{ a^H (I - S^H S) a \} \geq 0, \quad (2.24)$$

which indicates that the matrix $I - S^H S$ is positive semi-definite and measures the power loss in the network. If $I - S^H S = 0$, then the network is lossless. In the following, the trace of the matrix, $tr(I - S^H S)$, is the cumulative metric for accounting for network losses.

2.4 Matching and decoupling

Radiofrequency systems consist of interconnected devices with different characteristics and functionality. A traveling wave incident to a junction encounters a discontinuity created either by geometry or medium change, forcing it to be reflected and power to be lost. The degree of reflection is captured by the corresponding scattering coefficient. By introducing new discontinuities in a calculated manner, reflections may be canceled. The engineering process which appropriately transforms the impedance of a network into another value is called matching and the corresponding circuits are called matching networks.

Examples of matching can be found as early as the first implementations of the telegraph and electrical distribution systems, with their objective being maximum power transfer from the source to the load. The universality of the task to maximize power transfer is a practical problem situated at the epicenter of the design of the MRI transmit system as well. Considering the single channel case of transmit, two different matching criteria are prominent; *conjugate* and *reflectionless* matching.

Conjugate matching stems from the maximum transfer theorem, when a source of a *given impedance* Z_{src} is required to deliver most of the generated power to the load Z_L , as depicted in Figure 2.2. Calculating the power delivered to the load by $P = \frac{1}{2} \Re \{ V_{\text{in}} I_{\text{in}}^* \}$ and the input impedance Z_{in} , the maximum power delivered to the load is found by differentiating P for both real and imaginary part of Z_{in} . The system of equations yields

$$Z_{\text{in}} = Z_{\text{src}}^*. \quad (2.25)$$

When the conjugate matching condition is assumed for a lossless piece of line with phase constant β and of length d terminated by a

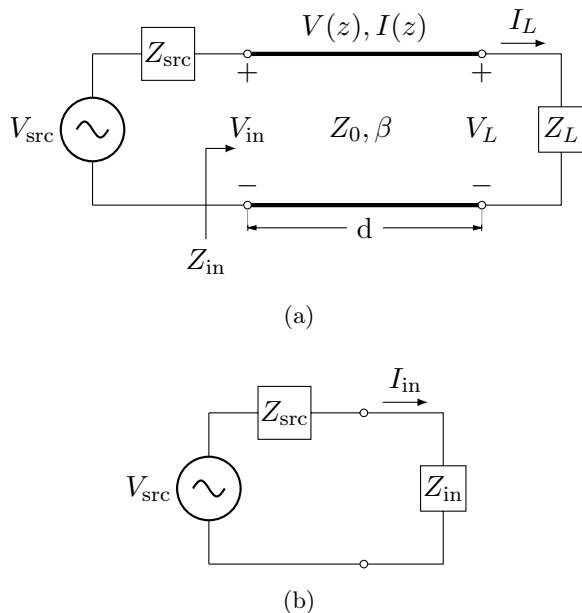


Figure 2.2: Conjugate matching delivers maximum power from the source to the matched load when $Z_{\text{in}} = Z_{\text{src}}^*$ holds. In (a), the source is connected to the load Z_L via a lossless transmission line of characteristic impedance Z_0 and phase constant β . In (b), the Thevenin equivalent circuit for the input impedance of the line and load as seen from the source is depicted.

load Z_L , then

$$\Gamma_L = \Gamma_{\text{src}}^* e^{2j\beta d} \quad (2.26)$$

holds, where the term $e^{2j\beta d}$ is owed to the phase shift of the reference plane [23]. Moving the matching network to the other side of the transmission line and looking into the line it holds

$$\Gamma_{\text{in}} = \Gamma_L e^{-2j\beta d} = \Gamma_{\text{src}}^*, \quad (2.27)$$

which, in turn, yields

$$Z_{\text{in}} = Z_{\text{src}}^*. \quad (2.28)$$

Thus, a matching network can be inserted at any point of a lossless line to achieve conjugate matching of a terminated line with a

load Z_L . This type of matching is employed when one cannot isolate the equivalent network comprising the source. For example, the sequential stages of a microwave amplifier, where a later stage is the load to the preceding stage, are routinely conjugate matched. This matching condition does not suppress reflections between the matching network and the load, hence a standing wave may be present, with reflections adding constructively at the load input for maximum power transfer.

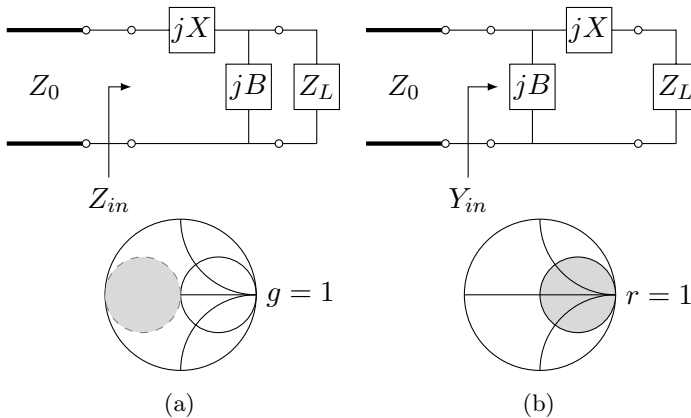


Figure 2.3: The two possible L-network topologies of reactive element circuits for single channel matching, along with the corresponding exclusion circles. When the load impedance is within the gray circles, the matching network cannot match the load impedance to Z_0 . The load impedance is $Z_L = R_L + jX_L$.

The matching condition that nullifies wave reflection at a reference plane, depicted in Figure 2.3, is different to conjugate matching and is called reflectionless matching. The matching network is preceded by a transmission line of characteristic impedance Z_0 and succeeded by a load of impedance Z_L . Here, the source is assumed to be matched, hence, in order to maximize power transfer to the load, its input impedance must be transformed to equal the characteristic

impedance of the line according to the formula

$$Z_{\text{in}} = Z_0. \quad (2.29)$$

Let us look at the first case depicted in Figure 2.3. A matching network in this case can always be realized, given that the complex input impedance Z_{in} has non-zero real part. For this example, the solution is based on lumped elements, such as capacitors and inductors, whereas resistors are not an option due to their lossy nature. The calculation of Z_{in} from the in-series reactance X and in-parallel susceptance B leads to the following matching condition:

$$Z_{\text{in}} = jX + \frac{1}{jB + \frac{1}{R_L + jX_L}} = Z_0. \quad (2.30)$$

Solving for the real and imaginary part of the equation one gets $X = \pm Z_0 \sqrt{\frac{1}{G_L} (\frac{1}{Z_0} - G_L)}$ and $B = -B_L \pm \sqrt{G_L (\frac{1}{Z_0} - G_L)}$, where G denotes conductance. A solution exists when $G_L \leq 1/Z_0$ or, in normalized form, $g_L \leq 1$. It follows that, in the general case, one needs at least two independent variables to match an arbitrary load Z_L to a Z_0 line. This readily implies that two reactive elements are necessary at their simplest arrangement as the given L-section network, with one reactance in series and one susceptance in parallel. Similar calculations can be carried out for the complementary case of Figure 2.3.

One should be aware that other matching strategies exist too. In the receive path for example, the matching network introduced between the coil and a low-noise amplifier aiming for the minimum noise factor is called noise matching. In this case, which is out of the present focus, matching results in suppressing the noise propagating to the receive amplifier rather than maximizing the power transfer.

Traditionally, all aforementioned formulas are expressed in terms of impedance parameters, but one can rewrite all formulas in terms

of S-parameters, which are easier measured by means of a network analyzer.

In transmit MRI, the amplifiers are isolated, making reflectionless matching the main criterion for load power maximization. The characteristic impedance of the transmission line Z_0 is selected such that it compromises between the goal of minimum losses and its maximum power handling. On the contrary, the load impedance Z_L is an arbitrary impedance, which can be time-variant or spatially dependent on the electromagnetic environment. This calls for a matching network whose main goal, in the present work, is its adaptivity in order to cope with load alterations. In practice, given an arbitrary load impedance, the adjustable matching network should be capable of performing the necessary impedance transformation that results in minimum reflections at the input of the matching network in order to achieve maximum power transfer to the load.

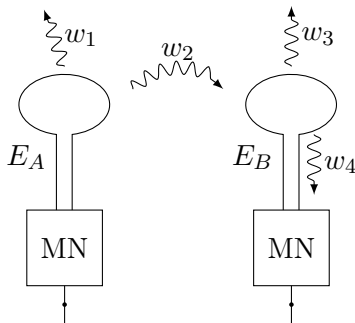


Figure 2.4: Coupling mechanisms when array element E_A transmits and E_B remains passive.

In the advent of multiple channel transmission in MRI, the task of matching the coil array is getting harder due to the intrinsic characteristic of *mutual coupling* among the elements. Mutual coupling refers to the multiple mechanisms related to the energy exchange between coils found in close proximity.

Referring to Figure 2.4, one can identify the various ways of a signal propagating unwittingly in multiple paths. Let a pair of two coil elements in free space. When element E_A transmits a wave w_1 , part of the energy will couple to the element E_B through wave w_2 . Since the element E_B has inherently a mismatch, part of the energy will be back-scattered in free space through wave w_3 and the rest will be propagated back in E_B towards its input as w_4 . The effect of w_4 is expressed in the off-diagonal elements of the scattering matrix and, since coupling changes more profoundly in high field MR, as discussed previously, the input impedance of the array alters notably. Therefore, one cannot discuss distinctively about matching or decoupling, because both belong to the same conceptual category of eliminating elements of the composite network S-matrix. In S-matrix notation, nulling the diagonal elements is the mathematical condition of reflectionless matching and nulling the off-diagonal elements corresponds to decoupling the elements of the array.

Due to the aforementioned difficulties and the importance of array matching quality, a lot of research has been conducted since early days of antenna arrays, in the mid-20th century. In this respect, MRI faces similar challenges to antenna theory and applications and, therefore, many methods are largely borrowed and extended.

Several researchers have proposed nulling the off-diagonal elements of the impedance or scattering matrix representations in order to decouple array's elements. By doing so, matching reduces to the relatively simple per-port matching case. Mishustin [24] synthesized reactive networks for decoupling a fixed load by a scattering matrix composition method. Others, like Widrow and Mantey [25], Gupta and Ksienski [26] and Steyskal and Herd [27] filtered unwanted signals in a post-processing step by using algorithms or fixed circuits, while Pasala and Friel [28] simulated several geometries with the method of moments, making ideal assumptions about the coupling of the non-nearest neighborhood elements. Lastly, Kang and Pozar

[29] described a method of mode decoupling by introducing higher modes to correct for those cases that cannot be captured by filtering with standard Chebyshev multi-section transformers. All these methods concern either fixed loads or far-field or geometries that are not suited for the intended general approach, where matching and decoupling are considered concurrently.

In MRI, coil arrays were initially adopted for the receive side. Even though receive and transmit share a lot of theory, they differ largely in the matching criteria and matching hardware, as partly discussed previously. Hence, Roemer et al. [30] performed decoupling by overlapping neighboring elements to eliminate next-neighbor coupling, whereas a mismatching scheme with low input impedance amplifiers was chosen to decouple non-overlapping elements. Andersen and Rasmussen [31] disregarded matching and investigated pair-wise networks of reactive elements for a two coil setup. Lee et al. [32] and, more recently, Mahmood et al. [33] used similar methods, assuming that the coil is matched and suggested a pair-wise network of reactive elements for a multiple port setup. The former implementation ignores coupling of non-neighboring elements, while the latter is extremely demanding at the number of required matching elements when coil elements are in plenty. In principle, one needs two degrees of freedom for controlling every entry of the scattering-matrix. Assuming that the matching network consists of reactive elements only, the number of variables one has to deal with is $(N + N^2)/2$ and corresponds to the upper (or lower, due to reciprocity) triangle of the S-matrix. For example, for a 2-port coil array one needs 6 reactive elements, for a 4-port 20 and for an 8-port 72. This readily shows that the task of matching and decoupling becomes daunting as the array becomes larger. Moreover, none of the aforementioned implementations aim for an adaptive solution.

Adaptivity was only recently introduced for either matching or decoupling. The simplest and most common approach, suggested by

Doty et al. [34] and de Zwart et al. [35], assumes fixed loading conditions and performs the matching by manual trimmers at all individual ports by simulating the required values. When the load changes, one has to repeat the calculation or manually find the new matching condition of the coil array. Sun and Fidler [36] and Sohn et al. [37] used a bank of capacitors switched on and off by PIN diodes, while Muftuler et al. [38], Neo et al. [39] and Pavan [40] proposed automatic matching by using varactors in the bore. Their methods work well for the Rx path, but the biasing of the varactors limits the power for the Tx path, rendering it also an unsafe choice. Moreover, this solution is sensitive to gradient induced currents that can unpredictably alter the matching. To mitigate the aforementioned problems Hwang and Hoult [41] and Keith et al. [42] proposed mechanical variable capacitors to perform per-channel matching.

Chapter 3

Single channel automatic matching

Manuscript in preparation:

Katsikatsos G., Pruessmann K. P.. *High-power variable capacitor module with optical closed-loop control for automatic matching.*

Any MR modality involves an RF transmission path emitting the B_1^+ field necessary for the nutation of the nuclear spin population. The efficiency of the transmission path depends on coil matching, which is affected by the close coupling with the sample, thus making efficiency susceptible to changes of loading conditions. The purpose of the present chapter is to conceive and implement the instrumentation enabling automatic impedance transformations by means of an automated adaptive matching network. To this end, a high-power, low-loss, wide-range, variable capacitor is developed. It is actuated by piezoelectric motors with closed-loop control by optical encoders. The capacitor forms the building block of a single channel matching network aiming at coil impedance matching. A network analyzer measures the input impedance of the combined system and a computer calculates the minimum reflection condition based on prior

knowledge of the capacitors. The prior knowledge stems from a pre-characterization step during the manufacturing process and comes in the form of capacitor-specific lookup tables. Finally, the computer adjusts the capacitors for the matching condition.

3.1 Introduction

Image generation in MRI relies on how one orchestrates the properties of the static B_0 field in conjunction with the gradient, the RF excitation and the reception fields. Spin nutation achieved by the emitted B_1^+ field depends on the efficiency of the transmission path, which in turn heavily depends on the loading conditions of the coil [43, 44, 45]. Different positioning and structure of biological samples have unpredictable impact on the coil input impedance due to the loading variations, hence altering its matching. Mismatching shifts the frequency of the resonant circuit and is, therefore, sometimes called de-tuning. From now on, we refer to the coil readjustments for mismatching or de-tuning as impedance matching or simply as matching. In order to eliminate the losses from the reflected power owing to the mismatch and, thus, maximize the transmitted power, one needs to transform the coil input impedance as seen by the amplifier by means of a microwave system called matching network.

Impedance variations are particularly detrimental at high Larmor frequencies due to the shortened wavelength. The outcome is two-fold; on one hand, there is a need for matching adaptivity to counteract for the mismatching caused by the pronounced loading variations owed to the increased electric field [46] and, on the other hand, matching complicates even more when coil arrays are of concern [47]. Regarding the correction of the B_1^+ non-uniformity generated by the strong coupling and wave phenomena in the sample at high field, arrays provide more degrees of freedom when it comes to spatial encoding schemes [48, 49, 50]. On the downside, they pose significant

challenges as far as the matching is concerned, as the coupling of the array elements provides additional scattering pathways, hence adding complexity [32].

There are several approaches dealing with the matching problem, with the most widespread being manual matching using trimmers on predetermined loads [34, 35]. Yet, these methods are patient-specific and time-costly and automatic matching instrumentation in the bore has been, therefore, suggested using different approaches, one of them being the use of varactor diodes which control the capacitance by DC biasing [39]. Nevertheless, their limited power handling and biasing sensitivity owed to gradient induced currents or high output power of the RF amplifier constrains the applicability of these methods only to receive purposes and calls for alternatives. Thus, for the transmit path, mechanical variable capacitors were introduced [41, 42]. In the latter work, the core of the design is a coaxial air capacitor whose variability is achieved by a moving rod. The choice of air as dielectric limits the capacitance range and holds lower voltages compared to other materials. Moreover, the low volume efficiency would render a reasonable range for our purposes prohibitively large.

In order to address the aforementioned shortcomings, a variable capacitor of planar design was developed. A ceramic with high dielectric constant and high voltage rating results in a large capacitance range and small footprint layout. The moving electrode is floating with no galvanic connection, making the design more reliable and lightweight. The capacitor is actuated by a piezoelectric motor and positioned by receiving feedback from an optical sensor. The variable capacitor is pre-characterized electrically in S-parameter nomenclature for its span and constitutes the building block of a matching network controlled by a computer. A set of algorithms are developed along with it for performing automatic matching on transmit coils under different loading conditions.

3.2 Material

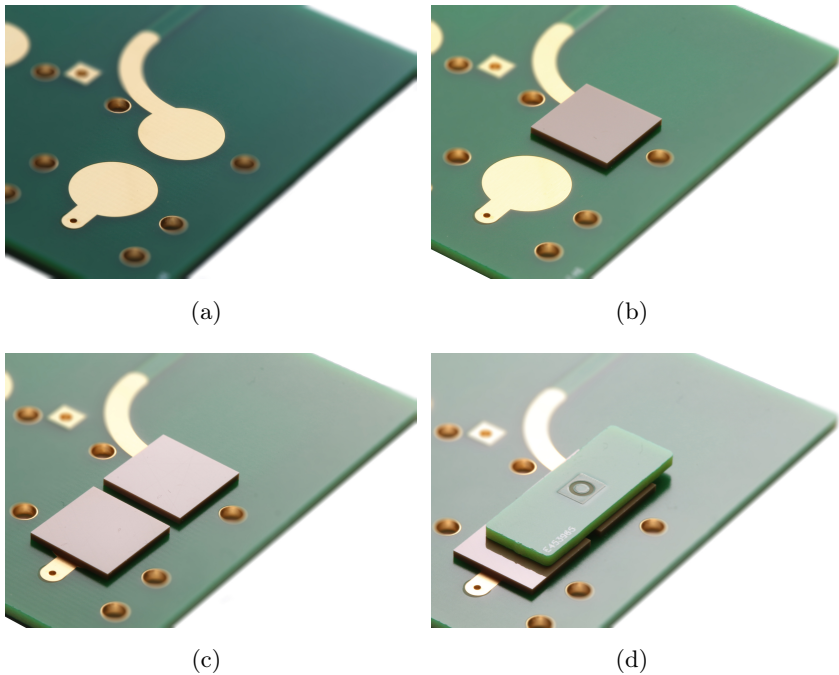


Figure 3.1: A single capacitor. (a) The bottom PCB with the round electrodes ‘A’ and ‘B’ exposed. (b-c) Placement of the $12 \times 12 \times 1$ mm dielectric slabs. The two slabs form a virtual rectangular measuring $12 \times 27 \times 1$ mm. (d) The floating electrode ‘C’ etched on a separate PCB. The latter is mechanically fixed on a II-shaped structure that moves it linearly (shown in Figure 3.2).

Figure 3.1 shows the assembly stages of a single capacitor. It consists of three parallel electrodes conceptually forming two capacitors connected in series. The electrodes ‘A’ and ‘B’ are etched on a double-sided FR4 PCB with dielectric constant of $\epsilon_{\text{PCB}}=4.36$. Electrode ‘C’ is etched on a single-sided PCB and is suspended 1 mm above the other two electrodes with the dielectric slabs in-between.

Figure 3.2 shows the module that hosts two matching networks consisting of four capacitors in their casing, as used in the magnet. The planar design increases the mechanical robustness and the ease of PCB manufacturing facilitates the system production.

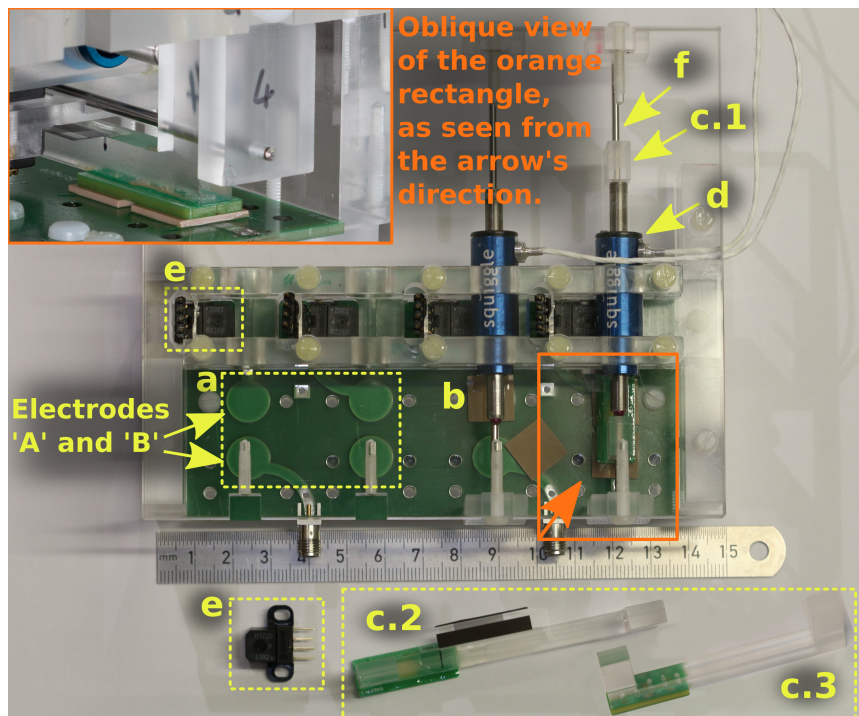


Figure 3.2: Top and oblique (top-left corner) view of the capacitor module in different assembly stages. (a) Top view of electrodes ‘A’ and ‘B’ of a matching network, along with their 50 Ohm microstrip traces. (b) Slabs of the dielectric material. (c1, c2, c3) Different views of a II-shaped PMMA with the floating electrode ‘C’ attached to it, along with the encoding strip. In the oblique-view image the bearing of the moving part. (d) Piezoelectric motor. (e) Optical encoders. (f) Steel rod responsible for the bearing of the moving part.

Dielectric material

Typical loading variations of the coils within the scope of the present work call for a capacitance of up to 60 pF. For the purpose of boosting the capacitance, the space between the electrodes is filled with two synthetic ceramic slabs (Kyocera, Kyoto JP) with dielectric constant of $\epsilon=142$, losses of $\tan \delta=0.0002$ (at $f=1$ GHz) and breakdown voltage of 8.2 kV/mm, depicted in Figure 3.3.

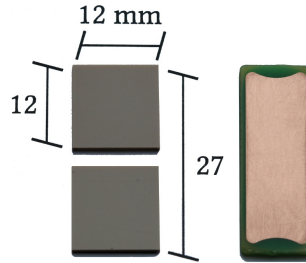


Figure 3.3: Slabs of the dielectric material in scale, along with the electrode of the floating PCB. The electrode has shape and dimensions such that prohibit extreme values of the electric field at the interfaces of the dielectric materials.

Electric field edge effects, where charge density tops, are suppressed by round-shaping the electrodes to prohibit charge concentration in a small area. This effect could lead to extreme E-field values prone to break the dielectric by corona discharge. The corresponding voltage value that the capacitor withstands until its electric field breaks by this mechanism is called breakdown voltage. Moreover, the severe difference of the dielectric constant at the material interfaces is another mechanism contributing to extreme values of electric field. These values can be amplified by air pockets between the dielectric and the copper plates, where the electric field builds up in the air due to its lower dielectric constant. According to the formula $E_{\text{air}}/E_{\text{diel}}=\epsilon_{\text{diel}}/\epsilon_{\text{air}}$, the capacitor is susceptible to similar corona

discharges. In the event that the capacitor copes with the breakdown voltage, loss of capacitance is owed to the air pockets due to the in-series arrangement of the two dielectrics. To mitigate both effects, the dielectric slabs are designed with very tight manufacturing specifications having a flatness of 1 μm and a surface roughness (R_α) of 0.1 μm . To further enhance the capacitor to withhold higher voltage, the copper-dielectric interfaces are sprayed with liquid Teflon, which forms a thin film of material with a dielectric constant of $\epsilon=2$, hence reducing the E-field relative to air by a factor equal to 2.

The dielectric slabs measure $12 \times 12 \times 1$ mm and are positioned 3 mm apart from each other in a fictitious rectangular area of 27×12 mm, as depicted in Figure 3.3.

Motors

The motors (Squiggle, New Scale Technologies, Victor US) consist of a cylinder made of a piezoelectric material which translates the internal wobbling motion in an one-dimensional translation. The cylinder surrounds a steel axis that rotates with the help of this wobble. A fixed thread attached to the motor casing converts the rotation of the axis into a translational motion. As the motion principle is based merely on the friction between the piezoelectric material and the steel axis, the motion of the axis has varying acceleration due to the high sensitivity to the varying mechanical loading. Therefore, extra design effort is made for minimizing potential friction surfaces. For this purpose, the moving PCB of the capacitor is secured on a Π -shaped acrylic bar (PMMA) which is suspended solely by two anchoring points and has only one degree of freedom. A static steel rod of 1 mm diameter holds the PMMA bar firm to the anchoring points, having a negligible effective friction interface. The PMMA bar is actuated by the piezoelectric motors, which are fixed on the casing of the module. The copper-dielectric interface causes most of

the friction experienced by the motors, which is significantly reduced by the aforementioned use of Teflon spray.

Motor's driving unit



Figure 3.4: The piezoelectric actuators and their driving unit.

The piezoelectric motors, along with their driving unit, are shown in Figure 3.4. The motors are controlled by their driving unit, which includes all the electronics necessary to drive the motors and is controlled by a computer through a USB cable. Each motor is connected with its accompanied driving unit through a 3-pole high-potential cable, which is part of the piezoelectric resonator. These cables needed to be extended, because, contrary to the capacitor, the driving unit is placed outside the magnet, as it contains ferrite parts. The extension was accomplished by cutting out a piece of the special connecting cables and soldering extensions of the same impedance such that the resulting impedance equals the impedance of the initial cable.

Position control

For the purposes of accurately controlling the position of the floating electrode and counteracting for the varying speed of the motor, an optical linear encoder (HEDS-9720, AVAGO, San Jose US) is installed in order to accurately monitor the position of the floating electrode. The encoder measures its relative position by counting the rising and falling edges of a TTL pulse train produced by the bars and windows of an encoding strip. Moreover, it is of quadrature type for sensing the direction, has a nominal resolution of 180 μm and is located on the side of the moving part where the encoding strip is attached. The strip consists of 90 μm equidistant bars and windows printed in-house with a photo-lithographic method. The resolution of the position is further enhanced by the ability of the I/O unit of the encoder (PhidgetEncoder 1047, Phidget, Calgary CA) to count both leading and trailing edges of both channels, which ultimately quadruples the interface resolution, reaching a resolution of 45 μm . Based on conservative measurements of maximum electrode speed, the update rate of 125 Hz is amply sufficient for accurate position control.

The encoder I/O unit is located inside the bore and communicates with the control PC via a USB cable.

Casing

Each capacitor is terminated on one side to an SMA connector through an RF trace of 50 Ohm microstrip line etched on the same PCB as the fixed bottom electrodes. The capacitors are on their other side connected in pairs, thus forming a matching network suited for matching a single coil. The RF traces are routed on the PCB in maximum distance from the moving part of the capacitor in order to avoid any electromagnetic interaction from fringing fields.

3.3 Methods

Quality factor

An important figure of merit of the capacitor is its quality factor (Q-factor), which measures its losses and is essential for calculating its breakdown voltage when it is used in resonators. Concerning the losses, the higher the Q the higher is the efficiency and the less are the losses. Concerning the voltage breakdown, Q-factor determines voltage by means of the power in the resonator. To study both aspects at the same time, the Q-factor was measured at a critical position, as described in the following. For an ideal RLC resonator, the Q-factor is defined as follows:

$$Q = \frac{\text{(average energy stored)}}{\text{(energy dissipated per cycle)}} = \omega \frac{W_e + W_m}{P_{\text{loss}}}, \quad (3.1)$$

where W_e and W_m are the energy stored in the electric and magnetic field, respectively. The stored energy is exchanged between the reactive elements in every cycle, i.e. $W_e = W_m$, which yields

$$Q = \omega_0 \frac{2W_e}{P_{\text{loss}}} = \omega_0 \frac{2W_m}{P_{\text{loss}}} = \frac{1}{\omega_0 RC} = \frac{\omega_0 L}{R}. \quad (3.2)$$

In order to measure the Q-factor of the capacitor, a resonator was built comprising of the capacitor and an in-series air-inductor. Based on theory, the resonance frequency of the circuit is given by Equation 3.3:

$$\omega_0 = \frac{1}{\sqrt{LC}}. \quad (3.3)$$

For calculating the voltage breakdown, the quality factor was measured for a critical position which corresponds to the minimum capacitance. For this position, the edges of the opposing electrodes are at minimum distance and an extremely high E-field is built across

them. The resonant circuit was build by the capacitor and an inductor with 0.8 mm thick copper wire and appropriate dimensions for tuning the resonator at 298 MHz.

In the case two components with different Q-factors are connected in-series, the total circuit Q-factor is

$$\frac{1}{Q_{\text{total}}} = \frac{1}{Q_1} + \frac{1}{Q_2} = \frac{1}{Q_C} + \frac{1}{Q_L}. \quad (3.4)$$

In order to determine the Q-factor of the custom-made capacitor, denoted by Q_C , the Q_{total} was measured by using an inductor of known value. In the absence of a calibration-graded inductor, the measurement of the inductor's Q-factor was performed by an indirect method using a readily available high-Q capacitor. Therefore, following the tuning of the resonator to the position prone to breaking with the custom-built inductor, the latter was disconnected from the circuit and a high-Q capacitor was connected to it. The measurement of the auxiliary resonator, Q_{total} , was conducted through two decoupled loop antennas connected to the network analyzer. The isolation of the loops was -80 dB. Approaching the loops in the vicinity of the resonator and measuring the coupling at the resonance peak, the Q-factor was calculated by the ratio of the center frequency over the bandwidth of the -3 dB span. It is important during this measurement not to approach the probe loop to the very vicinity of the resonator, as the increased coupling coefficient reduces the accuracy of the measurement by adding losses in an unpredictable way. Given the Q_{total} and the Q_C of the high-Q capacitor provided in the specification sheet, the Q_L of the inductor was deducted. Subsequently, the inductor was reconnected to the custom-made capacitor and the aforementioned experiment was repeated so as to calculate the Q_C by the known values. Knowing the Q-factor of the capacitor, it is possible to calculate the losses for a given capacitance value at the frequency of interest based on Equation 3.2.

Breakdown voltage of the capacitor

Apart from the loss estimation, the Q-factor can be used to calculate the voltage across the capacitor, given the topology and the input power. These properties are crucial characteristics in order to estimate the robustness of the transmission path.

For the capacitor to cope with the high power output of the RF amplifiers, which are in the kW regime, an estimation of the capacitor's breakdown voltage is necessary for the aforementioned most perilous position for breaking. The measurement of the breakdown power of the capacitor can be experimentally obtained through a destructive test. Initially, the resonant circuit was tuned to 298 MHz and its reflection coefficient $|\Gamma|$ was measured with a calibrated network analyzer. At this stage, the circuit was not matched at all, as any component connected to the resonator would alter its Q-factor. Subsequently, the circuit was connected through a dual directional coupler to an amplifier. The forward coupled port of the directional coupler was terminated to a 50 Ohm resistor and the reflected coupled port to a spectrum analyzer in order to detect any non-linearity indicating the onset of critical behavior of the capacitor. The amplifier was driven by a hard pulse of 100 us length at a modulation frequency of 1 kHz, giving a duty cycle of 10%. Based on the definition of Q-factor and the energy stored in the capacitor, the voltage when the breakdown of the capacitor occurs can be calculated:

$$V = \sqrt{\frac{2P_i(1 - |\Gamma|^2)Q}{\omega_0 C}}. \quad (3.5)$$

The capacitors of the matching network were additionally tested under typical MRI conditions. The test was done in-bore by attaching the matching network and one coil in cascade. Between the output of the amplifier and the input of the matching network, a directional coupler was connected to measure the forward power. The matching network capacitors were set to the positions susceptible to breaking.

Ultimately, the 4 kW scanner amplifier was ramped up to its full power.

Motion of the floating electrode of the capacitor and precision of positioning

The floating electrode of the capacitor approaches a desired position in full speed, which is approximately 2 mm/sec. While the capacitor is moving, the respective encoder is polling the position of the capacitor giving feedback to the positioning control. Mechanical hysteresis causes a systematic error within the resolution of ± 45 μm depending on the approaching direction of the capacitor to its target position.

The initialization of the capacitor position is done automatically every time the system starts up through the use of the encoding strip, which is extended by 1 mm from either side of the terminating points of the capacitor. The moving part of the capacitor is designed such that it can tolerate large out-of-limits operation. This feature is merely used during the calibration phase, i.e. the initialization starts by moving the capacitor towards one of its extremes. In case the capacitor exceeds the boundaries, it immediately comes to a halt. Following, the encoder counters are reset and therefore measure the absolute distance. Finally, the motors move in the opposite direction heading to the capacitor's initial position. When the calibration is completed, the module is in a well-defined state for operation. The calibration lasts approximately 3 seconds.

Capacitor range and lookup tables

The values of the capacitance at every position of the capacitor's electrode are calculated with the help of an in-series inductor of known value and Equation 3.3 and with the use of a calibrated network analyzer.

Having established a robust method to accurately position each capacitor, the 2-port S-matrices of the matching network are measured on the bench with a network analyzer for all position combinations. The encoding resolution, combined with the distance to be covered over the full range of the capacitors, yields a discretization of 300 points. Since the designed matching network consists of two capacitors, a lookup table is built containing the 300^2 possible positions. The lookup table is indexed by the two values of the position and contains the four values of the S-matrix. For each measurement, the values are averaged by 10 repetitions in order to avoid erroneous values caused by electrical noise. The averaging is performed only during the production process of the capacitor.

Matching strategy

Maximization of power delivery in the single-channel case is achieved by conjugate matching, which transforms its input impedance into the output impedance of the amplifier, thus minimizing the reflected power.

The setup comprises of a network analyzer, the matching network and a coil in cascade. The automatic matching is accomplished in four consecutive steps. Firstly, the reflection coefficient is measured with a network analyzer at the input of the matching network in order to analytically calculate the reflection coefficient of the coil. In this stage, the capacitors of the matching network are at an arbitrary position. Secondly, the S-parameters of the matching network that cancels out the reflection at its input are analytically calculated. Thirdly, the appropriate S-parameter is exhaustively searched in the lookup table. The result of this search is the associated pair of positions, which is passed to the motors so as to move accordingly. Finally, residual mismatch from the lookup table calculation and mechanical imperfections are iteratively corrected with the help of an

exhaustive neighbor search, with feedback obtained from the network analyzer in a closed-loop fashion. In this corrective step, the actual minimum of the magnitude of the reflection coefficient is found using heuristics: a gradient descent algorithm searches in the vicinity of the position pair for an improved matching condition and terminates the search when the reflection coefficient is lower than the threshold of -35 dB. When the optimal matching is achieved, the network analyzer is disconnected from the input of the matching network and the scanner is reconnected.

The S-parameters necessary for the first step of the aforementioned procedure are denoted by \tilde{S} , S^{MN} and S^c for the combined system, the matching network and the coil, respectively. Additionally, the forward waves are denoted by a and the reflected waves by b . Based on theory [21], the Equations 3.8 hold:

$$b^c = S^c a^c \quad (3.6)$$

$$b^{\text{MN}} = S^{\text{MN}} a^{\text{MN}} \quad (3.7)$$

$$\tilde{b} = \tilde{S} \tilde{a}. \quad (3.8)$$

Taking into account that $\tilde{a} = a_1^{\text{MN}}$, $\tilde{b} = b_1^{\text{MN}}$, $a_2^{\text{MN}} = b^c$ and $b_2^{\text{MN}} = a^c$ and substituting accordingly in the system 3.8, it can be deduced:

$$\tilde{S} = s_{11}^{\text{MN}} + s_{12}^{\text{MN}} S^c \frac{s_{21}^{\text{MN}}}{1 - S^c s_{22}^{\text{MN}}}, \quad (3.9)$$

where all the entries are complex numbers for the given position pair $\langle p_1, p_2 \rangle$. Solving for S^c yields:

$$S^c = \frac{\tilde{S} - s_{11}^{\text{MN}}}{s_{22}^{\text{MN}} \tilde{S} - s_{11}^{\text{MN}} s_{22}^{\text{MN}} + s_{12}^{\text{MN}} s_{21}^{\text{MN}}}. \quad (3.10)$$

The calculation is straight forward using the lookup table, given the known position of the capacitors and the measurements from the network analyzer.

The minimization problem $\min_{p_1, p_2} (|\tilde{S}|)$ of the total reflection at the input of the combined network, which represents the maximization of the power transferred to the load, is derived from Equation 3.9. The single-channel case with a matching network of specific topology has a single minimum [21] and is found by the objective function and the use of the lookup tables. Then, the motors are actuated and move the capacitors to the calculated positions. This will be referred as ‘one-jump’ matching in the following. Nevertheless, the calculated reflection coefficient differs from the real one, as mentioned earlier, and is counteracted by the exhaustive neighbor search.

Matching Experiments

The matching network capabilities are tested and verified with both *in-vitro* and *in-vivo* experiments. In the *in-vitro* experiment, the setup is loaded with a phantom of a rectangular container with dimensions $12 \times 12 \times 22$ cm filled with 142 mmol/l of sodium iodide (NaI) diluted in 4 l acetone and TMHD Resolve-Al gadolinium compound (Sigma-Aldrich, St. Louis MO) for setting the relaxation time at approximately 500 msec. According to Yang et al. [51], the conductivity of the phantom is measured to be 3.67 mS/cm and resembles the one of the brain for a 7T system. Acetone has been chosen as solvent due to the lower dielectric constant compared to water. This allows one to concentrate solely on the effects of coil loading, without being distracted by phenomena caused by the formation of standing waves that are expected due to the phantom size. In the *in-vivo* experiments, the focus lies on the lower leg close to the ankle bones, which gives an adequate filling factor and sufficient loading of the surface coils used.

In the conducted experiments, the B_1^+ maps are acquired according to the description of Chapter 2. A reliable selection for the baseline flip angle is 15° , while the block pre-pulse duration is set to 4 msec,

thus slightly longer to the original method in order to increase the feasible flip angle range. The nominal saturation angle is stepping incrementally by 40° in each step, starting from 0° , while the interval between the saturation and excitation pulses is $\Delta T=5.8$ msec and was experimentally found to give good results for the given phantom. The targeted region is a transversal slice of 5 mm thickness located at the middle of the phantom. The FOV is 200×200 mm and the image resolution is set to 64×64 pixels. For the B_0 map, the echo time is set to $\Delta TE=0.5$ msec. Along with every B_1^+ map, a standard gradient-echo image of low flip angle is acquired for image-based comparison. It is worth noting that all preparation phases such as RF gain optimization are turned off.

For the purpose of quantitatively validating the improvement of the power efficiency by automatic matching, an arbitrary coil is automatically matched under a typical scenario. Initially, the coil is matched as routinely done on the bench and is subsequently loaded with the sample. This causes the initial impedance of the coil to change. Following, a B_1^+ map and an image are acquired for the unmatched state. Then, the network analyzer is connected and the automatic matching algorithm is executed in 40-70 seconds on the push of a button. The matching process is followed by a new set of B_1^+ maps and images for the new state.

3.4 Results

Figure 3.5 shows the range of capacitance of the variable capacitor (left y-axis), which varies from 1.6 to 67 pF. The non-linearity of the capacitance range is explained by the effect of the two fictitious capacitors bundled in one capacitor in an in-series fashion. The initial plateau is caused by the electrode's shape, whereas the oscillation of the capacitance occurs due to mechanical imperfections. The right y-axis of Figure 3.5 depicts the standard deviation of the capacitor

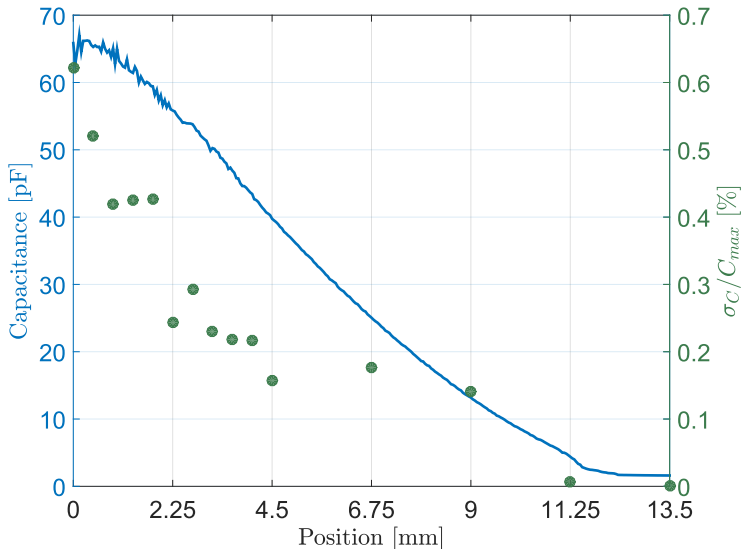


Figure 3.5: The blue line represents the capacitance of the custom-made variable capacitor for its full range. The green dots represent the standard deviation normalized by the maximum capacitance in percentage for a subset of positions for measuring the reproducibility of a capacitance value at a given position.

value at the same position for a number of runs over the maximum value of the capacitor in percentage. It is a figure of merit for the reproducibility of the capacitor values and is obtained by approaching each position from one side for 200 repetitions.

For the determination of the Q-factor and the maximum power the capacitor can withstand, the method of the resonant circuit described before was employed. The Q-factor was found to be 133. For the maximum power, taking into account the cable losses, the resonator was driven with 54 dBm power, whereas further increase of the injected power caused the capacitor to break. Its reflection coefficient was $|\Gamma| = -1.58$ dB, hence the power injected was 76 W.

Given the $Q_{\text{total}}=98$, the voltage that the capacitor can cope with is 2.11 kV.

Concerning the in-bore experiment, the capacitors of the matching network remained intact and there was no sign of damage. The measured forward power was 337 W.

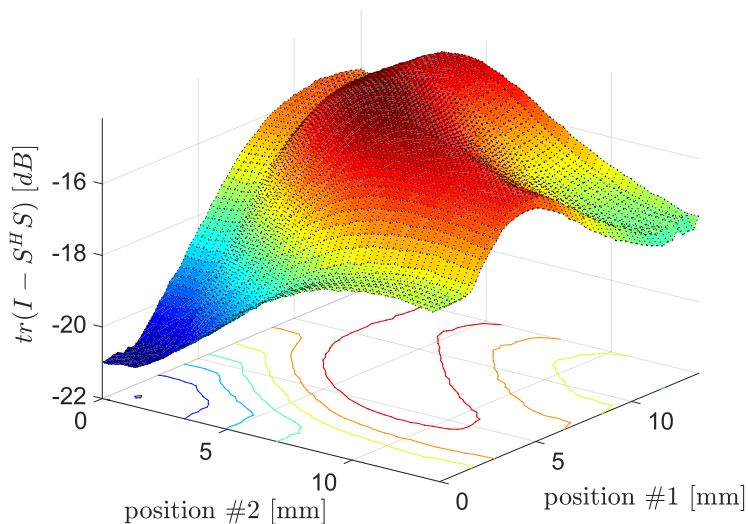


Figure 3.6: The surface depicts the total losses of a matching network, including the microstrip lines printed on the PCB. The losses are calculated by the trace of the matrix $I - S^H S$, where S denotes the total matrix.

Another important figure when the capacitors are bundled to form the matching networks is the network losses. Figure 3.6 illustrates the losses for all position combinations. The net loss of a device with a scattering matrix S is the trace of $I - S^H S$, where H denotes the Hermitian adjoint and I is the identity matrix. The losses of the matching network range between -21.02 and -14.18 dB with an average value of -16.5 dB. These include the microstrip RF traces printed on the PCB. As a result, the matching network is slightly

lossy, with 1-3% of the forward power dissipated to it.

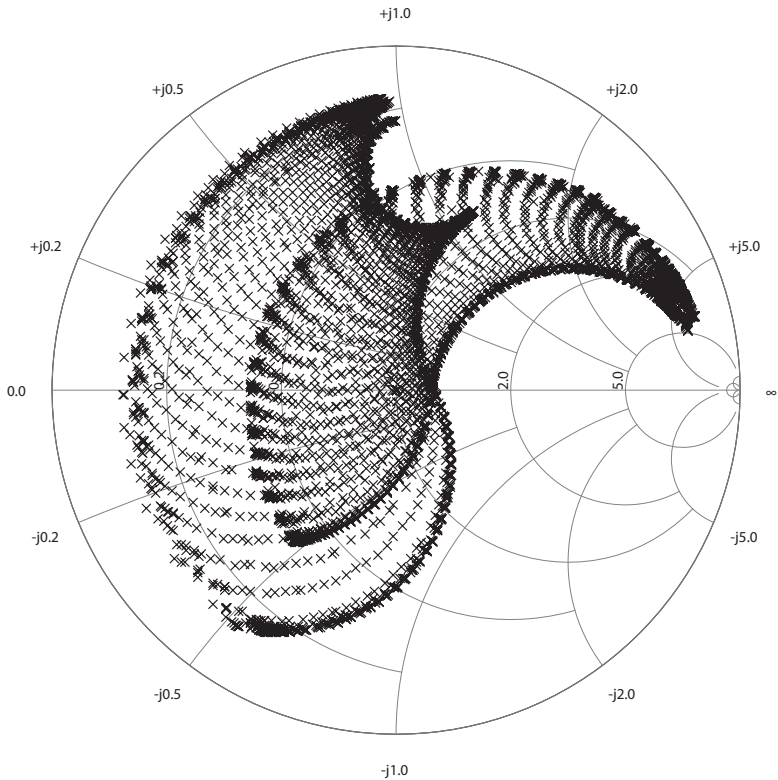


Figure 3.7: Loads that can be matched with the state-of-the-art matching network. The two regions correspond to the two distinct ways the matching network can be connected to the load.

Figure 3.7 illustrates on the Smith chart all coil impedances that can be matched by the matching network. In the case of the matching network, there are two possible network topologies, hence two distinct areas on the plot.

For validating the setup, the automatic matching procedure is performed in line with the aforementioned description by attaching a matchable rectangular coil in the scanner bore. Its dimensions are

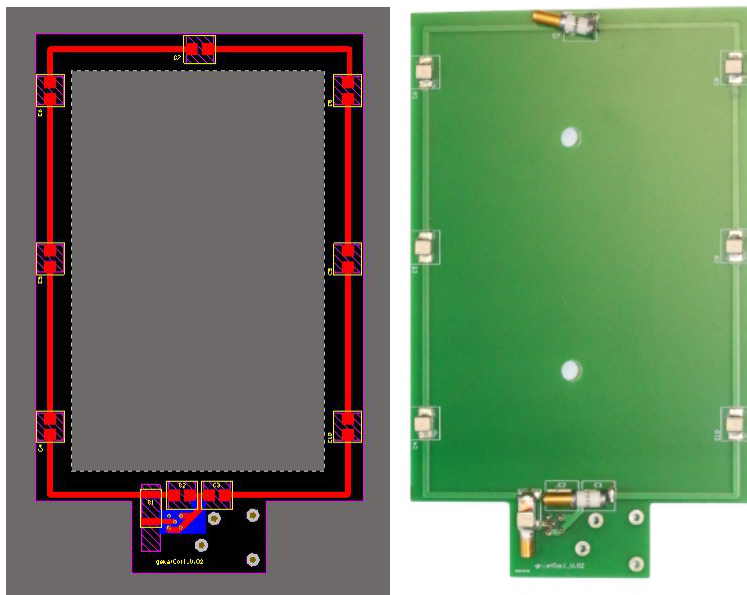


Figure 3.8: Schematic and picture of a single coil element. The fixed high-power capacitors are equidistantly distributed along the PCB printed coil. The balanced matching network is at the input of the coil element at the bottom of the images.

19×12.8 cm and it has its own manual matching network, as shown in Figure 3.8.

At the beginning of the experiment, the coil is loaded with the phantom and the current state represents the ‘unmatched’ case. Subsequently, the automatic procedure matches the coil in the bore. Figure 3.9 shows the reflection coefficient of the input port (S_{11}) for ten arbitrary loading conditions, i.e. ten different phantom positions, while proceeding directly to the gradient descent algorithm, thus skipping the one-step analytical matching procedure.

Figure 3.10 illustrates the S_{11} (left), followed by the one-step analytical matching procedure (middle) and the iterative automatic fine-

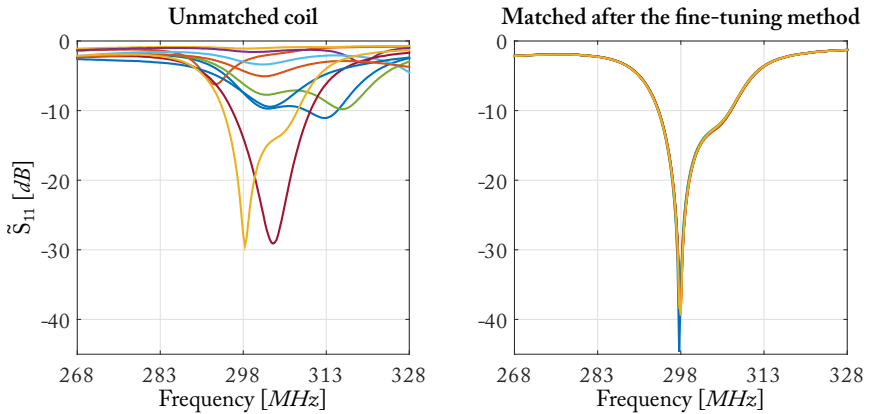


Figure 3.9: Reflection coefficient S_{11} at the input of the matching network. Ten different experiments starting with different initial loading conditions (left figure) and the end result (right figure).

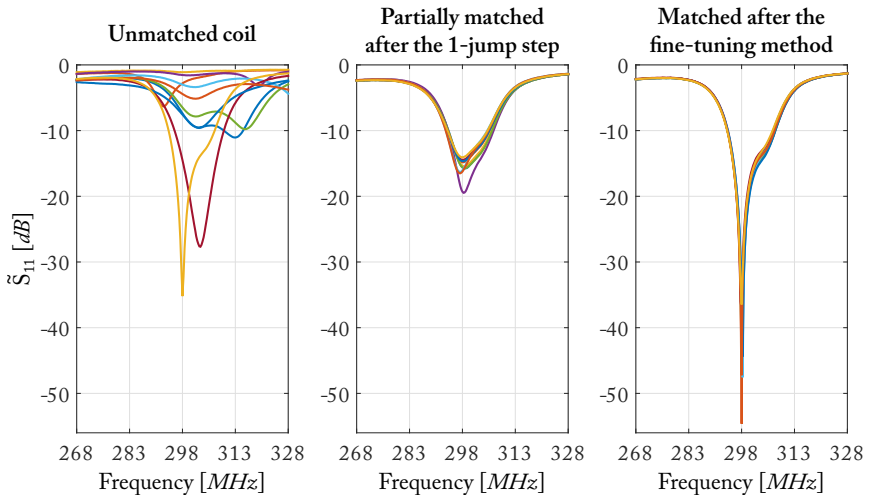


Figure 3.10: Reflection coefficient S_{11} at the input of the matching network. Ten different experiments starting with different initial loading conditions (left figure) and the end result (right), including the intermediate employment of the analytical solution (middle figure).

matching procedure with the aid of the gradient-descent algorithm (right). Both experiments deliver the desired result of matching the coil with a reflection coefficient of -35 dB or less.

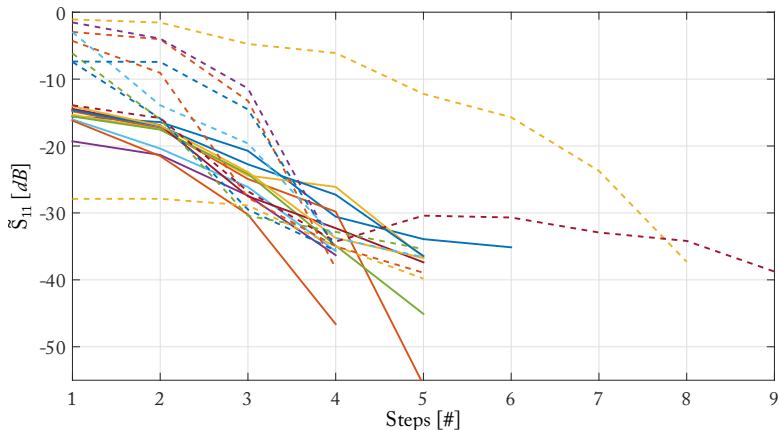


Figure 3.11: Comparison of the number of steps required to exceed the -35 dB threshold of acceptable matching with and without the 1-jump step. The continuous lines correspond to the case of using the 1-jump followed by the fine-tuning method. The dashed lines correspond to the case where the fine-tuning method is employed directly, without the intermediate 1-jump step. Both experiments were repeated 10 times for different loading conditions. As can be seen, the use of the intermediate analytic step is beneficial for speeding up the matching of the coil.

The later experiment, that includes the analytical step procedure, is naturally faster, as the intermediate analytical step brings the system closer to the desired matching condition as shown in Figure 3.11. The precision of the match is governed by the finite resolution of the capacitor and its reproducibility capability.

In the first row of Figure 3.12, the masked B_1^+ maps of the phantom are shown for the ‘unmatched’ (left) and the ‘matched’ case (middle), along with the ratio of the two maps (right), so as to assess the improvement. The S_{11} measurements performed with the network analyzer show an improvement of 10.34%, while the mean improve-

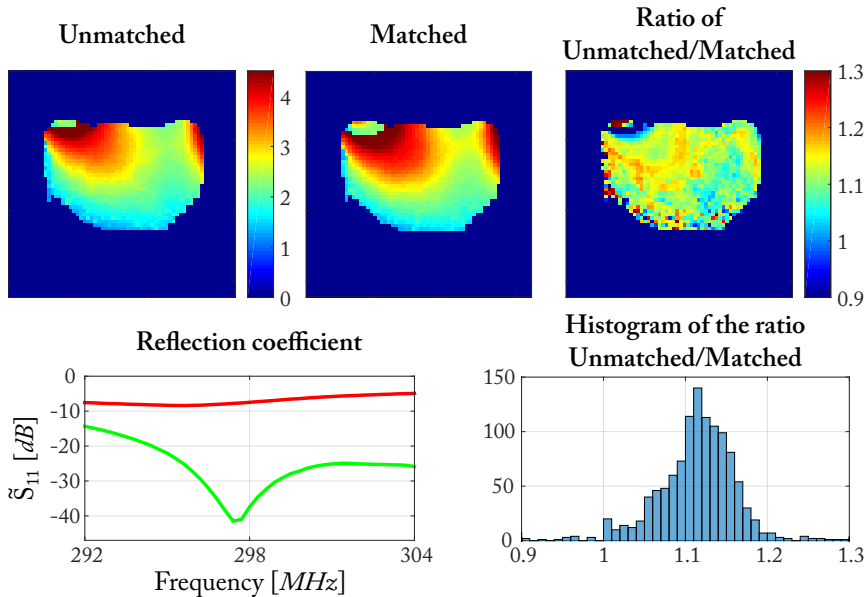


Figure 3.12: The upper left figure depicts the loaded case of the coil with the phantom prior to matching. The upper middle figure shows the result of the matching procedure, while the upper right figure depicts the ratio of the two cases. At the lower left are the readings of the network analyzer, with red depicting the unmatched case and the green the matched case. The lower right figure is the histogram of the matched/unmatched ratio.

ment on per-pixel basis of the B_1^+ maps is 10.33% with a standard deviation of 11% for the region. The former calculation concerns the improvement based on the measurements of the S-parameters, whereas the latter is the mean value of the histogram.

Figures 3.13-3.14 present the *in-vivo* results for the lower leg of a volunteer. As before, the expected improvement based on the impedance measurements is 15.49%, whereas the mean improvement based on the B_1^+ maps is 7.6% with a standard deviation of 13.2% for the masked region where the fat and bone tissue are excluded. The images shown in Figure 3.13 are the corresponding spin-warp

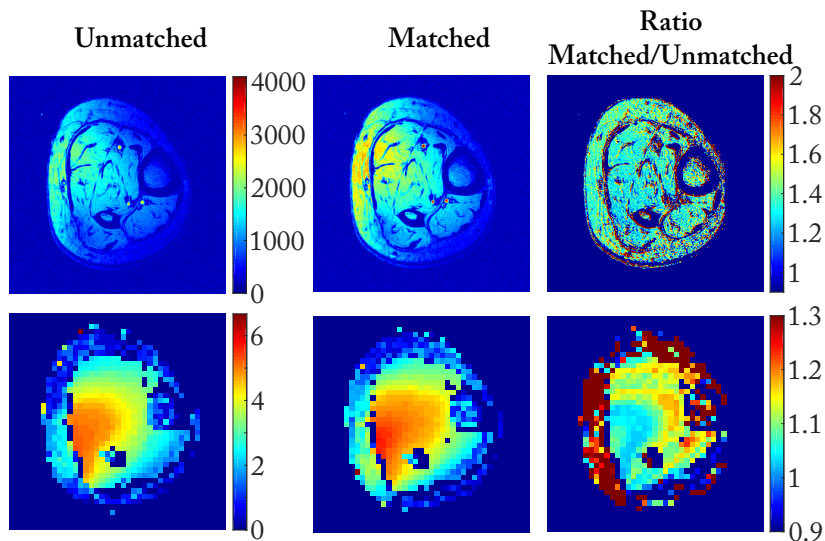


Figure 3.13: *in-vivo* experimental results: The upper row depicts the *in-vivo* MR images, along with the ratio of the change, whereas the lower row depicts the respective B_1^+ maps.

images of the aforementioned B_1^+ maps. Here, the improvement is 37.79% with a standard deviation of 52% for the whole sample region. The enhanced improvement of the MR images as compared to the B_1^+ maps is attributed to the receiving path gain.

3.5 Discussion & Conclusion

The present work addresses the problem of automated maximization of the power transferred to the load by developing a suitable module for automatic matching of a wide range of loading conditions. The approach for solving this problem conceptually consists of two parts, namely the development of a remotely-controlled, variable capacitor, which is the building block of the design, on one hand, and the design of the matching network and the matching procedure, on the other

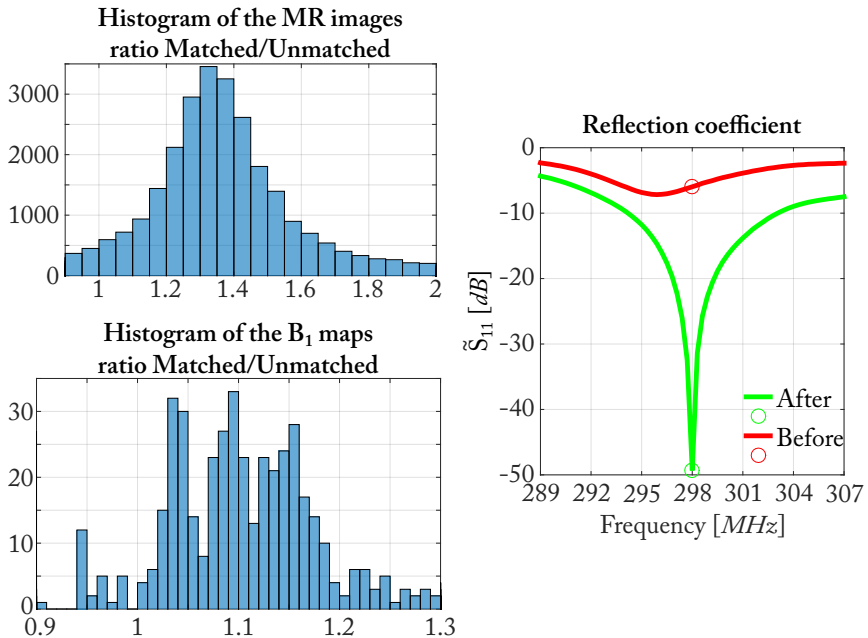


Figure 3.14: *in-vivo* experimental results: The upper histogram corresponds to the ratio of the *in-vivo* images (upper right image of Figure 3.13), whereas the lower histogram corresponds to the ratio of the B_1^+ maps (lower right image of Figure 3.13). The reflection coefficient depicted here refers to the reference plane at the input of the matching network for the two states (unmatched and matched).

hand.

The core challenge of the capacitor's design lies in the competing goals for miniaturization, wide capacitance range and high power handling. The requirement to keep the system as small as possible in order to place it next to the coil, while having a large capacitance range and high dielectric strength favor the selection of a high permittivity material. As a consequence, the use of dielectric material entails a homogeneous electric field, so as to avoid uneven stress and possible break across the cross-section of the material. This addi-

tional prerequisite dictates the planar design of the capacitor.

The selected dielectric material, coupled with the planar design of the capacitor, offers manifold advantages. The high permittivity of the dielectric material allows high ranges of capacitance, hence extending the capacitor's matching capabilities. Furthermore, the use of a dielectric material renders the capacitor of higher dielectric strength per se than air capacitors. Compared with a cylindrical capacitor, the planarity of the design offers increased per unit area of electrode, hence calling for a reduced demand on the dielectric constant of the material. Moreover, the floating electrode provides a fixed connection to the capacitor, thus eliminating a potential undefined impedance caused by the galvanic connection to the movable rod in the case of the cylindrical capacitor. The employment of standard electronic design development tools, along with the reduced amount of conductive material necessary as compared to other capacitor geometries, make the structure lightweight and robust. Lastly, the actuators can be small and integrated in the capacitors, leading to a simpler and of a smaller footprint mechanical design with reduced friction and minimum bearing, which make it nearly maintenance free.

The drawback of the use of high permittivity material is the possibility of the creation of air pockets that could render the capacitors unsafe and prone to breaking even at low power levels. Apart from the change in the electrodes' shape for counteracting this risk, high mechanical precision is required during the production to avoid imperfections that could break the capacitor under stress. Additionally, plating methods could be employed to the fixed electrodes to eliminate the aforementioned possibility.

The inclusion of the feedback loop through the inexpensive optical encoders provides high-precision positioning of the capacitor's electrode. The accurate positioning allows the relaxation of mechanical tolerances and complex calibration procedures of the motors. On

the downside, the closed-loop control poses challenges concerning the fitting and routing of the associated components and cables in a confined space.

Contrary to coil-specific matching networks, the matching network developed by the assembly of the designed variable capacitor pairs has no dependency to the selected coil, thanks to the high range of the capacitors. The module can be used with a large range of available coils.

As far as the losses of the matching network are concerned, there exists a region of positions where the capacitors seem to develop a mode of resonance with an inductive part of the capacitor. However, the phenomenon has negligible implications in terms of power losses. The losses can be further suppressed by the use of a low-loss substrate of the PCB.

Regarding the automatic matching procedure, the introduction of the S-matrix analysis and the respective analytic model enables the one-jump matching. As a result, the matching process is speeded up by directly selecting an appropriate setting in comparison to exclusively heuristic approaches.

Improvements of the matching procedure involve the optimization of the heuristics of the gradient descent algorithm. By taking into account the information from neighboring frequencies provided by the impedance measurement, the convergence of the algorithm towards the matching condition could be accelerated. Additionally, the current model can be further investigated for improvements so as to waive the need of heuristics.

Scaling up the module for the multi-channel case provides a powerful tool for the otherwise highly complex problem. Nevertheless, multi-channel matching poses hardware and algorithmic challenges. There is a need of multiplexing the different channels to the network analyzer and the respective dimensionality problem of the S-parameter

look-up tables. In this sense, variable capacitors and matching networks form the basis for exploring this domain.

Straight-forward application fields involve cases where loading varies, such as posture changes or thermal drifts during longer and demanding scans. Automatic matching is done on a push of a button, whereas a directional coupler could be used to eliminate the nuisance of manually connecting the network analyzer when a matching procedure is required. Concerning fast loading changes such as breathing or heart beating, the developed procedure is currently slow.

The practicality of the automatic matching module in a clinical environment is further evident when incorporating it in the scanning preparation phase for matching coil arrays, which are known to be notoriously difficult to match.

The module's design allows the safe operation under high power output of the RF amplifiers. The implementation of the concept enables quick and highly automated matching under different loading conditions, with minimum user intervention for *in-vivo* experiments inside the bore of a 7T system. The time scale for the matching is considered adequately short and can be scaled without any time cost, if performed in parallel.

Chapter 4

Multiple channel matching system

In the following, the conception and implementation of the multiple channel matching system are presented, based on the adaptive matching principles developed in Chapter 3.

4.1 Multiple channel system description

The capacitor module presented in Chapter 3 serves as the building block of the multiple channel setup, depicted in Figure 4.1. The transmit/receive (TR) system consists of a 4-channel coil array, each channel being a loop coil identical to the others. The array is connected to the first-layer matching network, denoted by MN_1 , which in turn is connected to a 4×4 Butler matrix. Subsequently, a second-layer matching network, MN_2 , is cascaded and the implemented network is connected to four distinct power amplifiers integrated in the scanner and capable of producing 1 kW output power. The network is assembled by using 50 Ohm coaxial cables chosen at lengths other than multiples of $\lambda/4$ so as to prohibit impedance transformation properties of the $\lambda/4$ transformer and are kept as short as the dimensions of the setup allow in order to minimize dissipative losses by standing waves.

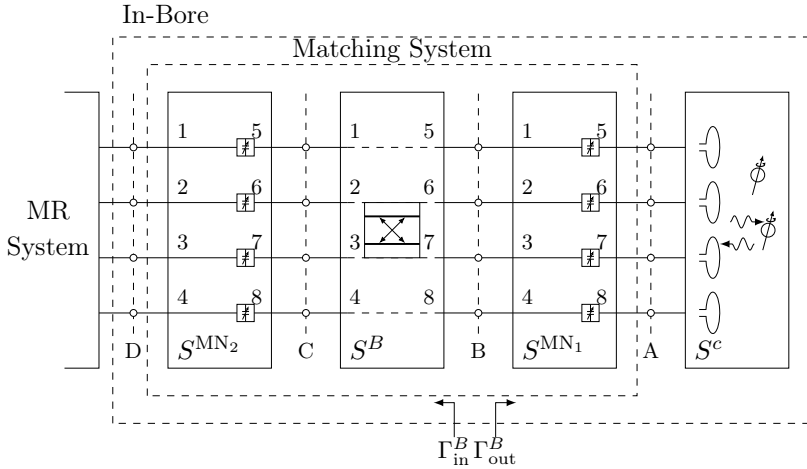


Figure 4.1: Schematic of the multiple channel setup. On the left hand-side lies the MR system, where the power amplifiers responsible for the spin excitation are located. In the bore, the *matching system* is connected to the coil characterized by the matrix S^c . The coil interacts with the environment not only for excitation and sensing, but also electrically. The matching system is composed of two layers of matching networks surrounding the Butler matrix. The reference planes between the distinct parts of the system are labeled *A-D* and are the access points of measuring and characterizing these sub-systems.

The measurement reference planes between the cascaded blocks are sequentially denoted by the capital letters *A-D*, with *A* being the plane between the coil and the first matching network MN_1 . The corresponding input and output reflection coefficients are denoted by $\Gamma_{in/out}^i$, where the superscript i denotes the corresponding reference plane. The total matching network, denoted as *matching system* and enclosed by the inner dashed-line rectangular, comprises of the two layers of matching network and the Butler matrix. The outer dashed-line rectangular corresponds to the part of the RF system located in the bore of the MRI scanner.

Coil array

The coil array is a 4-element circular loop array. The four identical elements are made out of 3.5 mm thick standard FR4 PCB and measure 190×125 mm. The dimensions of the array represent a compromise between fitting a phantom of adequate size for observing wave propagation phenomena and easily placing it in the scanner bore. The size is such that accommodates all cabling requirements of the surrounding instrumentation.

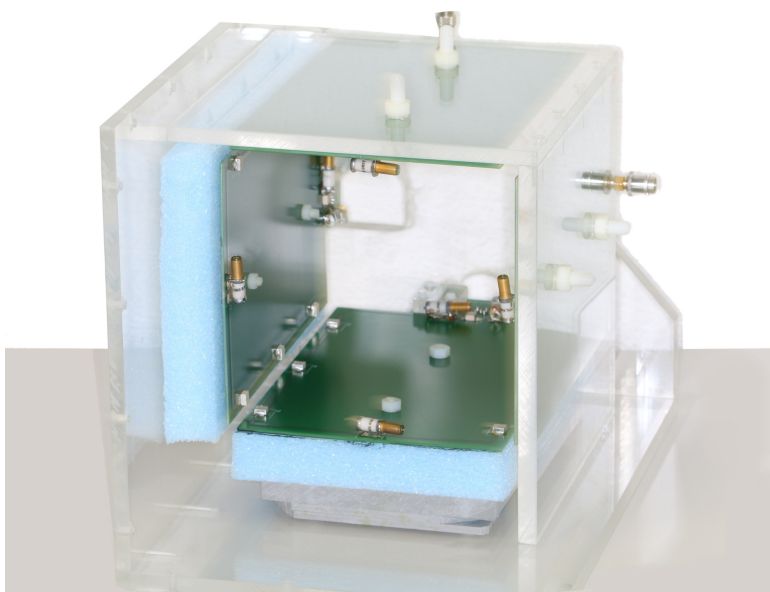


Figure 4.2: Coil array used in the experiments consisting of the elements depicted in Figure 3.8.

Each coil array element is tuned by seven capacitors distributed across its total length. Due to the size of the coil, which approaches the wavelength of the operating frequency, the capacitors are distributed equidistantly forming sections such that each of them is between $\lambda/20$ and $\lambda/10$ long and symmetry is preserved. This choice is

necessary in order to avoid wave phenomena on the coil itself. The high power capacitors (ATC 700C series, New York, US) soldered on the PCB can withhold voltage of 2.5 kV, according to their specifications. The capacitor located in the middle of the inductive loop, opposite to the feeding port, is variable (Voltronics NMAP series, NY, USA) in order to be able to re-tune each individual element in the array formation.

At the port of each element there is an integral matching network consisting of high power air trimmers to match the coil to the 50 Ohm line impedance. The impedance transformation is deemed necessary, for the coil has a very low resistance and an arbitrary reactance upon design, causing the forward wave to be reflected when mismatched.

Finally, each element is balanced in order to minimize currents flowing on the shield of the cable by splitting the capacitors into two groups of equal capacitance and arranging them symmetrically about the symmetry line of the coil. The ground of the RF cable is, thus, connected in the middle of the conductor at the input of the coil. The coils are connected to the rest of the system with a 90° BNC connector soldered on the rear side of the coil.

Following, the coil array elements are assembled and mounted on a rectangular, 5 mm thick PMMA case in equal distances from each other. At the formation of the coil array, the individual resonant elements couple and their resonance frequency changes, showing a characteristic double-peak frequency response about the frequency of interest. These modes are mitigated by iterative retuning with the use of the variable capacitor of each coil array element. When all four elements are tuned and matched on the bench with a calibrated network analyzer, the array is ready to use. Typical values of the reflection coefficient of the individual elements of the matched array are -15 to -20 dB.

For the purposes of the present work, no provision for avoiding coupling of the coil array has been made, in consideration of a typical

scenario rather than an ideal case. In the long run, the aim is the investigation of close coupling in coil arrays and their effects.

A fundamental property of the circular coil array concerns its symmetry, that allows its modeling as a circulant matrix in the scattering parameter nomenclature. The definitions and theorems of circulant matrices relevant to the present work are presented in the Appendix.

Matching network layers

The two matching network layers are formed as an aggregation of the matching network, whose mechanical and electrical characteristics are presented in Chapter 3. Each matching network layer, MN_i , consists of 2 PMMA casings, each enclosing two separate matching networks.

Butler Matrix

A Butler matrix is a feed network of hybrid dividers and phase shifters conceived by Butler and Lowe [52] to perform beam-forming of antenna arrays. Beam-forming is the spatial steering of an antenna array beam to multiple directions concurrently. A signal at a given input port produces signals of equal amplitude at the output with a constant phase difference between two consecutive output ports, thus creating a beam at a specific angle in space. As the same applies to all individual ports, the Butler matrix can be driven with independent signals, that create any possible linear combination of the output signals.

By definition, the Butler matrix is a linear, passive $N \times N$ network introduced between the N outputs of the power amplifier and the N inputs of the antenna array for performing the spatial fast Fourier transform (FFT) in the analog domain of the antenna input [53, 54]. An $N \times N$ Butler matrix gives an aperture distribution of an antenna

array, which is derived by the superposition of each beamlet A_{nm} when the individual input m is driven with amplitude A_m . Thus,

$$A_{nm} = \frac{A_m}{\sqrt{N}} e^{-i\frac{2\pi nm}{N}}, \quad (4.1)$$

which in turn yields the array excitation

$$A_n = \sum_m A_{nm} = \sum_m \frac{1}{\sqrt{N}} A_m e^{-i\frac{2\pi nm}{N}}. \quad (4.2)$$

Formula 4.2 is the FFT of the input A_m [55, 56].

Butler matrix uses in multiple channel matching

In the advent of parallel MR, the Butler matrix was used for mode generation in a coil array. Thanks to its property to perform the FFT, it can form an orthogonal basis of the excitation pulses with a reduced set of transmit amplifiers [57]. An immediate advantage of the generated modes is the ability of tailoring the B_1^+ distribution to target a specific region in the sample, along with the mitigation of B_1^+ inhomogeneities primarily associated with high-field MR.

According to Theorem 2 of the Appendix concerning circulant matrices, any circulant matrix and, consequently, the S-matrix of the circular coil array used in the present work is diagonalizable by the Fourier transform. This motivates the use of a Butler matrix in the array matching setup, since the S-matrix transformation allows the independent treatment of channels thereafter.

Butler matrix implementation

A Butler matrix can be implemented using either 90° or 180° hybrids. The use of 90° hybrids results in total phase shifts at the output of odd multiples of π and in matrix symmetry, whereas 180° hybrids

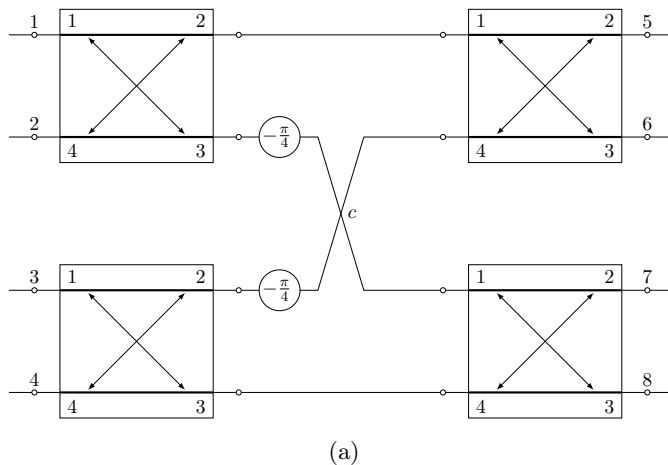


Figure 4.3: (a) Butler matrix schematic and (b) implementation. The Butler matrix is composed of 90° hybrids. The $-\pi/4$ phase shift is realized by a transmission line of appropriate length. The BNC inputs of the Butler matrix are on the bottom side of the board.

yield even multiples of π and asymmetrical matrices [58, 59, 60, 61]. The number of hybrids required in any case for an $N \times N$ matrix is $\frac{N}{2} \log_2 N$.

For the purposes of the present work, the 4×4 Butler matrix, shown in Figure 4.3, was built using 90° hybrids (Anaren Microwave, Syra-

cuse NY, US) and semi-rigid transmission lines (Huber & Suhner, Herisau, CH) of appropriate length for the -45° phase shifting. The hybrids were mounted on a FR4 PCB and in cases where no phase shifts were required, the corresponding inputs and outputs were soldered together. The delay of both semi-rigid lines was measured by a transmission measurement with a calibrated network analyzer and $\pm 0.1^\circ$ accuracy. The lines were bended in line with their specifications and soldered to the corresponding terminals. The shield braids were fused with solder to reduce loop paths and, consequently, sources of inductive currents. Finally, 90° BNC connectors were mounted directly to the inputs and outputs of the hybrids, on the rear side of the PCB.

In terms of its electrical characteristics, the Butler matrix was measured and the trace($I_8 - S_{\text{but}}^H S_{\text{but}}$) was found to be 0.3538. Given that a totally lossy system described by an 8×8 S-matrix has a value of 8, the losses are considered low.

Matching strategy

The matching strategy consists of random and deterministic steps, as the large search space of the optimization problem prohibits any exhaustive search approach. In the present work, a Monte Carlo method divides the problem into manageable sub-problems, with their domains searched exhaustively.

The experiment is initiated with the generation of a set of random seed vectors. Each vector element corresponds to the position of a single capacitor. For every seed vector, the algorithm optimizes, for the given objective function, one capacitor after the other by traversing all its positions. The change of a capacitor position invalidates all previous optimizations due to coupling. Therefore, the capacitors are optimized iteratively until a stable position is found.

Algorithm 1 Pseudo-code of the matching strategy.

Initial state: The unloaded coil is manually matched at actualPosition.

Input: Select objective function for the matching and number of seeds.

Output: Matched system.

```

1: for seedi ← 1 . . . n do                                ▷ seedi is a random position vector
2:   arbitraryPosition ← seedi
3:   repeat
4:     for capacitori ← 1 . . . c do
5:       Initialize  $\tilde{S}_{\text{best}}$  accordingly
6:       for positioni ← 1 . . . 300 do
7:         combinedMatrix ←  $S^{\text{MN}}$  from the lookup tables
8:         Calculate objective function analytically
9:         if  $\tilde{S}$  better than  $\tilde{S}_{\text{best}}$  then
10:           $\tilde{S}_{\text{best}} \leftarrow \tilde{S}$ 
11:          Store all necessary data
12:          Store the position of your best result
13:        end if
14:      end for
15:      Go to  $\tilde{S}_{\text{best}}$ 
16:    end for
17:    until position vector is the same as in previous iteration.
18:    if  $\tilde{S}$  better than  $\tilde{S}_{\text{best}}$  then
19:       $\tilde{S}_{\text{best}} \leftarrow \tilde{S}$ 
20:      Store all necessary data
21:    end if
22:  end for
23:  ▷ So far there was no actual movement. Only computations.
24:  actualPosition ← position of  $\tilde{S}_{\text{best}}$ 
25:  repeat
26:    for capacitori ← 1 . . . c do
27:      for all neighboring positions do
28:        Move capacitori
29:        Measure  $\tilde{S}$  and record it
30:      end for
31:      actualPosition ← best neighboring position
32:    end for
33:  until threshold is met.

```

This procedure is performed on all seed vectors. The lookup tables enable the execution of the optimization computationally, without involving any motion of the capacitors.

Following, the motors are actuated and the capacitors move to the calculated positions. Thereafter, a gradient descent algorithm finds the local optimum by checking all neighboring positions. The neighborhood search is performed to correct for mechanical imperfections or measurement noise that affect the preceding optimization. The gradient descent algorithm halts when a threshold condition is met.

The matching strategy is summarized in the pseudo-code shown in Algorithm 1.

4.2 Objective functions

In the following, the mathematical formulations of the objective functions implemented and used in the present work are presented. The objective functions are based on the S-matrices of the matching network and the coil and, therefore, account for the array coupling. The objective functions are the following:

1. the minimization of the reflection at the input of the matching system, denoted by $\min(\tilde{S})$,
2. the minimization of losses in the matching network, denoted by $\min(\text{loss})$ and
3. the maximization of power delivery to the load, denoted by $\max(\text{P2L})$.

Minimum reflection

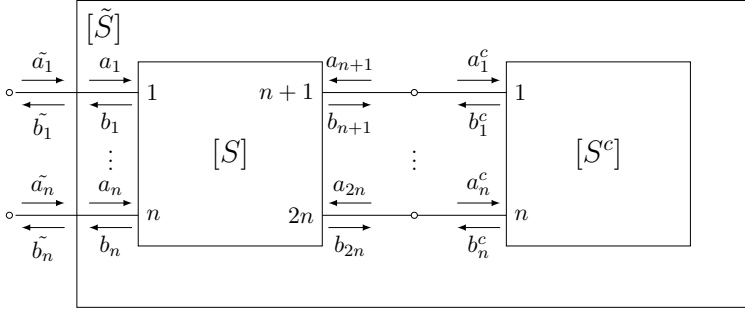


Figure 4.4: Multiple channel S-matrices. S^c is the characteristic S-matrix of the coil, S captures the total matching system and \tilde{S} is the S-matrix of the combined system. The incident and reflected waves to the ports are denoted by a and b , correspondingly. Indices denote the corresponding port and superscripts denote the sub-system.

Let a and b denote the incident and reflected waves to the ports respectively, while accents or superscripts define different devices as depicted in Figure 4.4.

Hence, the following equations hold:

$$b = S a \quad (4.3)$$

$$\tilde{b} = \tilde{S} \tilde{a} \quad (4.4)$$

$$b^c = S^c a^c. \quad (4.5)$$

For the incident and reflective waves, the following equations hold when the reference impedance is real:

$$a_i = \tilde{a}_i \quad \text{for } i = 1 \dots n \quad (4.6)$$

$$a_{n+i} = \tilde{b}_i^c \quad \text{for } i = 1 \dots n \quad (4.7)$$

$$b_i = \tilde{b}_i \quad \text{for } i = 1 \dots n \quad (4.8)$$

$$b_{n+i} = \tilde{a}_i^c \quad \text{for } i = 1 \dots n. \quad (4.9)$$

The goal is to determine $[S]$ when $[\tilde{S}] = 0$. This holds when the load $[S^c]$ is matched, i.e. $s_{ii}^c = 0, \forall i$ and represents the reflectionless matching.

Concerning the S-matrix of the matching network, $[S]$, the following hold:

1. S is lossless, i.e. $S^T S^* = I$, with I being the identity matrix,
2. S is reciprocal, i.e. $S_{ij} = S_{ji}, \forall i, j$ and
3. S is passive, i.e. $|S_{ij}| \leq 1, \forall i, j$.

Equation 4.3 yields:

$$\begin{aligned}
 b &= S a \iff \\
 \begin{bmatrix} \tilde{b} \\ a^c \end{bmatrix} &= S \begin{bmatrix} \tilde{a} \\ b^c \end{bmatrix} \iff \\
 \begin{bmatrix} \tilde{b} \\ a^c \end{bmatrix} &= S \begin{bmatrix} \tilde{a} \\ S^c a^c \end{bmatrix} \iff \\
 \begin{bmatrix} \tilde{b}_1 \\ \vdots \\ \tilde{b}_n \\ a_1^c \\ \vdots \\ a_n^c \end{bmatrix} &= \begin{bmatrix} s_{11} & s_{1n} & s_{1,n+1} & s_{1,2n} \\ & \ddots & & \\ & & & \\ \hline s_{n1} & s_{nn} & s_{n,n+1} & s_{n,2n} \\ \hline s_{n+1,1} & s_{n+1,n} & s_{n+1,n+1} & s_{n+1,2n} \\ & \ddots & & \\ s_{2n,1} & s_{2n,n} & s_{2n,n+1} & s_{2n,2n} \end{bmatrix} \begin{bmatrix} \tilde{a}_1 \\ \vdots \\ \tilde{a}_n \\ [S^c a^c] \end{bmatrix}.
 \end{aligned}$$

The block sub-matrices can be denoted as:

$$\begin{aligned}
 S_{I,I} &= \begin{bmatrix} s_{11} & & s_{1n} \\ & \ddots & \\ s_{n1} & & s_{nn} \end{bmatrix} \\
 S_{I,II} &= \begin{bmatrix} s_{1,n+1} & & s_{1,2n} \\ & \ddots & \\ s_{n,n+1} & & s_{n,2n} \end{bmatrix} \\
 S_{II,I} &= \begin{bmatrix} s_{n+1,1} & & s_{n+1,n} \\ & \ddots & \\ s_{2n,1} & & s_{2n,n} \end{bmatrix} \\
 S_{II,II} &= \begin{bmatrix} s_{n+1,n+1} & & s_{n+1,2n} \\ & \ddots & \\ s_{2n,n+1} & & s_{2n,2n} \end{bmatrix},
 \end{aligned}$$

which yields:

$$\tilde{b} = S_{I,I}\tilde{a} + S_{I,II}S^c a^c \quad (4.10)$$

$$a^c = S_{II,I}\tilde{a} + S_{II,II}S^c a^c. \quad (4.11)$$

Equation 4.11 yields:

$$\begin{aligned}
 a^c - S_{II,II}S^c a^c &= S_{II,I}\tilde{a} \iff \\
 (I - S_{II,II}S^c)a^c &= S_{II,I}\tilde{a} \iff \\
 a^c &= (I - S_{II,II}S^c)^{-1}S_{II,I}\tilde{a}. \quad (4.12)
 \end{aligned}$$

Combining Equations 4.10 and 4.12 results in:

$$\begin{aligned}
 \tilde{b} &= S_{I,I}\tilde{a} + S_{I,II}S^c a^c \\
 \tilde{b} &= S_{I,I}\tilde{a} + S_{I,II}S^c(I - S_{II,II}S^c)^{-1}S_{II,I}\tilde{a} \\
 \tilde{b} &= \underbrace{\{S_{I,I} + S_{I,II}S^c(I - S_{II,II}S^c)^{-1}S_{II,I}\}}_{\tilde{S}} \tilde{a}.
 \end{aligned}$$

The formulation of reflectionless matching is:

$$\begin{aligned}\tilde{S} \stackrel{!}{=} [0] &= S_{I,I} + S_{I,II}S^c(I - S_{II,II}S^c)^{-1}S_{II,I} \implies \\ S_{I,I} &= -S_{I,II}S^c(I - S_{II,II}S^c)^{-1}S_{II,I}.\end{aligned}\quad (4.13)$$

Taking into consideration the equality $S_{II,I} = [S_{I,II}]^T$, Equation 4.13 transforms to:

$$S_{I,I} = -S_{I,II}S^c(I - S_{II,II}S^c)^{-1} [S_{I,II}]^T. \quad (4.14)$$

Equation 4.14 minimizes reflections at the input of the combined system by means of the lookup tables and constitutes the objective function of minimum reflection.

Minimum losses in the matching network

Referring to Figure 4.4, the total system absorbs maximum power when $\text{trace}(I - \tilde{S}^H \tilde{S})$ is maximum. Accordingly, the losses in the matching network are minimum when $\text{trace}(I - S^H S)$ nulls. Combining both optimization criteria yields

$$\min \left(\text{trace}(\tilde{S}^H \tilde{S}) - \text{trace}(S^H S) \right). \quad (4.15)$$

Formula 4.15 represents the objective function of minimum losses in the matching system.

Maximum power to the load

Referring to Figure 4.4, the following hold:

$$a^c = b_{II} = \begin{bmatrix} b_{n+1} \\ \vdots \\ b_{2n} \end{bmatrix}_{4 \times 1} = \begin{bmatrix} S_{II,I} & S_{II,II} \end{bmatrix}_{4 \times 8} \cdot a_{8 \times 1} \quad (4.16)$$

and

$$\begin{aligned}
 \tilde{b} &= b_I = \begin{bmatrix} b_1 \\ \vdots \\ b_n \end{bmatrix}_{4 \times 1} = \begin{bmatrix} S_{I,I} & S_{I,II} \end{bmatrix}_{4 \times 8} \cdot a_{8 \times 1} = \\
 &= S_{I,I} \cdot a_I + S_{I,II} \cdot a_{II} = \\
 &= S_{I,I} \cdot a_I + S_{I,II} \cdot b^c = \\
 &= S_{I,I} \cdot a_I + S_{I,II} \cdot S^c a^c.
 \end{aligned} \tag{4.17}$$

Solving Equation 4.17 for a^c yields

$$\begin{aligned}
 a^c &= (S_{I,II} S^c)^{-1} \cdot (\tilde{b} - S_{I,I} a_I) = \\
 &= (S_{I,II} S^c)^{-1} \cdot (\tilde{S} \tilde{a} - S_{I,I} a_I) = \\
 &= (S_{I,II} S^c)^{-1} \cdot (\tilde{S} a_I - S_{I,I} a_I) = \\
 &= \underbrace{(S_{I,II} S^c)^{-1} \cdot (\tilde{S} - S_{I,I})}_{X} a_I
 \end{aligned} \tag{4.18}$$

and therefore

$$a^c = X a_I. \tag{4.19}$$

The maximum net power transferred to the coil is the sum of power at each port. Since the real power submitted into port i of any network is equal to $|a_i|^2 - |b_i|^2$, the net power delivered to the 4-port coil is

$$P^c = \sum_{i=1}^4 (|a_i^c|^2 - |b_i^c|^2). \tag{4.20}$$

The matrix form of Equation 4.20 is

$$P^c = (a^c)^H a^c - (b^c)^H b^c. \tag{4.21}$$

Substitution of Equation 4.19 to Equation 4.21 gives

$$P^c = a_I^H X^H X a_I - a_I^H X^H (S^c)^H S^c X a_I. \tag{4.22}$$

Taking the trace of P^c and considering its additive property, the net power delivered to the coil array is given by

$$\hat{P} = \text{tr}(X^H X) - \text{tr}(X^H (S^c)^H S^c X). \quad (4.23)$$

Thus, the objective function is given by the formula:

$$\max_{\text{over } S} \hat{P}. \quad (4.24)$$

The latter optimization criterion is assumed to outweigh the criterion of minimum reflections at the input of the matching network and the criterion of minimum losses in the matching network, as it represents a combination of the two. It ensures that power incident to the input ports will be transferred to the output ports at the maximum, while the losses are concurrently minimized.

Chapter 5

Evaluation of matching strategies

An array matching system consists of both the physical devices and the logic dedicated to control these devices. The matching efficiency depends on both aspects, which act complementary to each other. The control logic can be further broken down into two categories: The first one includes the logic that controls the low-level electronics, whereas the second refers to the logic relevant to the matching problem.

In the present chapter, the focus lies on the previously presented objective functions, in combination with the proposed algorithm. The performance of the array matching system is explored for a set of typical matching scenarios, which provide insight to the system and reveal potential shortfalls. To this end, test cases for the input of the matching algorithm are presented and validated. Two types of simulations are performed for validation purposes. The first aims to provide insights to the behavior of the matching system. A set of scattering parameter surfaces derive from the combination of different array loading conditions and different states of the matching network. The second simulation type aims to measure the algorithmic performance. To achieve this goal, a Monte Carlo simulation is employed and performance metrics are devised. They include the optimal values returned by the objective functions, the vectorial dis-

tances between the initial and final positions, the average translational distance of each individual capacitor and the average number of the required iterations until algorithm termination. These metrics grade the matching performance both in terms of quality and speed.

5.1 Methods

5.1.1 Simulation setup

The topology of the network is depicted in Figure 4.4 for both simulation types. The matching system consists of the two layers of matching network surrounding the Butler matrix, as presented in Section 4.1. This results in a setup of 16 variable capacitors and their corresponding lookup tables. The combined S-matrices are calculated as presented in Chapter 4. The 300-step capacitor resolution generates a search space of size 300^{16} . In order to make the simulation computationally tractable, a 6-fold resolution reduction is performed for every capacitor, reducing its size to 50^{16} . This is permitted by the smoothness of capacitance as a function of its electric field area.

For the Monte Carlo simulation, a set of 10^7 random inputs called seeds is generated. The simulation performs, in accordance to Algorithm 1, the iterative sub-space exhaustive search for all seed points, followed by the gradient descent in the neighborhood of the optimum returned by the preceding algorithmic step. The optima result from the previously presented objective functions:

1. *minimum reflection* at the input of the matching system, denoted by $\min(\tilde{S})$,
2. *minimum losses* in the matching system, denoted by $\min(\text{loss})$,
and

3. *maximum power* delivered to the load, denoted by $\max(\text{P2L})$.

For both simulation types, the capability to synthesize the measured S-matrices for all states of the matching network allows their execution entirely on a computer.

5.1.2 Scattering parameter surfaces

The scattering parameters relevant to the present work reside on multidimensional surfaces. The shape of these surfaces changes when a scattering parameter alters. This behavior is owed to coupling and renders depiction of the surfaces difficult, even when dimensionality allows it. In the following, the shapes of various scattering parameters are visualized in a reduced sub-space. The 16D dimensional space is reduced to a 2D sub-space, where the scattering parameters are functions of two capacitors. The capacitors are randomly selected and the initial selection is kept throughout the simulation in order to maintain comparability. The random choice of the capacitor pair waives any biasing to channel specific observations. The presence of the Butler matrix further reduces this possibility due to the mixing of the waves in the system. Hence, the depictions of the scattering parameters remain generic visualizations of the system. Therefore, they enable key observations about the behavior of the scattering parameters in a generic case. The roughness of the depicted surfaces reveals the complexity of the problem. Gaining insight of the problem is crucial for optimizing aspects of algorithmic design that will boost its performance.

The test cases for the following simulation are a combination of the cases of the actual experiment. The simulation is performed for all objective functions when the coil is either loaded or unloaded. Moreover, the simulation is performed for two distinct cases. In the first case, the initial position vector corresponds to the matched condition in terms of minimum reflection. In the second case, a random

initial position vector is chosen and the state is called unmatched. For both cases, the previously described selected capacitors produce the surface for their full ranges.

In summary, the test cases examined for each of the three objective functions are the following:

1. matched and unloaded,
2. matched and loaded,
3. unmatched and unloaded and
4. unmatched and loaded.

5.1.3 Monte Carlo simulation metrics

The results of the Monte Carlo simulation for all objective functions are statistically evaluated by means of their distribution. The distribution is a figure of merit for the selection of the experiments' random input size. Moreover, the stability of the algorithm for each of the objective functions can be measured on this basis as well. Finally, the number of histogram modes is indicative of each objective function's capability to find the global optimum and avoid local optima.

Each simulated result is identified by the pair of the optimum value and the corresponding position vector. This pair is unique. The distance between the initial random position and the final position constitutes an additional metric. Statistics about the size of the multidimensional ball enclosing the cloud of the simulated position outcomes measure the actual search space and can accelerate the discovery of the optimum.

When focusing on a single capacitor, the information revealed from the simulated position span is an indication of its weight for finding

the optimum. Prior knowledge of this weight can accelerate the optimum discovery by optimizing the capacitor optimization sequence dictated by the weight.

Finally, the number of steps until the termination of the iterative sub-space search is a direct indicator of the convergence speed for a given objective function. A single iteration tests all capacitors over their total position span against the given objective function. This amounts to the most expensive calculation of the simulation, as it scales with the random input size.

5.2 Results

5.2.1 Scattering parameter surfaces

Minimum reflection

The scattering parameters of the S-matrix at the input of the matching network are depicted for the combination of the cases loaded/unloaded and matched/unmatched, as described previously.

Figures 5.1-5.2 correspond to the matched case when the coil is unloaded and loaded respectively. The total range of the two randomly selected capacitors generates a surface for each element of the matrix \tilde{S} . The lower triangle elements are omitted due to the symmetry of the matrix.

The initial matching is located at position vector $pos_{\text{init.}} = (34, 37)$. The reflection coefficients for this position have values well below -20 dB for s_{11} and s_{44} , whereas s_{22} and s_{33} are approximately at -15 dB. The quality of matching for s_{22} and s_{33} can be explained by the coupling, as seen from the scattering coefficient s_{23} , that creates additional reflections, which add up destructively. With the exception

of s_{23} , all off-diagonal elements are decoupled, with decoupling well below -15 dB.

The difference between Figure 5.1 and Figure 5.2 is the loading of the coil. The matching condition for position $pos_{init.} = (34, 37)$ is either completely lost or matching quality has principally worsen. Loading has higher impact on port 1, while the other ports preserve the shape of the surfaces, but with pronounced losses in terms of reflection. Moreover, port 2 shows relatively low sensitivity to loading compared to port 4, where loading causes s_{44} to shift. Coupling increases as expected, thus degrading the overall efficiency of the system.

In terms of smoothness, the surfaces of the diagonal elements have several local optima that cannot be resolved solely with a gradient descent method. This holds for both the unloaded and loaded case. For example, focusing on s_{33} and s_{44} , a gradient descent method may end up in a sub-optimal minimum due to the dichotomous ridge of s_{33} or the local maximum found in the valley of s_{44} . On the contrary, this does not hold for the off-diagonal elements, where the surfaces are more smooth and contain an observable single minimum.

The sequence that capacitors are optimized impacts the end result. It can be observed that the minimum for this pair would depend on the order the capacitors were evaluated against the objective function.

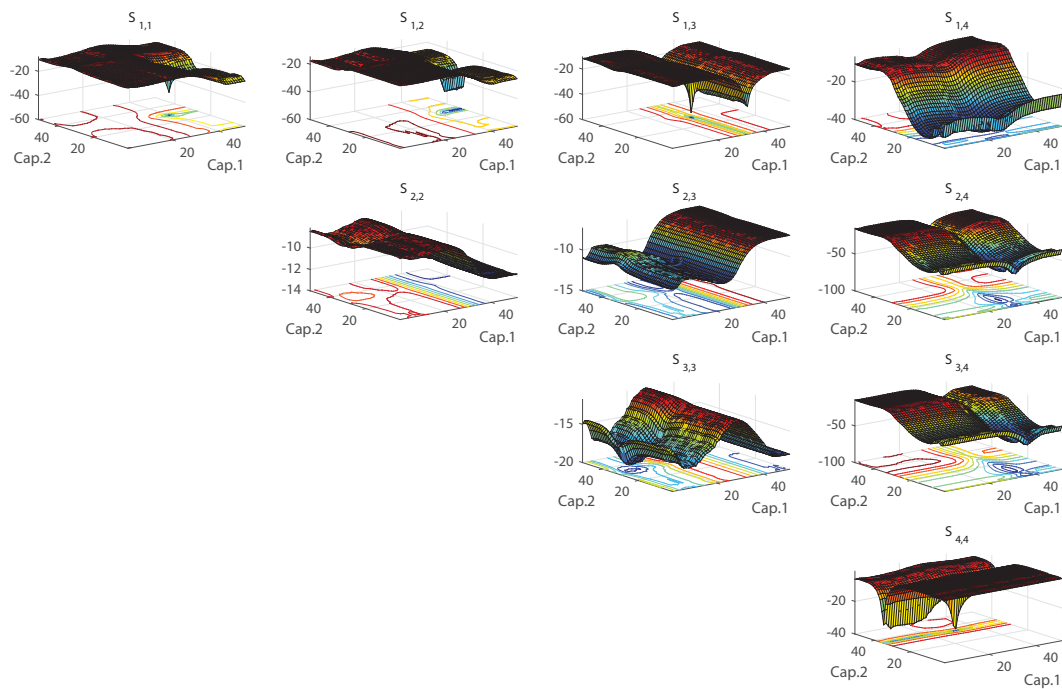


Figure 5.1: Roughness of the S-parameters at the input of the matching system for the full span of two random capacitors of an initially manually matched *unloaded* coil. Comparing to Figure 5.2 representing the loaded case it is noticeable that the matching either vanishes or shifts drastically. Coupling in Figure 5.2 is more pronounced, even though more power is reflected, as can be noticed by the diagonal elements.

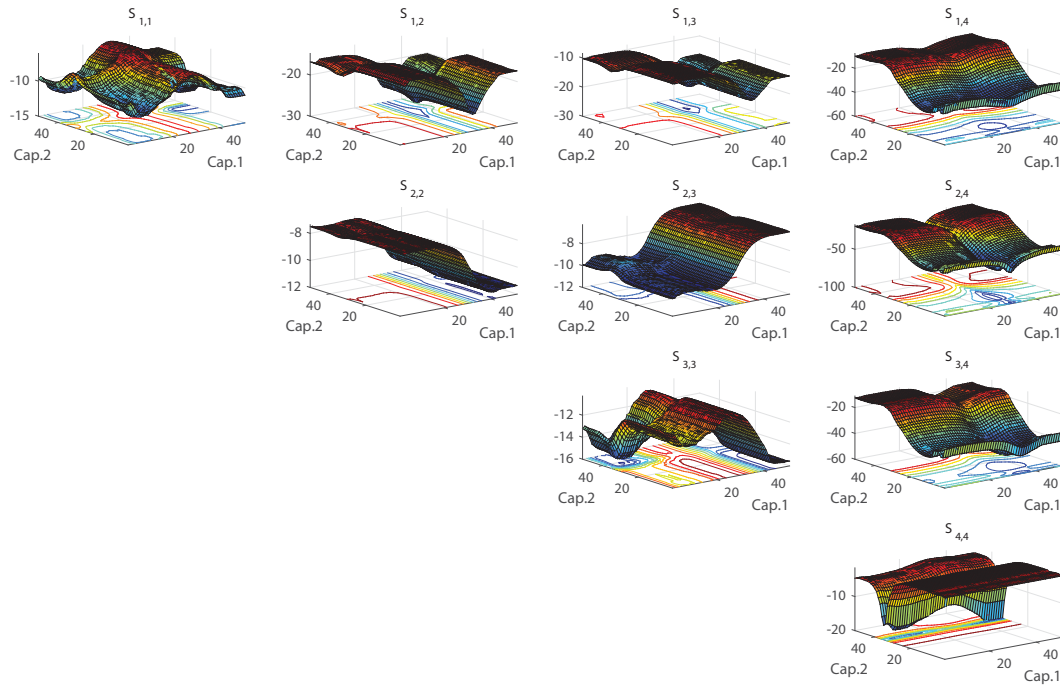


Figure 5.2: Roughness of the S-parameters at the input of the matching system for the full span of two random capacitors of an initially manually matched *loaded* coil. It can be deduced that the chosen pair of capacitors has a higher impact on port 1 compared to port 2, as the change of s_{11} is more severe than that of s_{22} , where only mild changes are noticed. Moreover, capacitor No.2 has little effect on s_{22} , which shows the relatively low sensitivity of the port to the capacitor No.2. On the contrary, only slight changes of the positioning of capacitor No.2 largely affect the reflection coefficient s_{44} .

Figures 5.3-5.4 depict the surface plots of the same array under the same loading conditions as previously. The difference lies in the position vector, which is in this case random, as opposed to the previous position that was obtained after matching.

For the current case, the system is mismatched and totally reflective, as observed from the reflection coefficients of all four ports. Only port 4 allows some power flow into the system for a range of capacitor positions. Since no power makes it into the system, coupling remains very weak for the unloaded coil. When the coil is loaded, coupling increases owing to the increased capacitive coupling through the sample.

As far as flatness is concerned, the surfaces of the scattering coefficients are relatively flat and lack complexity. This occurs due to the very low power present in the system. This also translates to large support areas, where the reflection coefficients are optimal. Nevertheless, their values are high and cannot match the system. The sudden changes of the diagonal coefficients at the marginal positions of the capacitors indicate that the current set of capacitors has little effect on finding a matching condition. Nevertheless, capacitor No.2 has a prevailing effect on port 4 compared to capacitor No.1, as seen by s_{44} , whereas the exact opposite holds for port 3. The observations conclude that other capacitors need to be optimized before considering the selected ones in order to match the system.

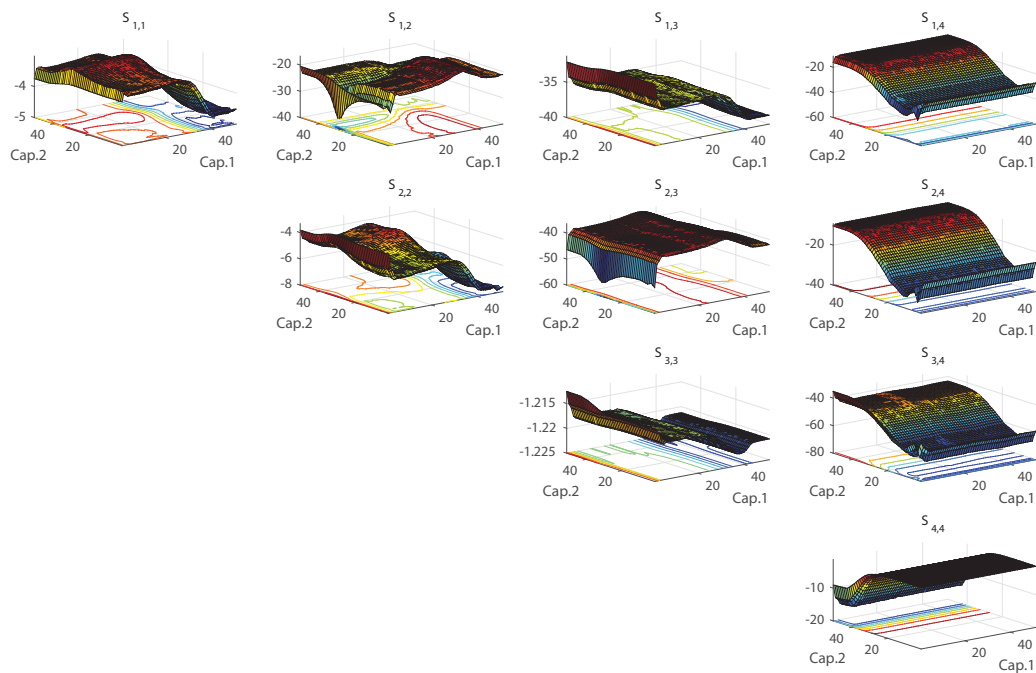


Figure 5.3: Roughness of the S-parameters at the input of the matching system for the full span of two random capacitors arbitrarily positioned for the *unloaded* coil. The position setting reflects an *unmatched* case. Ports 1-3 heavily reflect the power, which also occurs in the coupling coefficients. The system radiates only lightly, hence the power coupled to other elements remains at very low levels.

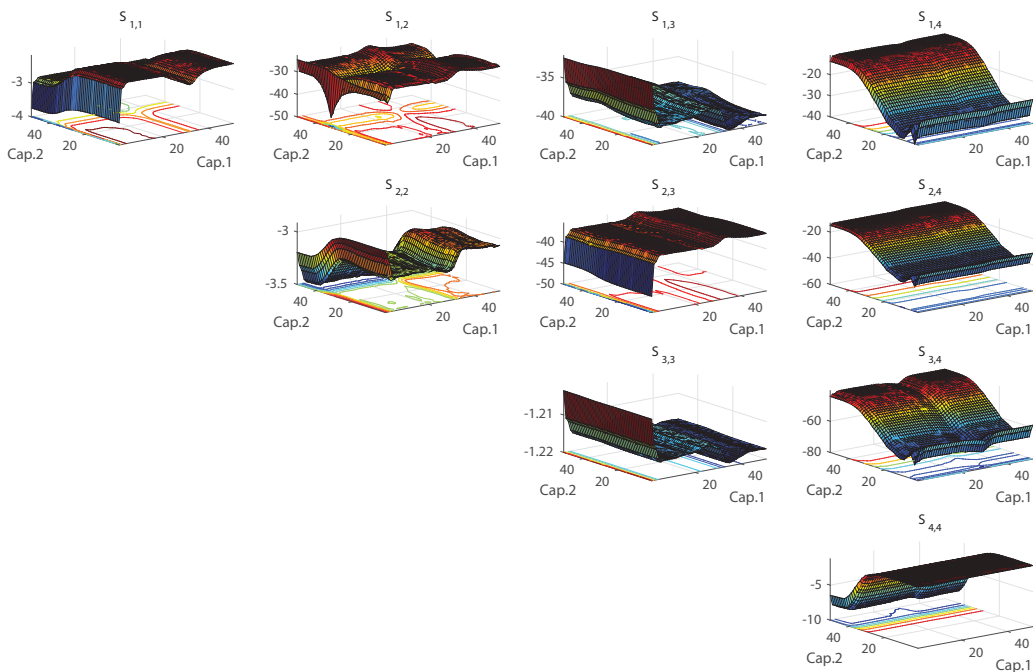


Figure 5.4: Roughness of the S-parameters at the input of the matching system for the full span of two random capacitors arbitrarily positioned for the *loaded* coil. The position setting reflects an *unmatched* case. Compared to the unloaded case in Figure 5.3, only two surface plots exhibit structural changes, namely port 1 and port 2. All others S-parameters suffer little or no structural changes, with only amplitude variations. Comparing the s_{11} of all four cases, it can be inferred that performing solely a gradient descent would yield different outcomes.

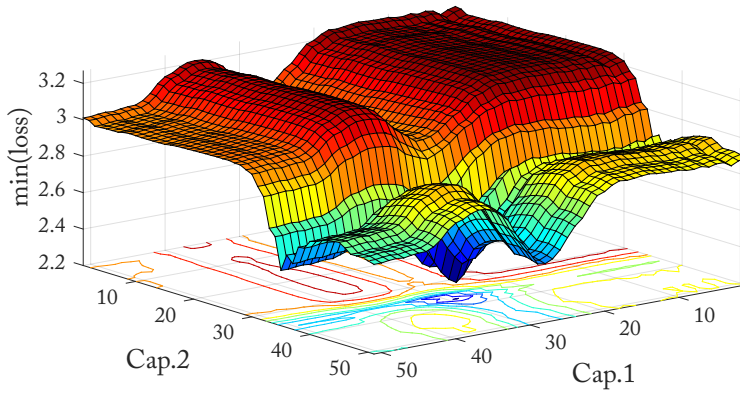
Comparing the matched (Figures 5.1-5.2) to the unmatched case (Figures 5.3-5.4), the matched case exhibits increased structural diversity, while power is flowing into the system. The matched case refers to a system condition where a solution is not far, in terms of the Euclidean distance of the position vector, and a matching strategy is easier to be found.

On the contrary, the unmatched case does not provide much insight concerning the way to proceed. The system can be brought close to matching only by changing to another set of capacitors. The iterative exhaustive sub-space search guarantees that the optimum will be found when the position vector is close to it. In a similar manner, the randomization of the initial position guarantees that a good candidate position is close to the optimum, disregarding choices like the unmatched case.

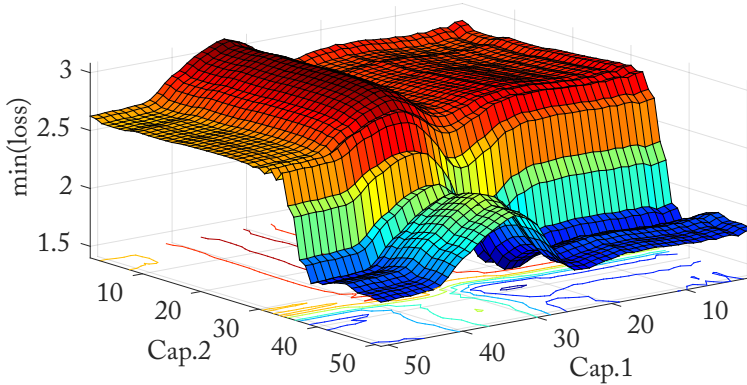
Minimum losses

Figure 5.5 depicts the surfaces of the values for the objective function of minimum losses when the system is initially matched. In this case, the objective function returns a scalar number, which is the difference of the traces of the 4×4 S-matrix of the total system and the 8×8 S-matrix of the matching network, as described in Chapter 4. The z -axis values correspond to the value of the trace and, therefore, are not in power units as previously.

The position where the system is matched in terms of its reflection coefficients is the same as previously and corresponds to the position vector $pos_{init.} = (34, 37)$. The minimum loss condition corresponds to the position vector $pos = (29, 37)$ and differs from the minimum reflection. The difference is owed to the different matching criterion. As a first observation, the matching condition for this objective function lies in the proximity of the minimum reflection optimization. Secondly, the matching condition is affected by only one capacitor.



(a)



(b)

Figure 5.5: Roughness of $\min(\text{loss})$ initially matched for the (a) unloaded and (b) loaded case.

Hence, it is concluded that only slight adjustments are necessary for finding the optimum for the current objective function.

Concerning the surfaces, the shape is preserved in the unloaded and loaded case. The robustness of the surfaces against the change of the

loading condition indicates that the objective function of minimum losses may serve as a more stable matching criterion compared to the minimum reflections. Moreover, both surfaces present one single minimum, which would render convergence of the iterative sub-space search faster, as will be shown later.

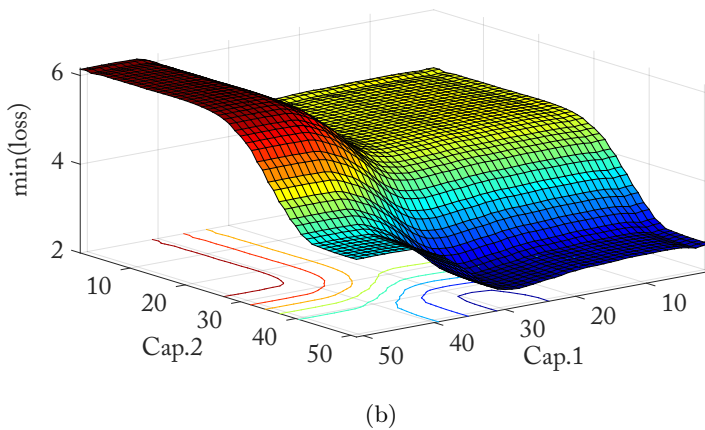
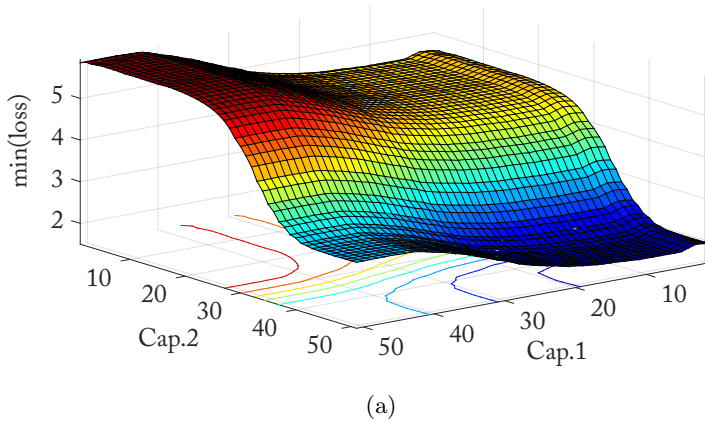


Figure 5.6: Roughness of $\min(\text{loss})$ for random position for the (a) unloaded and (b) loaded case.

Regarding the values returned by the objective function, the unloaded surface has a higher net value compared to the loaded case. For this, two mechanisms come into play. One concerns coupling as seen at the input of the system and the other the losses of the matching network. The observable net decrease of the values suggests that coupling has increased, which can be confirmed from Figures 5.1 and 5.2.

Figure 5.6 depicts the surfaces of the values for the objective function of minimum losses when the matching system is at a random position and, hence, the system is unmatched. The returned values of the objective function indicate that the system is far from the matched case and other capacitors need to be adjusted beforehand in order to end up to the minimum depicted in Figure 5.5(b). Nevertheless, the adjustment of the selected capacitors improves the matching, as seen by the large span of the values in the z -axis. This is an instance of the problem for an initial random seed that could end-up in a local minimum and, hence, a matched condition.

Maximum power to the load

Figures 5.7-5.8 depict the surfaces of the diagonal elements of the matrix $P^c = (X^H X) - (X^H (S^c)^H S^c X)$ presented in Equation 4.22. Figure 5.7 corresponds to the unloaded case and Figure 5.8 to the loaded case.

The surfaces are smooth with identifiable global maxima, with the exception of P_{22}^c for the loaded case, where a global minimum exists and at least four local maxima are present. The surfaces have several plateaus that could pose a problem to a gradient guided algorithm to find its direction towards the optimum. This restriction is waived by the execution of the sub-space search, which finds the local maximum in one iteration. The three of the four diagonal elements tend to preserve the shape characteristics between the unloaded and the

loaded case. Nevertheless, the shape of P_{22}^c degenerates after loading the coil. From the values of the z -axis it can be concluded that more power flows into the coil, owed mainly to port 1 and 2.

Figure 5.9 depicts the surfaces of the trace of matrix P^c , presented in Equation 4.23, for the (a) unloaded and (b) loaded case. The set of these surfaces clarifies the previously stated observations of the individual elements of the array. The net increase of the power flowing into the coil is shown by the value of the trace. This indicates that, in the unloaded case, power is reflected at the input of the coil back to the matching network, where it is dissipated.

Concerning the search of the maximum, the existence of a single maximum as seen in both surfaces of Figure 5.9 can be discovered with high probability by the exhaustive sub-space search in one iteration. The fast discovery makes this objective function comparable to the one minimizing the losses. This is derived from the fact that both take into account the losses owed to coupling and the losses in the matching network.

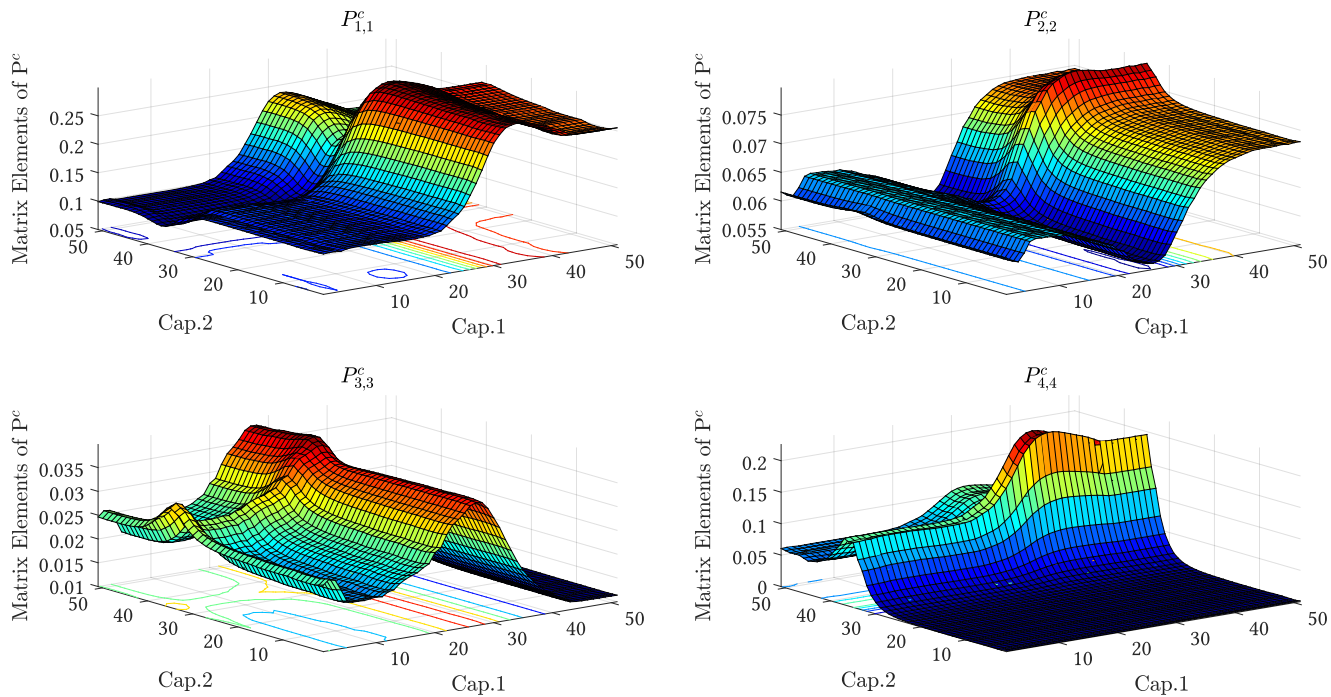


Figure 5.7: Roughness of the diagonal elements of the matrix $P^c = (X^H X) - (X^H (S^c)^H S^c X)$ (unloaded).

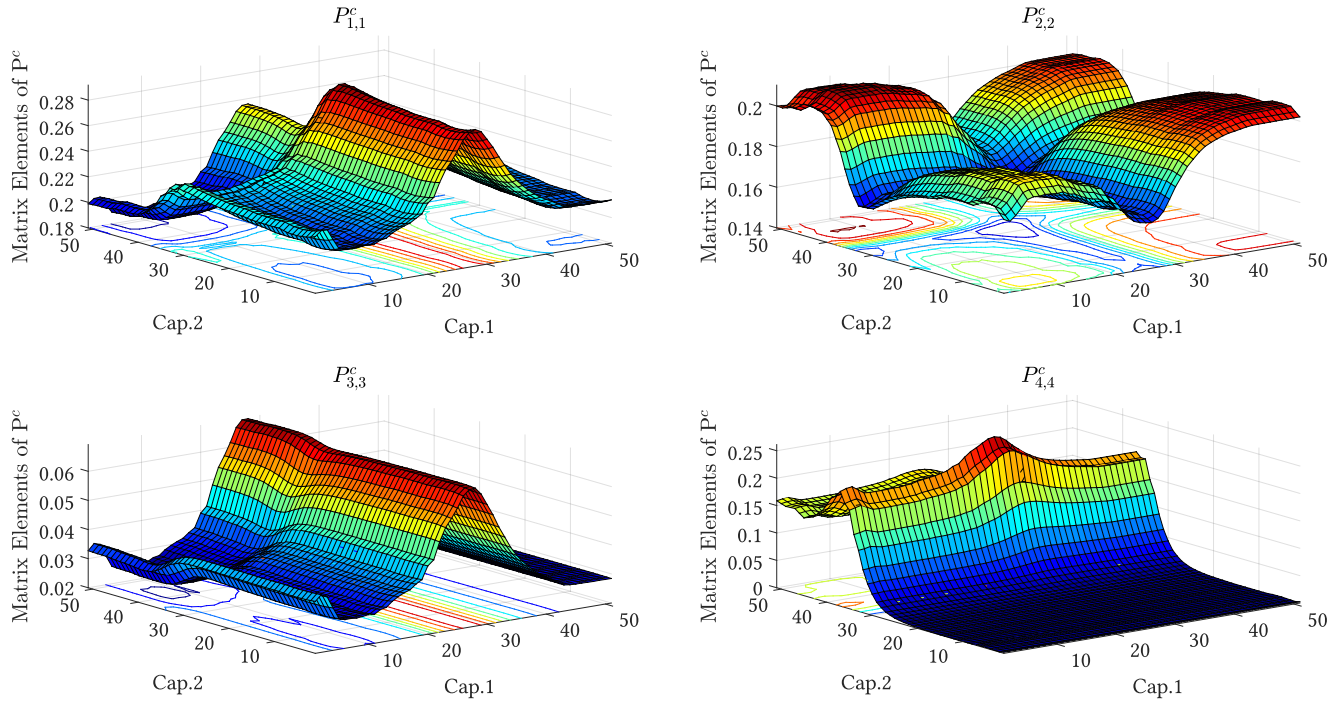
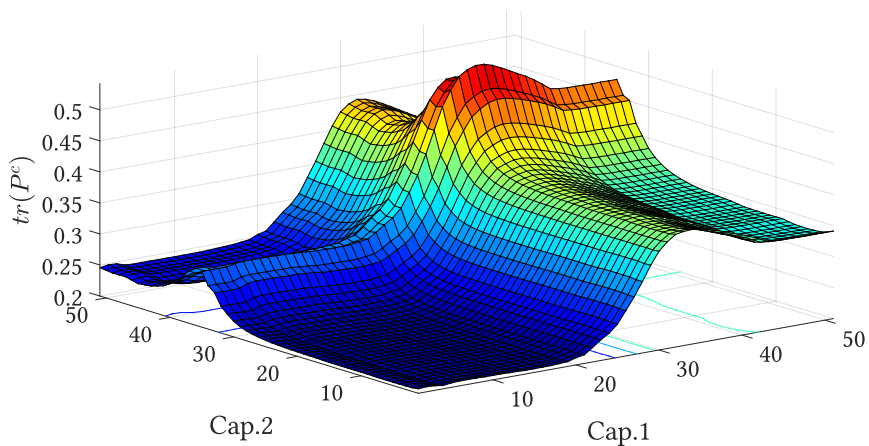
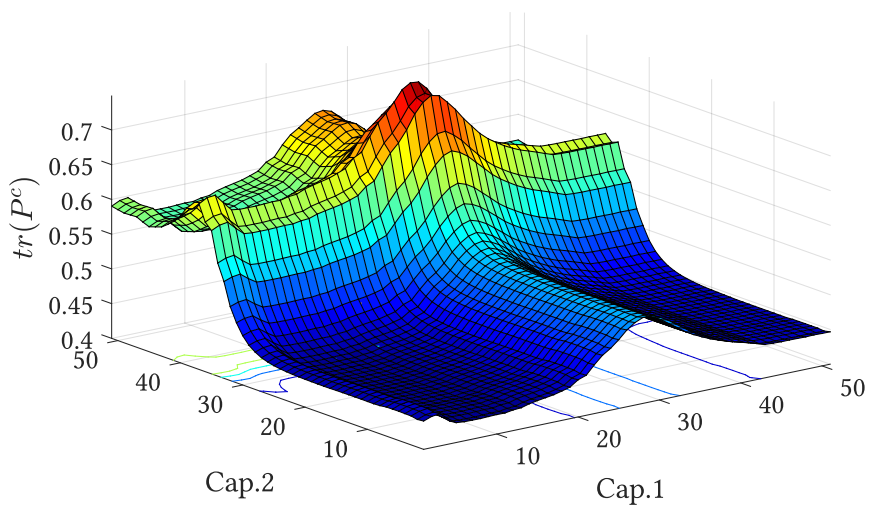


Figure 5.8: Roughness of the diagonal elements of the matrix $P^c = (X^H X) - (X^H (S^c)^H S^c X)$ (loaded).



(a)



(b)

Figure 5.9: Roughness of $\text{tr}(X^H X) - \text{tr}(X^H (S^c)^H S^c X)$ in the (a) unloaded and the (b) loaded case.

5.2.2 Monte Carlo simulation results

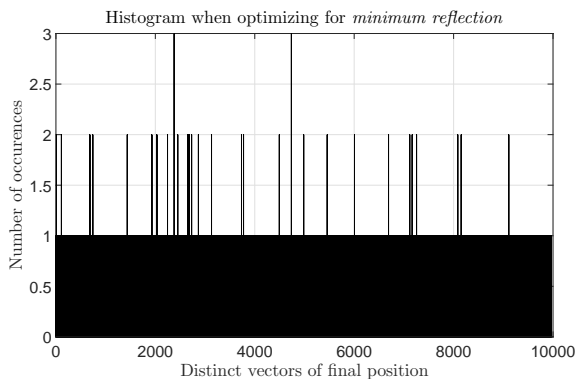
Distribution of objective functions optima

In Figures 5.10-5.12, the histograms of the 10'000 experiments for the three objective functions are presented. The upper histograms show the number of occurrences of the final positions. If a position is already encountered, the outcome is accounted for the corresponding bin. Hence, each bin of the histogram corresponds to a distinct final position. The lower histograms are sorted according to the value returned by the objective function.

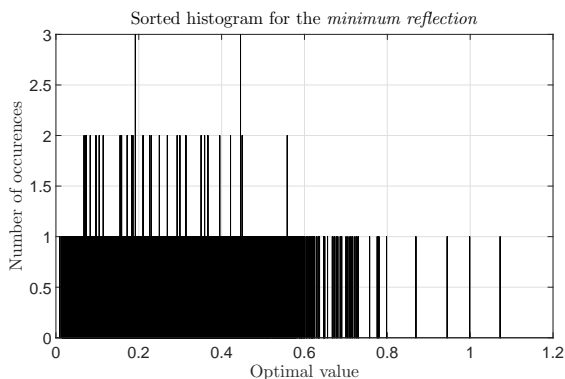
Ideally, it is desirable that the algorithm returns results that lie close to the best result of the population with high probability. When the histogram is multi-modal, it indicates that there are several local optima.

Minimum reflection. Histogram (a) of Figure 5.10 showing the number of occurrences of the final positions is uniform. Apart from few exceptions, the resulting positions are all different. Histogram (b) is the sorted version of histogram (a) according to the minimum of the objective function $trace(\tilde{S})$. The algorithm results in positions with small reflection, but in different positions. Both histograms indicate a lack of algorithm stability. The optimization does not guarantee the discovery of the global minimum. Instead, almost every random experiment ends up in a different result. Moreover, the existence of the many different optima signify that many local minima may be present. Another reason for this behavior is that the single optimum cannot be found, even when approached from different directions.

Minimum losses. Histogram (a) of Figure 5.11 showing the number of occurrences of the final positions is skewed right and multi-



(a)

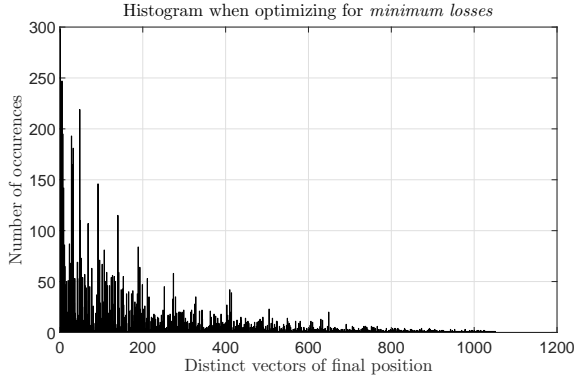


(b)

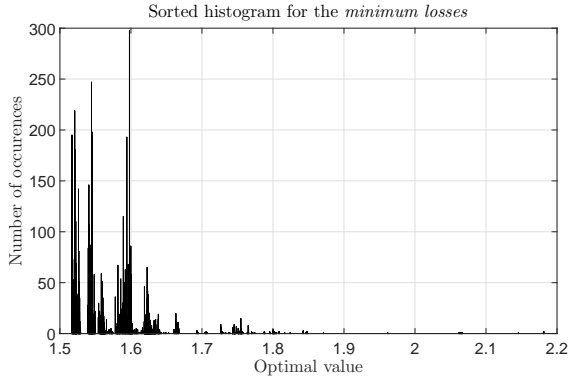
Figure 5.10: Histograms of the 10'000 repetitions for the *minimum reflection* objective function. The upper histogram shows the number of occurrences of the final positions. The lower is sorted according to the value returned by the objective function.

modal. The early discovery of a good result with a success of almost 3% signifies that the existence of the global minimum is quickly found. This hypothesis matches with the observations of the surfaces depicting the objective function of minimum loss. The number of occurrences is the second highest among the evaluated objective

functions and makes the minimization of losses a candidate for evaluation. Histogram (b) confirms the performance of the objective function, since it results in optimal values in the lowest spectrum with very high probability.



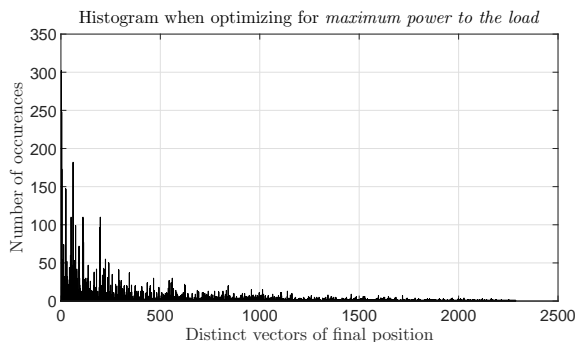
(a)



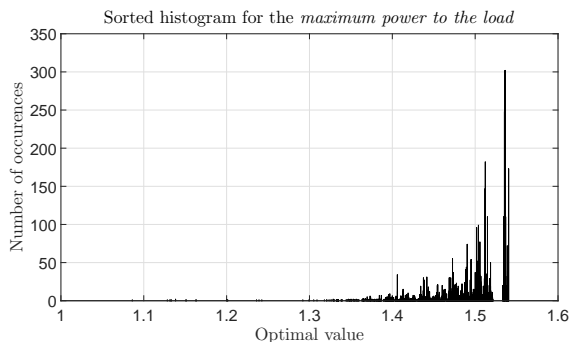
(b)

Figure 5.11: Histograms of the 10'000 repetitions when optimizing for *minimum losses* in the system. The upper histogram shows the number of occurrences of the final positions. The lower is sorted according to the value returned by the objective function.

Maximum power to the load. Histogram (a) of Figure 5.12 showing the number of occurrences of the final positions is skewed right and multi-modal. One of the earliest discoveries reappears several times, making the algorithm optimizing for maximum power to the load the best performing in this regard, with a frequency of more than 3%. Histogram (b) confirms this strategy for matching.



(a)



(b)

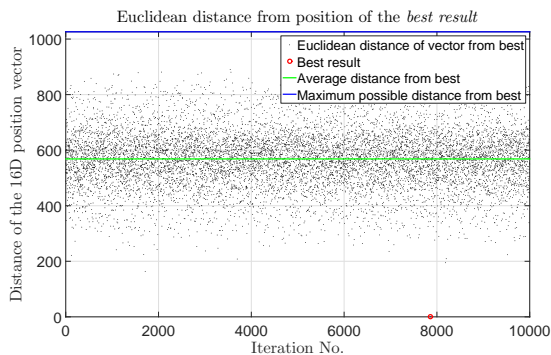
Figure 5.12: Histograms of the 10'000 repetitions when optimizing for *maximum power to the load*. The upper histogram shows the number of occurrences of the final positions. The lower is sorted according to the value returned by the objective function.

The presented findings support the observations made for the surfaces calculated by the scattering parameters and the corresponding conclusions. The two novel objective functions, combined with the proposed algorithm, give recurring results that are further investigated in the following.

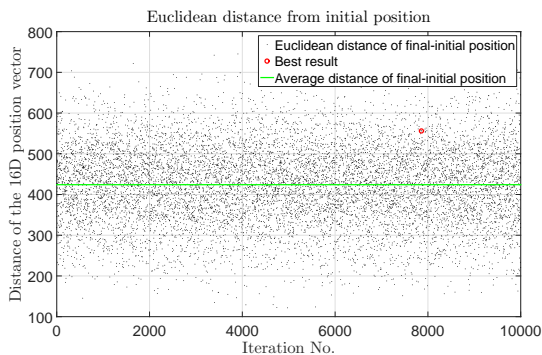
Position vector distance

Figures 5.13-5.15 depict the scatter plots of the Euclidean distances for the total seed population for the three objective functions. The upper plot displays the 16D Euclidean distance of each final position from the best solution in the seed population for each objective function. The mean value is plotted with the green line, whereas the blue line manifests the maximum Euclidean distance from the position of the best result. In the lower plot, the Euclidean distances between the initial and the final position for the seed population is drawn. The green line is the average of the population. Both plots denote the best result with a red circle.

Minimum reflection. Figure 5.13 corresponds to the minimum reflection optimization. The average of the possible outcomes lies at a distance of almost 600 from the best outcome. Taking into account the previously seen histograms for this case, which indicate the diversity of final outcomes, it can be concluded that there is higher likelihood that more local minima exist. These are well apart from each other and offer similarly good solutions in terms of minimization of reflections at the input of the system. The average distance of the cloud from the initial positions is 425 and is the lowest among the three explored objective functions. Hence, the objective function converges relatively fast to a local minimum in terms of traveling distance. Whether this translates into a good matching result is to be investigated later.



(a)

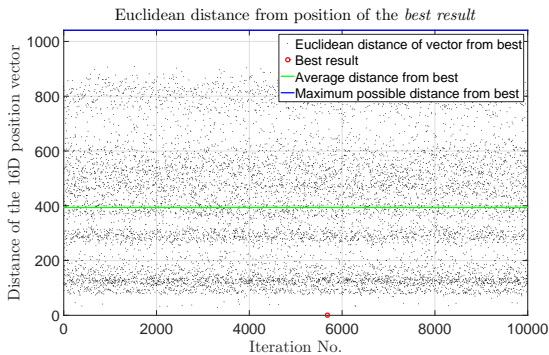


(b)

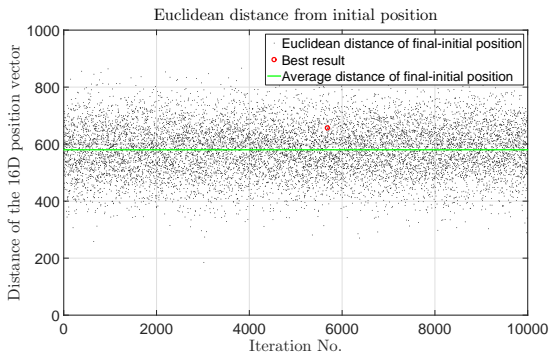
Figure 5.13: Scatter plot of the Euclidean distance for the objective function of *minimum reflection* at the input of the matching network.

Minimum losses. Figure 5.14 corresponds to the minimum losses optimization. In this case, the average of the possible outcomes lies at a distance of 400 from the best outcome. Nevertheless, the separation of the outcomes in several bands reveals the multiple modes observed in the respective histograms. The existence of multiple modes and bands is an indication of multiple optimal solutions. The band lying at the distance of 100-150 is a strong indication that a global optimum is present and that the algorithm approaches very

close to it, even if it cannot find it. The average distance of the cloud from the initial positions of 580 is the largest among the three objective functions. Moreover, the small dispersion of the final points around the average value is another strong indication of few minima, as supported by the corresponding histogram.



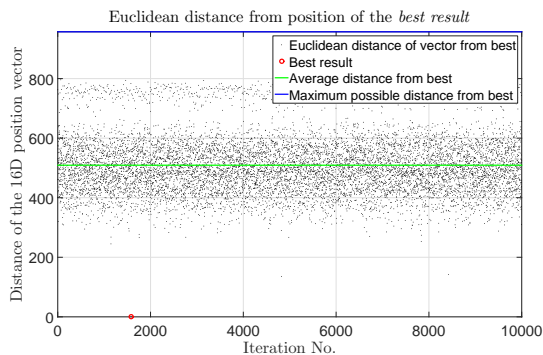
(a)



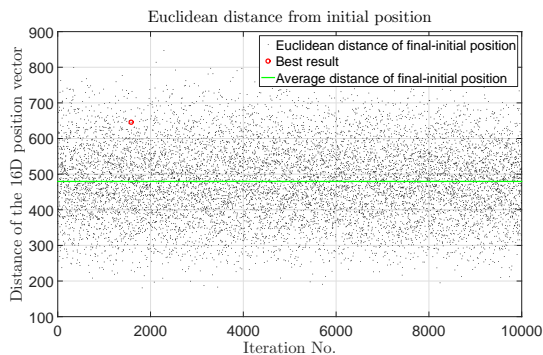
(b)

Figure 5.14: Scatter plot of the Euclidean distance for the objective function of *minimum losses* in the matching network.

Maximum power to the load. Figure 5.15 corresponds to the optimization of maximum power to the load. The average of the



(a)



(b)

Figure 5.15: Scatter plot of the Euclidean distance for the objective function of *maximum power to the load*.

possible outcomes is at a distance of 500 from the best outcome. Here, a second band appears at an even greater distance than the average, signifying that multiple optimal solutions are present. Taking into account the histogram of the sorted optima in Figure 5.12(b), the band lying at the distance of 750 is the one that corresponds to one of the best outcomes. The consistency of finding a sub-optimal solution implies that the 16D space has a dichotomy that the algorithm is unable to overcome. The average distance of the cloud from the

initial positions in this case is 480. The dispersion is much higher as compared to the optimization of minimum loss, which indicates the presence of several local maxima.

Individual capacitor ranges

Figure 5.16 is the box plot of the variation of the individual capacitors distance for the random input of 10'000 position vectors. The respective values are summarized in Table A.1 of the Appendix. The capacitors move the least for the objective function of minimum reflection and the most for the minimum losses. These results confirm the previously presented plots of the distances from the initial position.

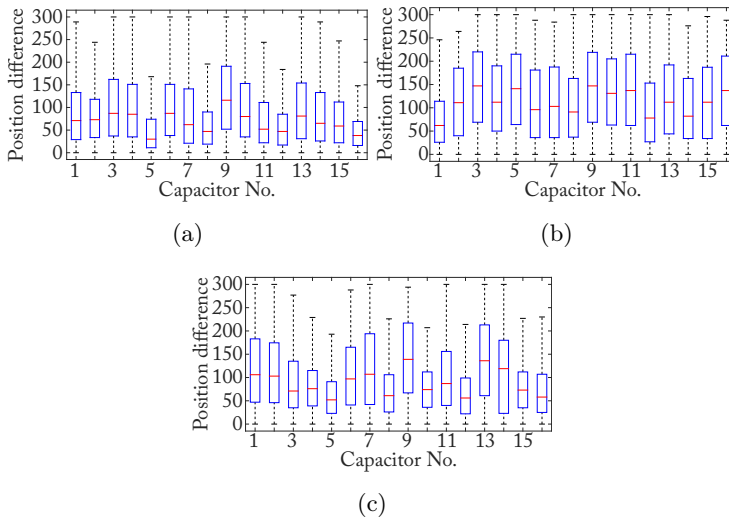


Figure 5.16: Position difference between the initial and final position for every capacitor for the 10'000 iterations for the different objective functions. (a) Minimum reflection at the input of the matching system, (b) minimum losses in the matching network and (c) maximum power transfer to the load.

Termination of iteration

As described in Chapter 4, the sub-space exhaustive search is terminated at a local optimum, when the position vector remains unchanged in two consecutive iterations. The histogram of the number of iterations until termination is shown in Figure 5.17 and summarized in Table 5.1. The iterative sub-space search terminates faster on average for the objective function of minimum losses due to the existence of few local optima.

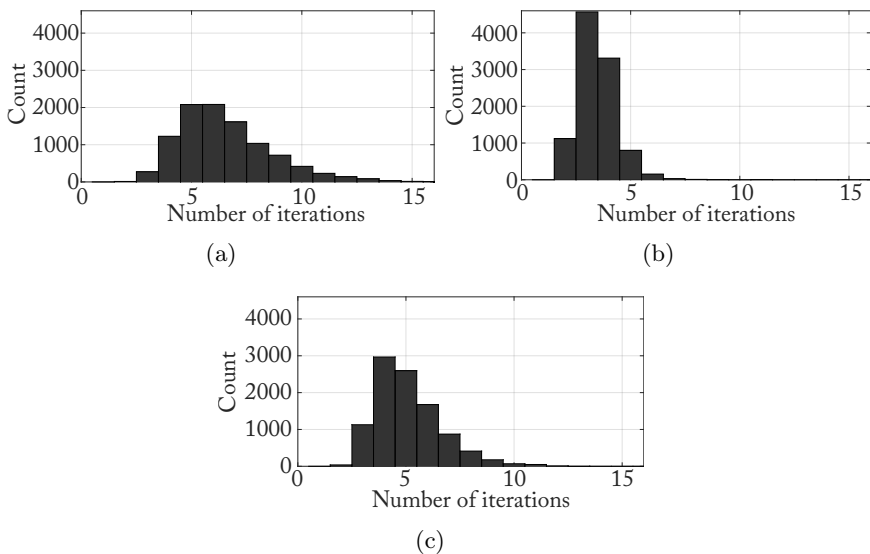


Figure 5.17: Histograms of the termination step of the sub-space exhaustive search for the different objective functions. (a) Minimum reflection at the input of the matching system, (b) minimum losses in the system and (c) maximum power transfer to the load.

Concerning the large number of iterations for the objective function of minimum reflection, the speed of convergence contradicts the small traveling distance to the optimum. This behavior suggests that the approach is either slow or oscillation of movement occurs in

the vicinity of the optimum.

Finally, the broader distribution of the termination step for the objective function of maximum power and its long tail suggest that the algorithm encounters difficulties in finding the optimum. The separation of the 16D space, as discussed for Figures 5.12 and 5.15(a), can trigger this behavior, when the random seeds are close to the multidimensional separation plane.

	Mean	Median	SD
$\min(\tilde{S})$	6.5474	6	2.2011
$\min(\text{loss})$	3.4440	3	0.8877
$\max(\text{P2L})$	5.0768	5	1.5385

Table 5.1: Statistical analysis of the termination step.

Chapter 6

Multiple channel matching experiments

In the present chapter, the results of the experiments conducted with the designed adaptive matching system in the bore of a 7 Tesla MRI system (Achieva, Philips, Netherlands) are presented. The matching system consists of the two layers of the developed variable matching network and a 4×4 Butler matrix and is driven by four independent 1 kW amplifiers, as described in Chapter 4. The system is controlled by a computer undertaking the task of evaluating different optimization criteria for matching the generic 4-port array under different loading conditions.

The multiple channel experiments presented in this chapter are conducted with the following routine, given the measurement setup is installed:

1. turn off all unnecessary preparation phase corrections at the scanner side,
2. connect the network analyzer at the input of the matching network,
3. position the center xy -plane of the coil at the isocenter of the magnet,

4. manually match the unloaded coil until a satisfactory matching condition is achieved by taking into account only the reflection coefficients of the 4-channel system,
5. read all the data and save the initial position and relevant S-matrices,
6. load the coil with the phantom avoiding any motion of the coil,
7. read the new S-matrix of the loaded system,
8. disconnect the network analyzer and connect the output of the high-power amplifiers,
9. acquire the B_1^+ maps and MR images for the unmatched state,
10. disconnect the amplifiers and re-connect the network analyzer,
11. perform automatic matching for a given objective function,
12. record the S-matrices with the network analyzer,
13. disconnect the network analyzer and re-connect the scanner,
14. acquire the B_1^+ maps and MR images for the matched state,
15. repeat for all objective functions from step 10.

For comparison purposes, an additional experiment, which requires moving the scanner table in order to gain access to the matching network, was conducted by removing the Butler matrix and one of the matching network layers. This constitutes the conventional method of matching and serves comparison purposes of the two. In the single layer matching, as will be called from now on, the chosen objective function was the minimization of the reflection coefficient at the input of the system. Consequently, the aforementioned routine was repeated for the single layer matching setup.

In step 6, motion can be caused accidentally either by phantom loading or indirectly when connecting/disconnecting cables. Any motion in the maps and images is registered by means of the standard Matlab image toolbox.

The B_1^+ and SNR maps were acquired in a similar fashion to the single channel experiment. Both map-flavors indicate strong non-uniformity attributed to the coupling changes by re-matching. Hence, the ultimate comparison is imperative to be made in a statistical manner. Thus, the following figures are automatically computed on the acquired image: (i) mean, (ii) median and (iii) standard deviation.

For the images presented henceforth, whether B_1^+ maps or SNR maps, the region outside the phantom area is automatically masked out and has no contribution to the statistical results.

6.1 Results

In the following, the experimental results of the array matching are presented. Firstly, the single layer minimum reflection per-port matching of the 4-channel coil array is demonstrated. Following, the novel matching methods considering array coupling are shown for all aforementioned objective functions. Lastly, the comparison between the two preceding matching methods is presented.

Individual port matching of MRI array

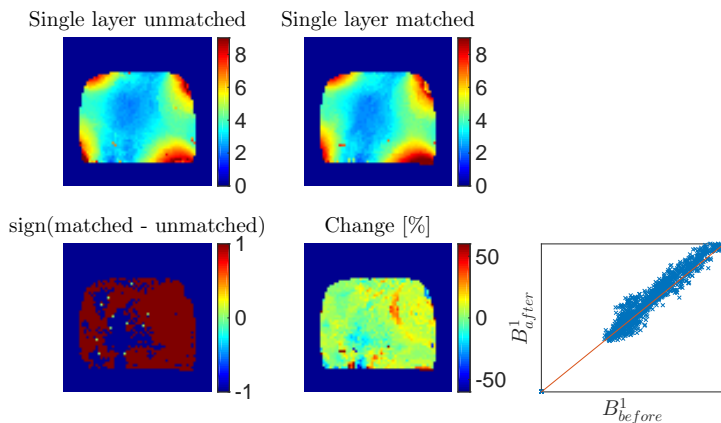
Figure 6.1 depicts the (a) B_1^+ and (b) SNR maps of the single layer matching setup for the unmatched and the matched case in the top row. The sign of the difference between the matched and the unmatched case are displayed below the respective maps, along with the percentage change on per-pixel basis. The improvement is shown

in the last plot, where the B_1^+ and SNR values of the unmatched (x -axis) and matched case (y -axis) for each pixel of the map are compared. The red line represents the zero improvement margin. The expected improvement is demonstrated by the sign map and the scatter plot, where the majority of pixels show gains in B_1^+ and SNR units. The mean spatial improvement for the B_1^+ maps is 7.95 % with a standard deviation of 12.57 %, while for the SNR maps 17.14 % and 21.05 % respectively. Table 6.1 summarizes the statistical analysis' results of the spatial improvement in the sample. The sign of improvement between the two matching conditions highlights the areas inside the sample affected by matching. The pixels in deeper areas of the sample exhibit loss, while the improvement is mainly attributed to the regions adjacent to the coils.

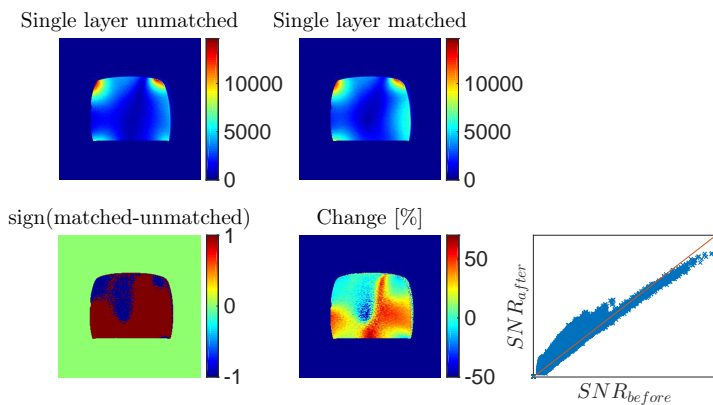
	Mean change [%]	Median change [%]	SD of change [%]
B_1^+	7.95	5.94	12.57
SNR	17.14	17.73	21.05

Table 6.1: Percentage change of the B_1^+ and the SNR from the unmatched to the matched case.

In Figures 6.2-6.5, the individual channel contributions in terms of both B_1^+ and SNR maps are presented, accompanied by the percentage change and corresponding distributions. The S_{ii} traces at the input of the matching network show the change in matching as seen by the network analyzer. Considerable improvement can be observed after re-matching the loaded coil in terms of reflection coefficients. All channels contribute consistently in their proximity, but with low improvement, as shown in the percentage change plots. The significant improvement occurs in the areas with lack of signal for the unmatched condition. They lie at the opposite side of the transmit-



(a)



(b)

Figure 6.1: Total (a) B_1^+ and (b) SNR maps of single layer minimum reflection per-port matching. Matched and unmatched cases, along with the sign of difference and percentage change.

ting coils and in the center of the sample. Focusing on channel 1 and 3, there is no visible improvement for the individual channels, as seen in the histograms, despite the improvement displayed by the

traces. This suggests that power does not reach the sample. There are two mechanisms leading to this phenomenon. Firstly, in the lack of consideration for coupling, power is scattered back through the coupled coil elements and, secondly, part of the power is dissipated in the matching network. Finally, the spatial pattern of the change differs between the B_1^+ and SNR maps.

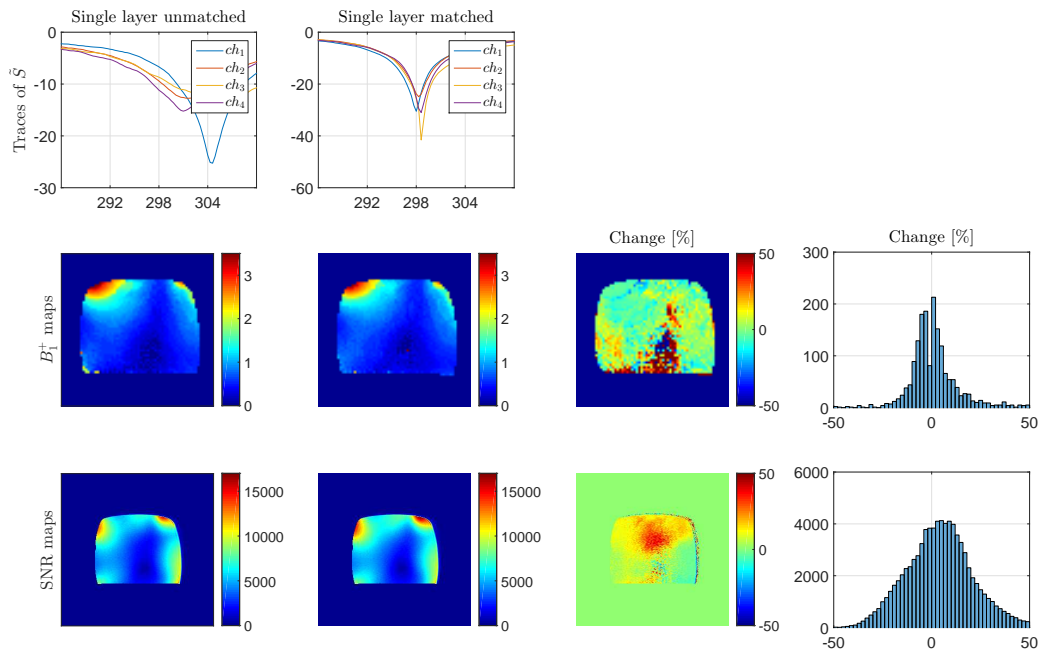


Figure 6.2: Individual channel effect on array matching for the single layer setup (channel 1).

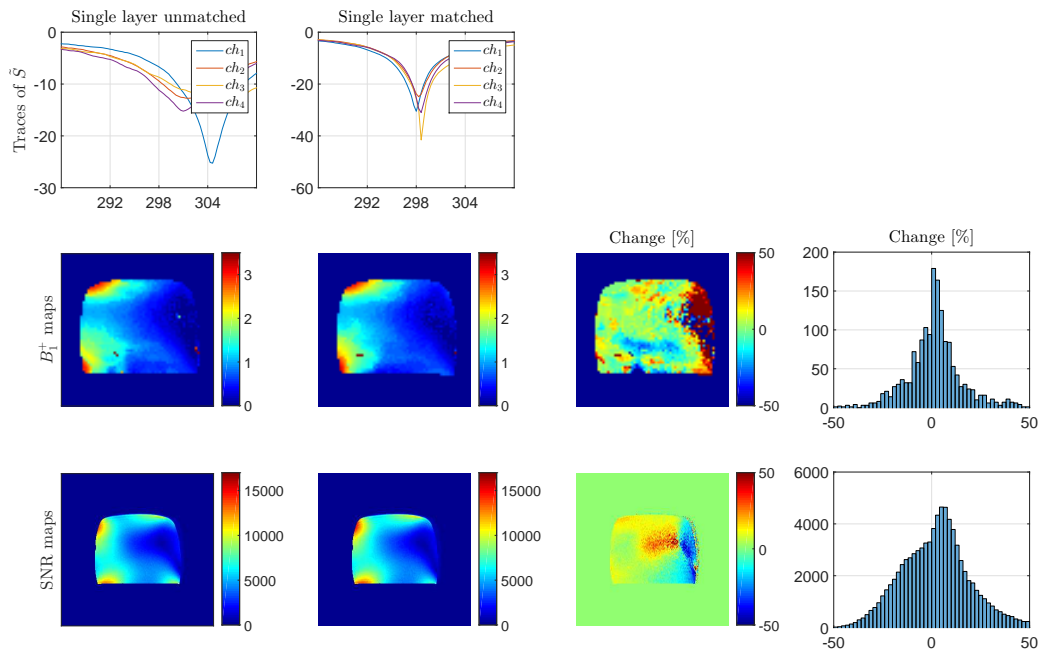


Figure 6.3: Individual channel effect on array matching for the single layer setup (channel 2).

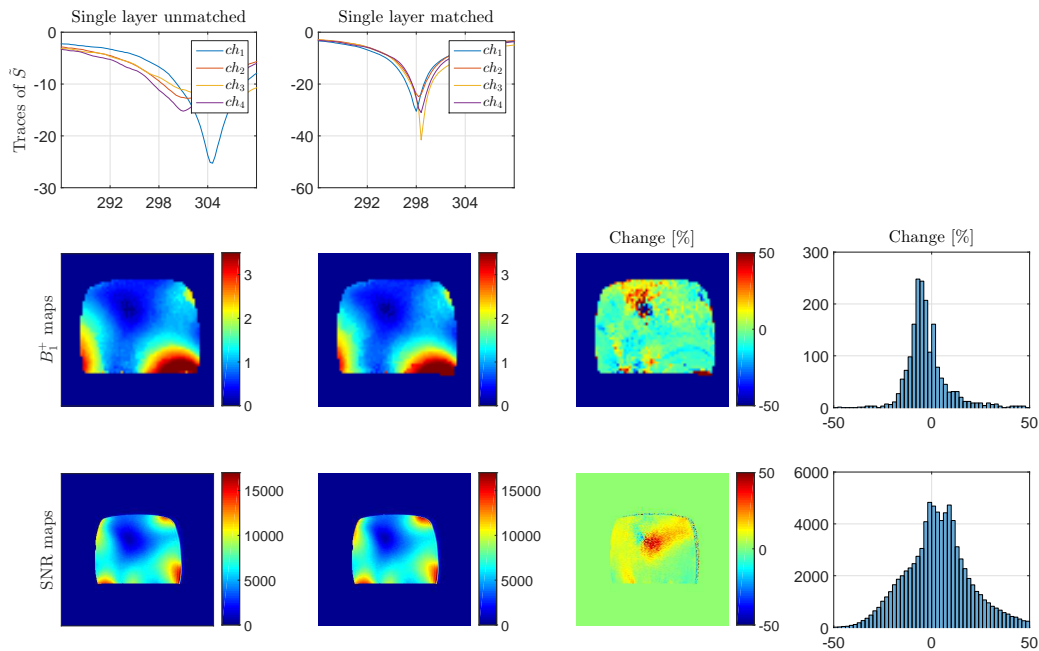


Figure 6.4: Individual channel effect on array matching for the single layer setup (channel 3).

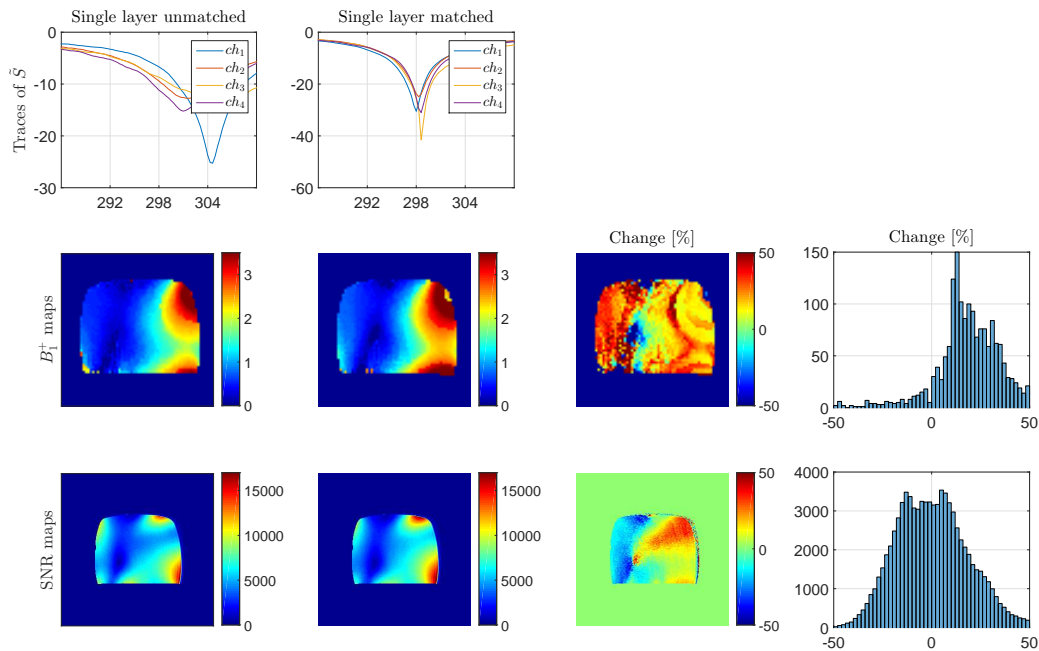
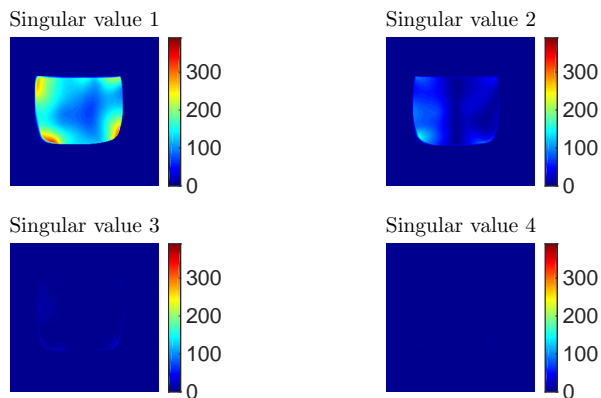
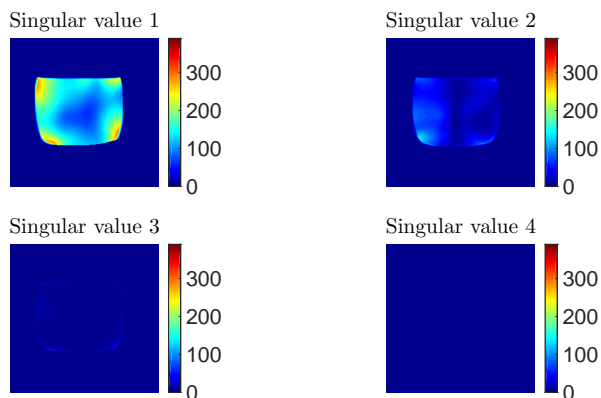


Figure 6.5: Individual channel effect on array matching for the single layer setup (channel 4).



(a)



(b)

Figure 6.6: SVD of SNR maps for the single layer matching in the (a) unmatched and the (b) matched case.

Figure 6.6 displays the four singular values calculated from the SNR maps. The second largest singular value has non-negligible values that amount to approximately 30 % of the maximum singular value. The signal emerging in the second singular value is missing from the

first one and is discarded to the second component. This can result from hardware fluctuations that affect the receive sensitivity, such as voltage gain. Nevertheless, in the lack of such fluctuations, more signal would end-up being accounted in the principal component and, therefore, deliver better matching results.

Multi-port matching of MRI array

In the following, the multi-port matching results are presented. The matching system is now considered as a whole by taking into account the cross-terms of the S-matrices as well.

Figure 6.7 shows the B_1^+ maps for all matching conditions in the first row and the pairwise comparisons in the remaining rows. The improvements of $\min(\tilde{S})$, $\min(\text{loss})$ and $\max(\text{P2L})$ compared to the loaded case are shown in the second row. The improvements of $\min(\text{loss})$ and $\max(\text{P2L})$ compared to the $\min(\tilde{S})$ are shown in the third row. The B_1^+ map that outmatches all is the one that optimizes for *minimum losses in the matching system*. The maps are significantly improved in all methods as compared to the loaded coil, which is considered to be the unmatched condition. In the unmatched case, the coil array cannot penetrate deep in the sample. Although the areas close to the conductors of the coils are generally well illuminated in all matched cases, there are areas which lie on the surface of the sample that suffer from low B_1^+ exposure. These areas are located at the top and bottom of the sample. Most of the central areas of the sample are covered after re-matching for all matching strategies.

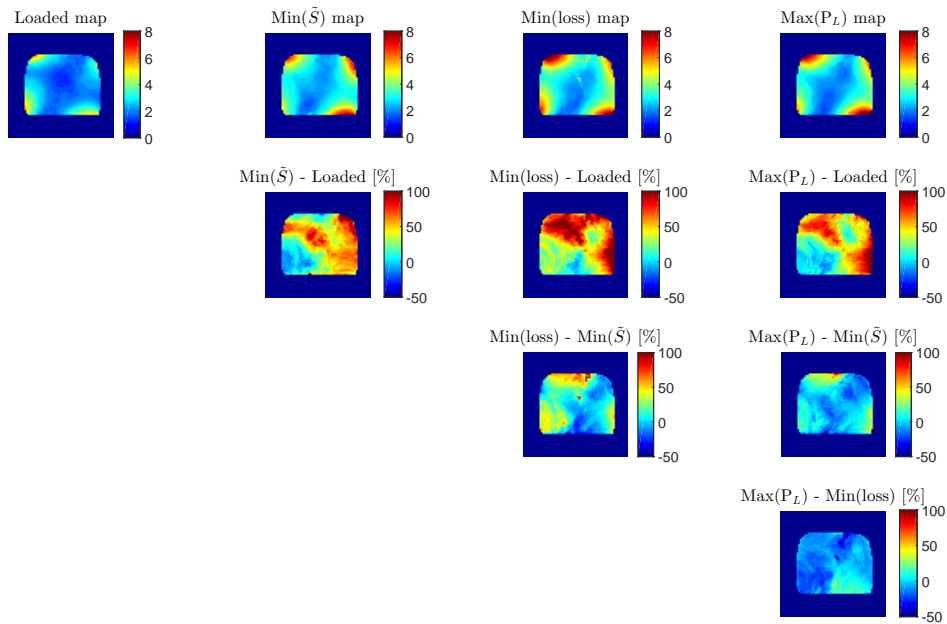


Figure 6.7: Comparisons of the total maps for array matching. The top row displays the actual maps, whereas the others constitute the B_1^+ map comparisons in percentage. The pairwise comparisons are noted accordingly.

The improvements of the pairwise comparisons of the B_1^+ maps on per-pixel basis are shown in the scatter plots in Figure 6.8. All

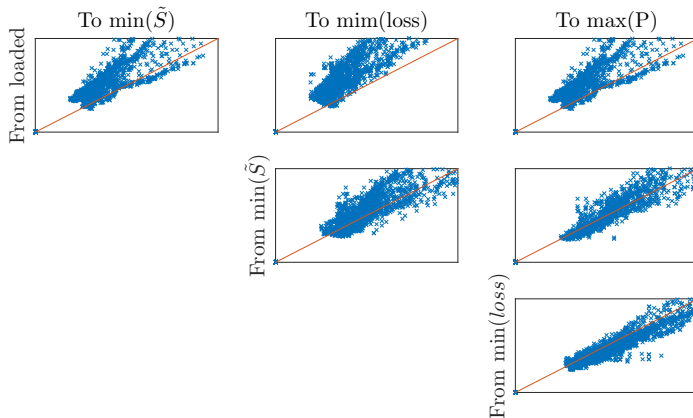


Figure 6.8: Pairwise comparison of the total B_1^+ maps for array matching.

plots demonstrate the improvement as compared to their inferior matching state, except from the comparison between the objective functions of minimum losses in the network and maximum power to the load. The latter was expected to have higher gains than the minimum losses optimization, since it accounts for maximum power transmission both at the input of the matching network and the input of the coil concurrently. From the density of the scatter plots it is evident that the improvement is more pronounced in the pixels with low B_1^+ than those with high B_1^+ . Table 6.2 summarizes the preceding observations by means of spatial statistics of the sample area.

		$min(\tilde{S})$	min(loss)	max(P2L)
Loaded	Mean [%]	38.67	56.47	40.35
	Median [%]	37.02	53.14	42.07
	SD [%]	31.60	42.46	38.07
$min(\tilde{S})$	Mean [%]		13.78	1.50
	Median [%]		11.50	0.78
	SD [%]		22.75	15.41
min(loss)	Mean [%]			-9.44
	Median [%]			-9.46
	SD [%]			12.10

Table 6.2: Statistical analysis of the percentage change of the B_1^+ in array matching.

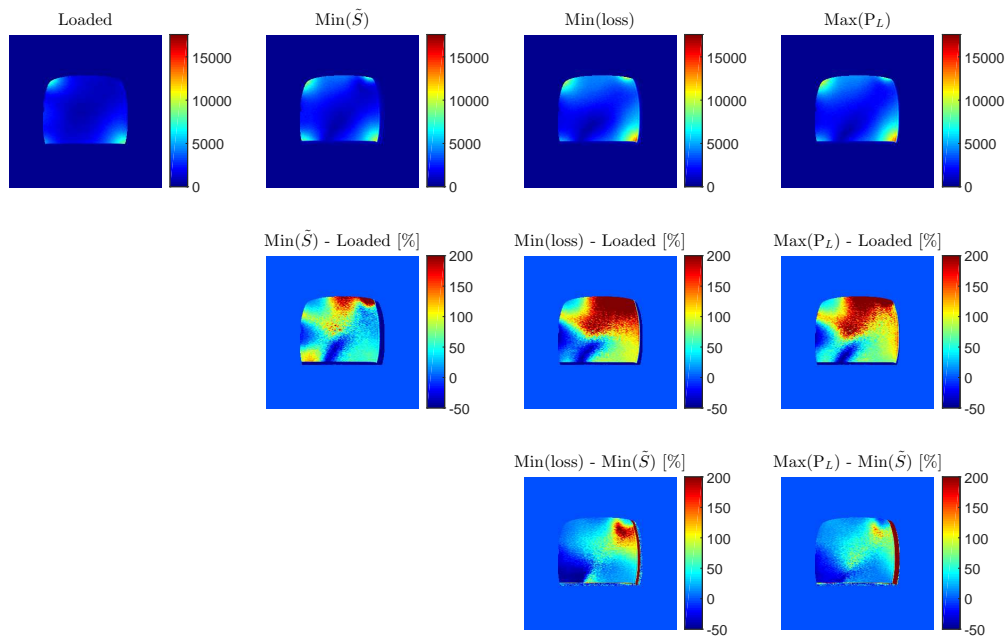


Figure 6.9: Comparisons of SNR maps of the array matching.

		$\min(\tilde{S})$	$\min(\text{loss})$	$\max(\text{P2L})$
Loaded	Mean [%]	65.80	110.90	105.10
	Median [%]	47.40	80.39	79.50
	SD [%]	88.70	145.30	121.80
$\min(\tilde{S})$	Mean [%]		32.70	30.29
	Median [%]		26.00	25.56
	SD [%]		56.20	53.99
$\min(\text{loss})$	Mean [%]			4.10
	Median [%]			0.54
	SD [%]			25.53

Table 6.3: Statistical analysis of the percentage change of the SNR in array matching.

Figure 6.9 depicts the pairwise comparisons of the SNR maps. Matching gains are substantial when compared with the loaded case. The pairwise comparisons preserve the sign of difference of the B_1^+ comparisons. Also in this case, the objective function for $\min(\text{loss})$ outperforms the one for $\max(\text{P2L})$, as observed in the B_1^+ map comparison. The improvement is small, but the range of confidence owed to the large value of standard deviation does not allow a safe conclusion. As the mean value of the change for all pixels is small, it is assumed that error is also generated by the algorithm performing the image registration. Table 6.3 summarizes the preceding observations by means of spatial statistics of the sample area.

Figure 6.10 displays the coupling coefficients in logarithmic and linear scale for the different objective functions. All plots are identically scaled. The lower triangle scattering parameters of the matching system S-matrix are omitted due to symmetry of the S-matrices. Counter-intuitively, the coupling at the input of the system increases for the case of *minimum loss*, which is the best matching scenario

so far. Considering that $\min(\text{loss})$ optimization outperforms the one for $\min(\tilde{S})$ in terms of B_1^+ strength according to Tables 6.2-6.3, coupling at the input of the matching network is an important factor to account for array matching performance. The optimization for $\min(\tilde{S})$ injects power to the array system measuring the contributions of every channel individually, ignoring the effect of coupling, as depicted in the second column of the figure. Accounting for these effects solely at the input of the system also limits the capabilities of the matching system, since it ignores its internal losses. Based on the B_1^+ and SNR map results, a matching strategy that accounts for all coupling coefficients in the system, like the $\min(\text{loss})$ and the $\max(\text{P2L})$ optimizations do, is beneficial for array matching.

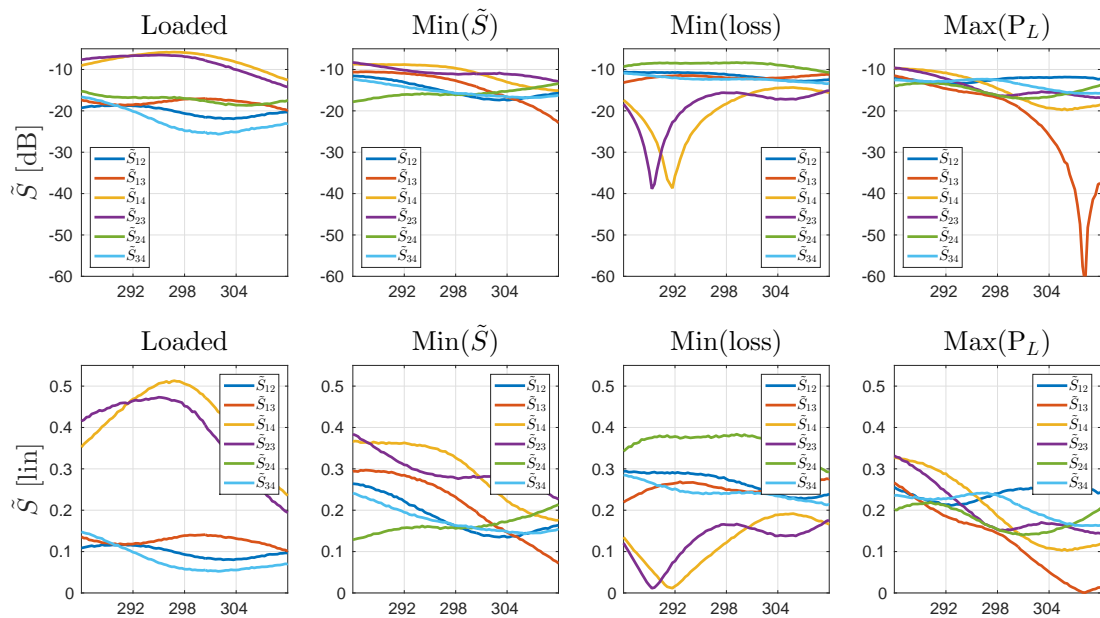


Figure 6.10: Coupling coefficients after matching with different objective functions at the input of the matching system.

Figures 6.11-6.14 depict the single channel contributions in terms of both B_1^+ mapping and SNR maps. Along with the B_1^+ and SNR maps, the reflections coefficients at the input of the matching network are depicted. Columns refer to the different objective functions. The improvements are reflected in the maps for all individual channels and all novel methods. Also in this case, the *minimum losses* optimization is the best performing one on average. Counter-intuitively for the min(loss), reflection at the input of the matching network is increased for all channels. The same occurs for the second best, namely the function that optimizes for *maximum power to the load*. Considering the net improvement of both min(loss) and max(P2L) to min(\tilde{S}) in the B_1^+ and SNR maps, along with the significant increase of all reflection coefficients, it is implied that optimizing solely for the S-matrix of the total system does not deliver the optimum result. Instead, taking into account the interaction of the individual S-matrices that are cascaded and form the system is beneficial in terms of B_1^+ delivered to the sample.

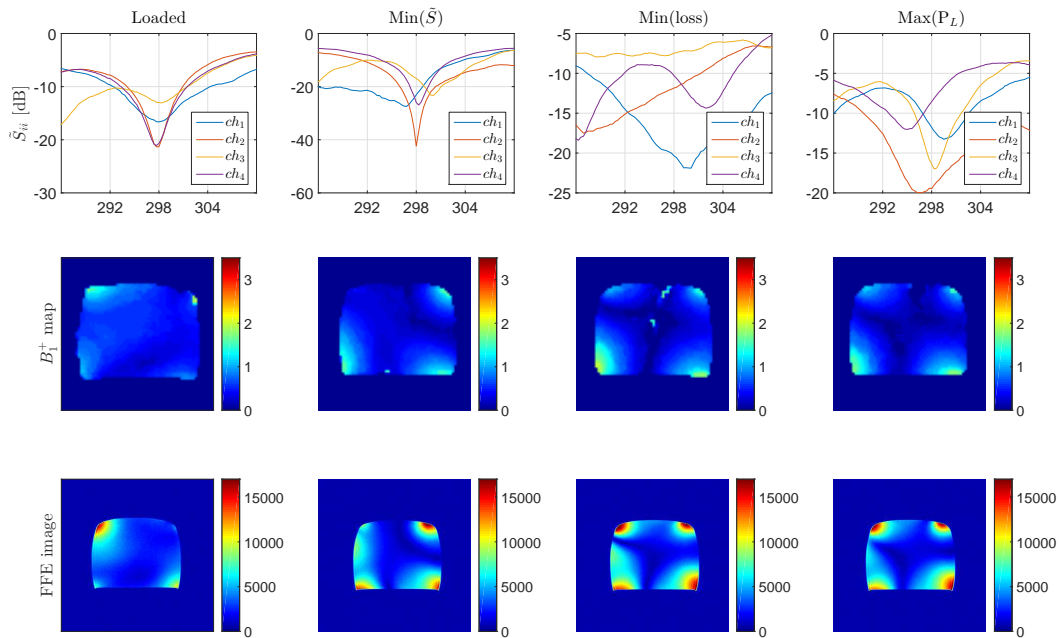


Figure 6.11: Individual channel effect on array matching (channel 1).

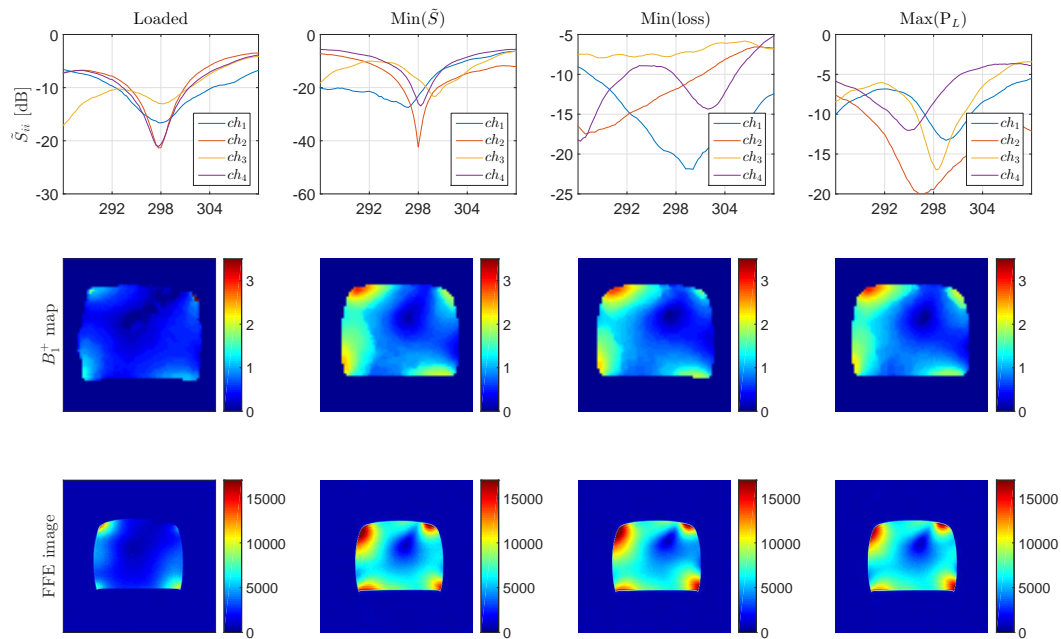


Figure 6.12: Individual channel effect on array matching (channel 2).

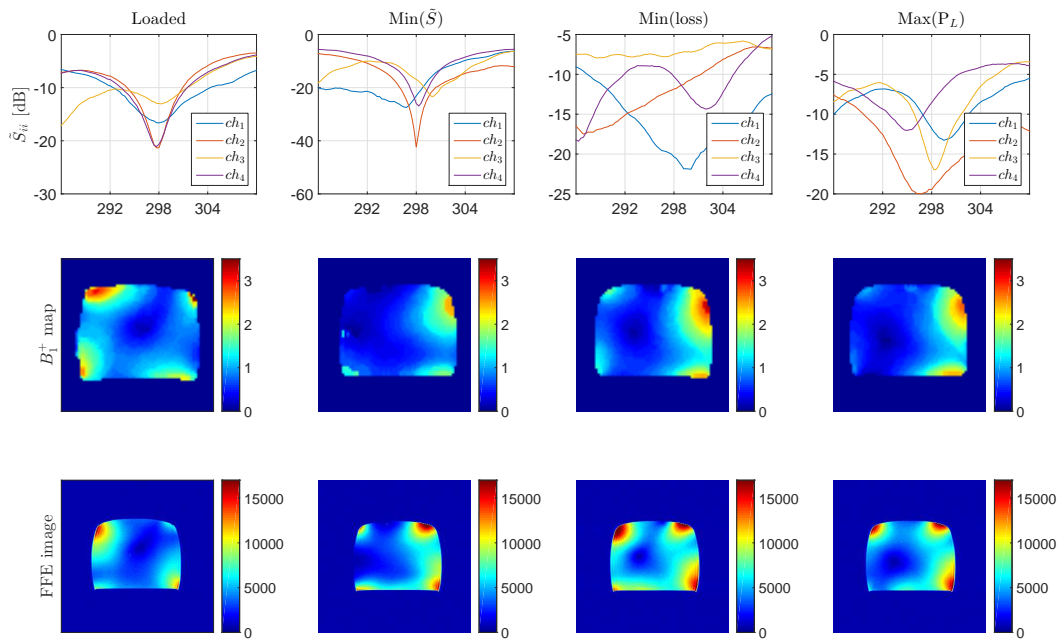


Figure 6.13: Individual channel effect on array matching (channel 3).

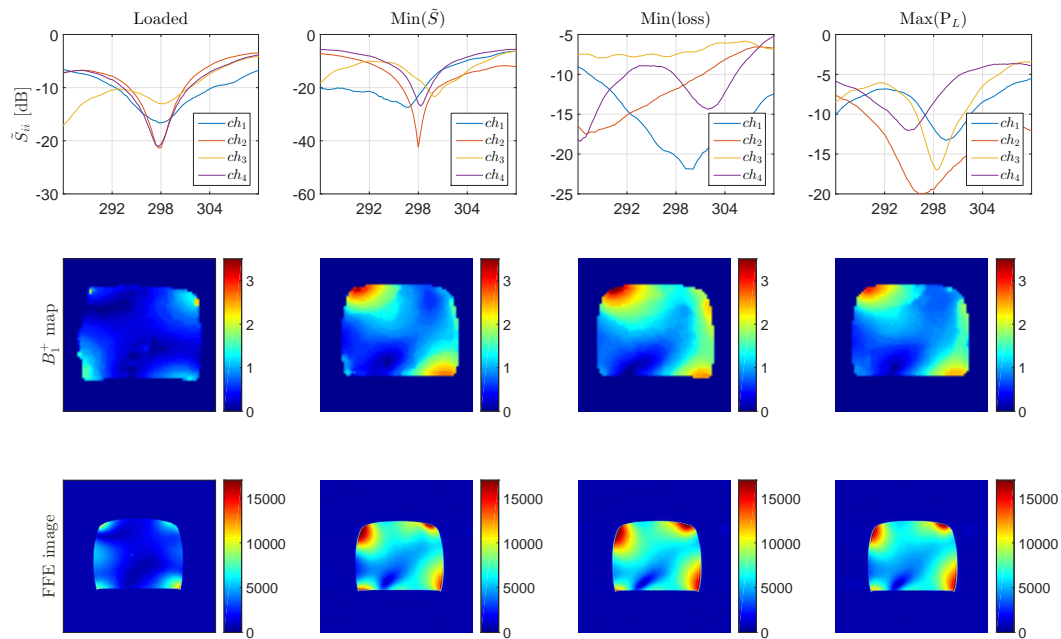
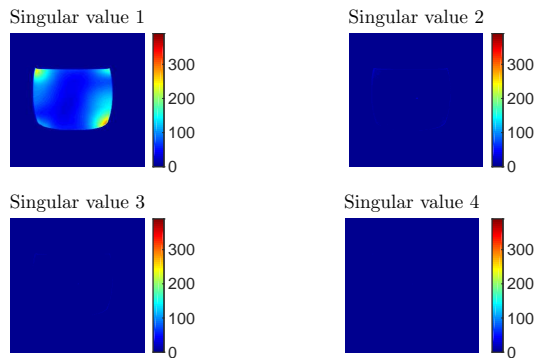
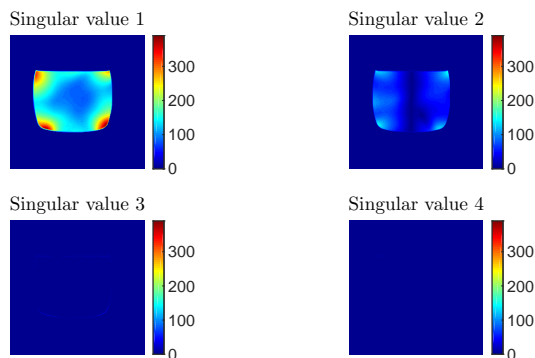


Figure 6.14: Individual channel effect on array matching (channel 4).

Figures 6.15-6.16 display the four singular values calculated by the SNR maps. Again, the second largest singular value has non-negligible values, with the exception of the loaded coil. As previously discussed, the pronounced levels of the second singular value are owed to receive instability and, in their absence, a better matching performance would have been achieved.

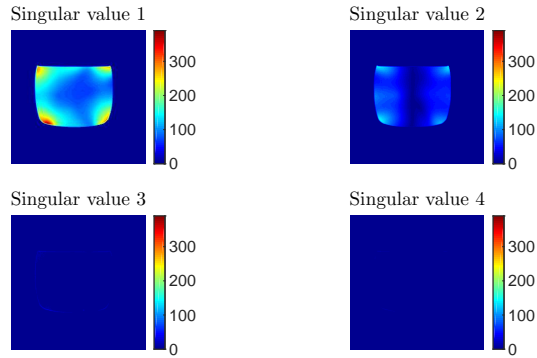


(a)

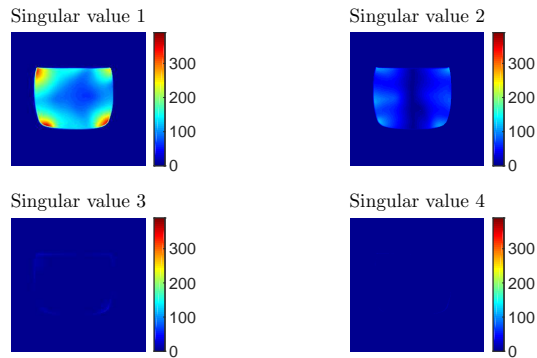


(b)

Figure 6.15: SVD of SNR maps with the Butler matrix: (a) Loaded and (b) $\min(\tilde{S})$.



(a)



(b)

Figure 6.16: SVD of SNR maps with the Butler matrix: (a) $\min(\text{loss})$ and (b) $\max(\text{P2L})$.

Comparison of individual vs. multi port matching of MRI array

Previously, it was established that single layer per-port reflection minimization is beneficial when re-matching a loaded array. Similarly, array matching is also beneficial when using prior knowledge of its sub-systems and optimizing for the full S-matrices. Although the two strategies differ largely in terms of hardware and logic, it is imperative to compare them for their outcome. The comparisons are performed in terms of B_1^+ and SNR maps.

Figure 6.17 depicts the comparison between the B_1^+ maps for the two cases. The single layer method performs better than the best performing method of array matching. There is a difference of -14.07 % on the average B_1^+ unit in the sample. Nevertheless, the large standard deviation of 21.76 % reduces the confidence to draw conclusions. The improvement between the loaded case and the min(loss) optimization for the array matching is larger than the improvement between the unmatched and the matched case of the single layer matching. However, their initial matching conditions, which are attributed to the strength of the improvement, cannot be compared as they constitute different matching states. In the SNR maps, the result is in accordance with the one for the B_1^+ map. Array matching for min(loss) changes by -1.23 % compared to the conventional single layer matching method and standard deviation is 36.84 %. The histogram of the SNR map is multi-modal, with a clear mode of pixels that improve and another where they present losses. The areas where pixels gain or lose are indicated in the map of the percentage change as well. The results are summarized in Table 6.4. The fact that the former larger improvement does not outperform the single layer matching in total indicates that a loss mechanism other than coupling is present. The standing waves present in the matching network are assumed to cause the weakness of the array matching in comparison to the single layer matching.

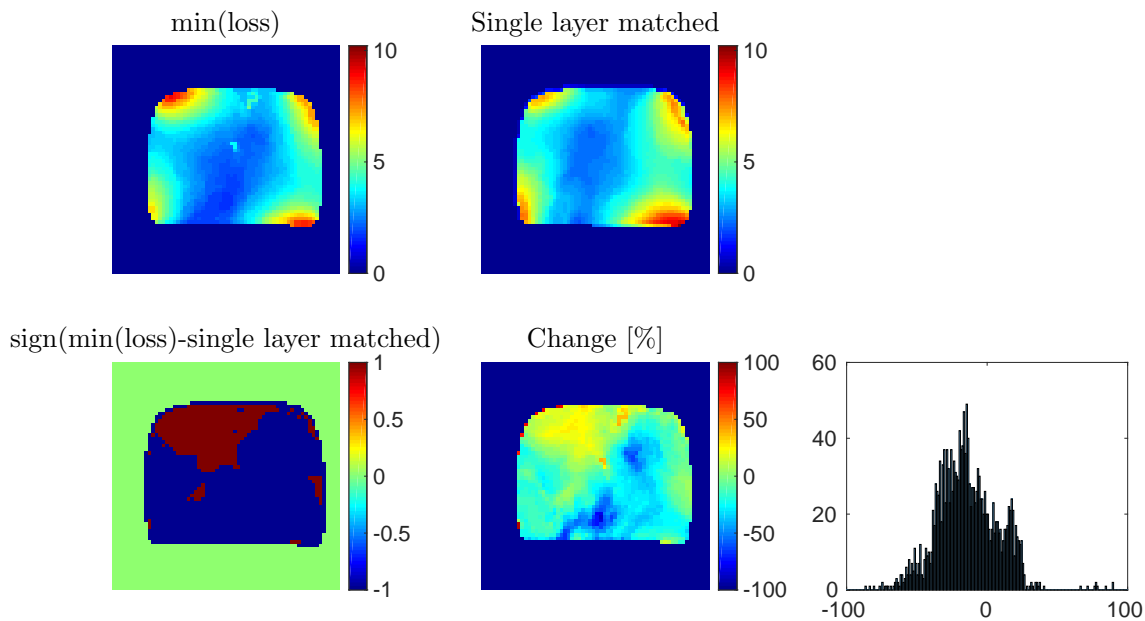


Figure 6.17: Comparison of B_1^+ maps for the single stage per-channel matching vs. the best result (minimum losses) with the Butler matrix.

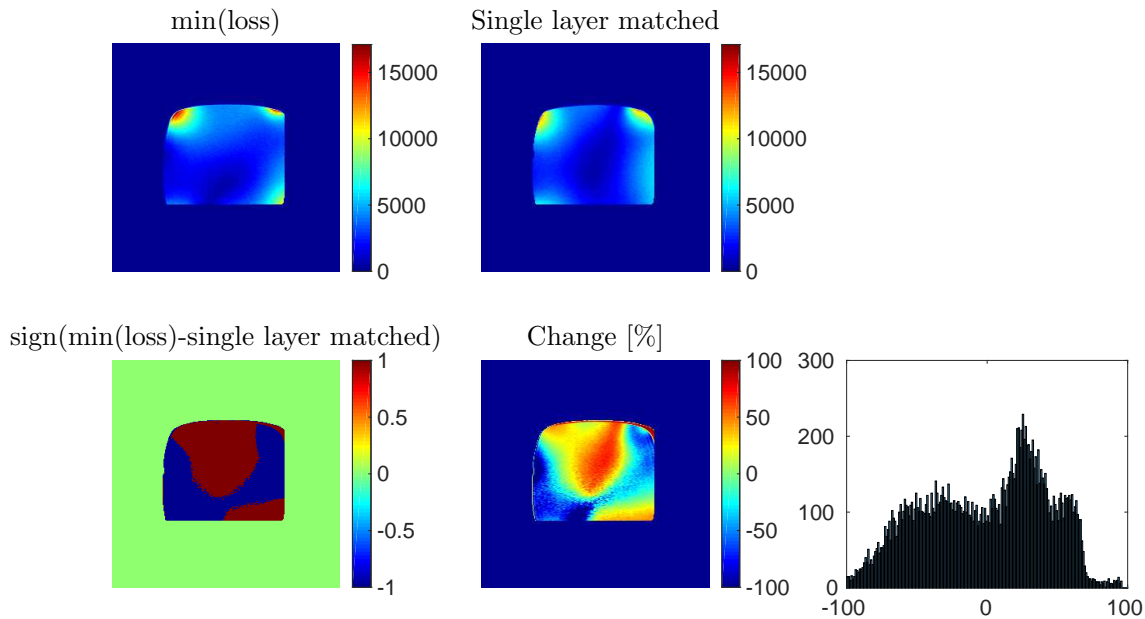


Figure 6.18: Comparison of SNR maps for the single stage per-channel matching vs. the best result (minimum losses) with the Butler matrix.

	Mean change [%]	Median change [%]	SD of change [%]
B_1^+	-14.07	-15.64	21.76
SNR	-1.23	4.93	36.84

Table 6.4: Percentage change of the B_1^+ and the SNR from the matched single layer to the array matching for the minimum losses optimization.

6.2 Discussion & Conclusion

The present work explores several approaches for optimal matching by introducing prior knowledge for the sub-systems of the matching system in the form of the lookup tables. This knowledge is fed to an algorithm in order to perform matching with different criteria. The comparison with the conventional method of matching proved that there are still aspects to be tackled with.

The algorithm introduces randomization in order to cope with the dimensionality of the search space. Every random initialization of the matching problem is subsequently solved for a series of local optimizations in a deterministic manner. The problems are computationally manageable and they result in a local optimum. The global optimum is always found aided by the random input of the algorithm.

All matching strategies perform as expected compared to the initial loaded case, which serves as a benchmark for the improvement of every method. The comparison between the methods of *minimum losses* and *maximum power to the load* shows that the results are very close for a conclusive winner. The latter is outperformed due to the pronounced losses after the assembly of the matching system. Nevertheless, the method is beneficial in cases where focus of B_1^+ on specific areas in the sample is required. Moreover, the individual

channel results show that a largely reflecting channel proves beneficial for the total array matching, as observed by the B_1^+ maps.

The array matching by accounting for all sub-components of the system is proven to perform in agreement with the expectations under practical loading scenarios. Similar conclusions are drawn for the conventional way of reflectionless matching at the input of the system. Hence, both matching practices offer gains when applied. It remains an open question how losses in the matching network for the specific implementation affect the total matching efficiency and whether a better matching network implementation would present gains.

Chapter 7

Discussion

The trend towards ultra-high field MRI and its close symbiosis with coil arrays in order to mitigate the effects of shortened wavelength impose the need for a mechanism that counteracts the changes of the varying loading conditions. Concerning the transmitter, working with the coil array imperfections, such as coupling, facilitates its wider practicality and easier adoption, while loosening the constraints applied to other engineering disciplines, such as array design, where element decoupling is a strong requirement. The present work enables adaptive matching for multiple channel transmitters in MRI, with the goal of boosting the performance of transmit coil arrays. Regarding the engineering approach, a generalized framework is adopted, where no restricting assumptions were made for the underlying MR experiment.

In terms of applicability, the modular system designed lies in the core of the transmit apparatus, making it a practical extension not only for future instrumentation, but for the existing hardware as well. The methods developed are pertinent to any MR modality that requires increased efficiency or accurate modeling of its transmission path. While, for the purposes of the present work, the scope was narrowed to the investigation of power transmission or reflection and loss, further optimization schemes are open for exploration.

In order to fulfill the requirements, the necessary means were developed. An adaptive variable capacitor module was designed and fabricated, addressing the in-bore robust operability for the high-power output of the amplifiers with low losses. The inclusion of the closed-loop controlled positioning allowed for accurate reproduction of the desired impedance selection, empowered by its electrical pre-characterization through the stored lookup tables. The implemented single channel matching algorithm was verified for various loading scenarios, thus establishing the basis for the scaling of the setup towards the multiple channel case.

In this regard, new material and method requirements emerged; inter-element coupling was dealt by means of variability on the matching network side. Furthermore, the problem's dimensionality required a well engineered choice for reduction in order to successfully match a multiple coil array. The prerequisite of coupling coefficients controllability by the matching network and the circulant property of the circular coil array triggered the introduction of the Butler matrix. The matrix blends the contributions of the individual two-port matching networks into a scheme, where they are capable of concurrently influencing all scattering coefficients of the S-matrices. The latter feature is related to the explosion of problem dimensionality by the multiplication of the instrumentation. Furthermore, the single channel algorithm required modifications in order to cope with the computationally intractable search space. In this context, it was imperative to examine the behavior of the objective functions and measure their matching and algorithmic performance. Ultimately, the multiple port matching network was implemented, serving as a test bed for verifying the initial hypothesis of multiple channel matching profitability, reflected in the results.

The practicality of the present work concerns the cases where the loading condition varies either in the course of a single MR scan, correcting for impedance changes caused by motion or systematic

thermal drifts or, even, between different experiments aiming for the optimum match in a patient-specific case.

Outlook

From a research perspective, key aspects for future exploration and experimentation concern the suppression of losses in the matching network. For validating the hypothesis regarding the losses responsible for the lower array performance as compared to the single layer matching, the answer to this question is substantial. To address this problem, a Butler matrix tailored for the problem could be designed and implemented. In view of the possible improvements by the losses' elimination, the limitation in terms of adaptivity may be considered. More complex matching network topologies and matching network designs could be tested.

In this regard, limiting factors of the matching network designs and topologies could be considered. Whether higher sophistication and complexity in the seek for a generic solution or a simple tailored approach for a specific problem is the more suitable way, is an open question. Error propagation in a complex network is another key aspect. Taking into account the error, stability issues tied with the inversion of the scattering matrices could be resolved.

In the same vein, further algorithmic flavors for boosting the performance are vital towards validation of matching systems. From mapping the behavior of the matching algorithm to applying training algorithms for valid inputs, the algorithmic playground is vast. Logging the algorithmic steps and analyzing them in a post-processing step could reveal patterns that enhance matching performance. Likewise, training the algorithm could boost its speed and accuracy by a significant amount.

Finally, integration issues to streamline operation for non-experts

could be addressed. Akin enhancements are certain to pave the way towards the adoption of transmit matching systems.

Appendix

A.1 Circulant matrices

The following mathematical treatment can be found in more rigorous fashion in [62]. It is repeated here for the reader's convenience.

Definition 1. *Circulant matrix of order n is a square matrix of the form*

$$C = \text{circ}(c_1, c_2, \dots, c_n) = \begin{bmatrix} c_1 & c_2 & \cdots & c_n \\ c_n & c_1 & \cdots & c_{n-1} \\ \vdots & \vdots & \ddots & \vdots \\ c_2 & c_3 & \cdots & c_1 \end{bmatrix}. \quad (\text{A.1})$$

The elements of each row of a circulant matrix are identical to the elements of the previous row, shifted by one position to the right and wrapped around.

Definition 2. *Permutation matrix of order n is a matrix obtained by permuting the rows of the identity matrix I_n according to some permutation of the numbers one to n . Hence, every row and every column contains a single 1, with zeros everywhere else.*

Among all permutation matrices, the matrix

$$\pi = \begin{bmatrix} 0 & 1 & 0 & \cdots & 0 \\ 0 & 0 & 1 & \cdots & 0 \\ \vdots & \vdots & \vdots & \ddots & \vdots \\ 1 & 0 & 0 & \cdots & 0 \end{bmatrix} \quad (\text{A.2})$$

plays a fundamental role in the theory of circulants. It is the matrix that defines the forward shift permutation. By induction, it follows that

$$\pi^n = I. \quad (\text{A.3})$$

Definition 3. Now, let n be a positive integer. From Euler's formula we set

$$\omega = e^{\frac{2\pi i}{n}} = \cos \frac{2\pi}{n} + i \sin \frac{2\pi}{n}, \quad \text{with } i = \sqrt{-1}. \quad (\text{A.4})$$

Definition 4. We call Fourier matrix the $n \times n$ square matrix F_n given by

$$\begin{aligned} F^* &= \frac{1}{\sqrt{n}} (\omega^{i-1} \omega^{j-1}) = \\ &= \frac{1}{\sqrt{n}} \begin{bmatrix} 1 & 1 & 1 & \dots & 1 \\ 1 & \omega & \omega^2 & \dots & \omega^{n-1} \\ 1 & \omega^2 & \omega^4 & \dots & \omega^{2(n-1)} \\ \vdots & \vdots & \vdots & \ddots & \vdots \\ 1 & \omega^{n-1} & \omega^{2(n-1)} & \dots & \omega^{(n-1)(n-1)} \end{bmatrix}. \end{aligned} \quad (\text{A.5})$$

For the Fourier matrix the following important identities hold

$$\begin{aligned} F &= F^T \\ F^* &= (F^*)^T = \bar{F} \\ F &= \bar{F}^* \\ FF^* &= F^*F = I \\ F\bar{F}^T &= \bar{F}^TF = I \\ F^{-1} &= F^* \\ F^{-1} &= \bar{F}^T. \end{aligned}$$

Definition 5. Let n be a positive integer and

$$\Omega = (\Omega_n) = \text{diag}(1, \omega, \omega^2, \dots, \omega^{n-1}). \quad (\text{A.6})$$

Theorem 1.

$$\pi = F^* \Omega F. \quad (\text{A.7})$$

Proof. From A.5, the j -th row of F^* is

$$F^* = (1/\sqrt{n})[\omega^{(j-1)0}, \omega^{(j-1)1}, \dots, \omega^{(j-1)(n-1)}].$$

Hence the j -th row of $F^* \Omega$ is

$$F^* \Omega = (1/\sqrt{n})[\omega^{(j-1)r} \cdot \omega^r] = (1/\sqrt{n})[\omega^{jr}],$$

with $r \in [0, 1, \dots, n-1]$. The k -th column of F is $(1/\sqrt{n})[\omega^{-(k-1)r}]$, with $r \in [0, 1, \dots, n-1]$. Thus, the (j, k) -th element of $F^* \Omega F$ is

$$\begin{aligned} \frac{1}{n} \sum_{r=0}^{n-1} \omega^{jr} \omega^{-(k-1)r} &= \frac{1}{n} \sum_{r=0}^{n-1} \omega^{r(j-k+1)} = \\ &= \begin{cases} 1 & \text{if } j = k - 1, \\ 0 & \text{if } j \neq k - 1, \end{cases} \quad \text{mod } n. \end{aligned} \quad (\text{A.8})$$

□

Then it follows that

Theorem 2. *If C is circulant, it is diagonalized by F .*

A.2 Simulation statistics of individual capacitors

Mean value	Cap.1	Cap.2	Cap.3	Cap.4	Cap.4	Cap.6	Cap.7	Cap.8
$\min(\tilde{S})$	86.9971	80.7026	103.8050	98.0912	53.5628	101.8267	84.6237	63.6291
$\min(\text{loss})$	76.8614	116.2529	145.6258	122.5927	140.5276	111.9776	114.5295	106.0821
$\max(\text{P2L})$	119.0416	113.4305	87.2480	80.2995	62.0530	108.2600	119.5425	78.1893
	Cap.9	Cap.10	Cap.11	Cap.12	Cap.13	Cap.14	Cap.15	Cap.16
	124.2946	98.0470	72.4864	54.2934	99.5263	80.6080	74.5572	50.4646
	145.2561	136.2834	139.6168	97.5652	121.0674	97.6707	115.7209	137.8120
	141.5619	77.7638	100.8116	65.8652	137.8060	112.9261	76.2959	76.2544
Median value	Cap.1	Cap.2	Cap.3	Cap.4	Cap.4	Cap.6	Cap.7	Cap.8
$\min(\tilde{S})$	71	73	87	85	30	87	62	47
$\min(\text{tr}(I - (S^{\text{MN}})^H S^{\text{MN}}))$	62	111	147	112	141	96	103	91
$\max(\text{P2L})$	106	103	71	76	52	97	107	61
	Cap.9	Cap.10	Cap.11	Cap.12	Cap.13	Cap.14	Cap.15	Cap.16
	116	80	52	47	81	65	59	38
	147	131	137	78	112	82	112	137
	139	74	87	56	136	119	73	58
Standard deviation	Cap.1	Cap.2	Cap.3	Cap.4	Cap.4	Cap.6	Cap.7	Cap.8
$\min(\tilde{S})$	69.4775	56.6110	77.2282	72.8255	60.2176	76.7252	73.8130	58.3271
$\min(\text{loss})$	62.9980	79.3184	86.6940	82.8748	85.3981	82.4448	83.3103	79.6489
$\max(\text{P2L})$	82.5969	78.4566	62.7543	51.7485	47.9702	77.5183	86.6032	68.4013
	Cap.9	Cap.10	Cap.11	Cap.12	Cap.13	Cap.14	Cap.15	Cap.16
	82.4754	74.4011	63.4969	41.6639	78.5289	62.2162	62.8414	48.9378
	86.2520	85.0170	87.8348	80.0171	83.6765	74.0148	80.5825	86.0642
	86.0447	49.9495	72.0853	53.3980	86.3187	87.1583	50.1051	68.3028

Table A.1: The mean value, median value and standard deviation for the individual capacitors for all methods. The table summarizes the box plots in Figure 5.16.

Notation and abbreviations

A^T	Transpose of matrix A
\bar{A}	Conjugate matrix A
A^* or A^H	Conjugate (or Hermitian) transpose of matrix A
$tr(A)$	Trace of matrix A
$diag(A)$	Diagonal of matrix A
F	Fourier matrix
I or I_n	Identity matrix of dimension n
S	An S-matrix
s_{ij}	Element i, j of S-matrix S
ϵ	Dielectric constant
γ	Gyromagnetic ratio; for $^1\text{H}=267.513 \cdot 10^6 \text{ rad s}^{-1} \text{ T}^{-1}$
Γ	Reflection coefficient
λ	Wavelength at frequency of interest
BNC	Bayonet Neill–Concelman connector
DUT	Device under test
FFE	Fast Field Echo imaging technique
FFT	Fast Fourier transform
fMRI	Functional MRI
FOV	Field of view
FR4	Grade designation assigned to PCB
MN	Matching network
minMag	Optimize for minimum reflection at the input of MN
MRI	Magnetic resonance imaging

MRS	Magnetic resonance spectroscopy
NMR	Nuclear magnetic resonance
P2L	Optimize for maximum Power-to-the-Load
PCB	Printed circuit board
PMMA	Poly(methyl methacrylate) or acrylic glass
Q	Quality factor
RF	Radiofrequency
ROI	Region of interest
Rx	Receive
SAR	Specific absorption ratio
SHS	Optimize for minimum losses in the MN
SMA	SubMiniature version A connector
SNR	Signal to noise ratio
SVD	Singular value decomposition
SWR	Standing wave ratio
TE	Echo time
TR	Repetition time
TTL	Transistor–transistor logic pulses
Tx	Transmit
Z_i	Complex impedance of device i

List of Figures

2.1	Lumped-element model of a piece of a transmission line.	15
2.2	Conjugate matching condition	21
2.3	Single channel matching network topologies	22
2.4	Coupling mechanisms when array element E_A transmits and E_B remains passive.	24
3.1	Single capacitor	32
3.2	View of the capacitor module	33
3.3	Dielectric slabs and floating electrode	34
3.4	Picture of the piezoelectric actuators	36
3.5	Capacitor range and reproducibility	46
3.6	Losses of the matching network	47
3.7	Load range matchable from the matching network	48
3.8	Single coil element	49
3.9	Reflection coefficient under different loading conditions <i>without</i> analytical calculation	50
3.10	Reflection coefficient under different loading conditions <i>emphwith</i> analytical calculation	50
3.11	Speed of the matching algorithm	51
3.12	Phantom experimental results	52

3.13	<i>in-vivo</i> B_1^+ maps and images	53
3.14	Histograms for the <i>in-vivo</i> experimental results	54
4.1	Schematic of the multiple channel setup	60
4.2	Coil array used in the experiments	61
4.3	Butler matrix	65
4.4	Multiple channel S-matrices	69
5.1	Roughness of the S-parameters at the input of the matching system for the full span of two random capacitors of an initially manually matched <i>unloaded</i> coil.	81
5.2	Roughness of the S-parameters at the input of the matching system for the full span of two random capacitors of an initially manually matched <i>loaded</i> coil.	82
5.3	Roughness of the S-parameters at the input of the matching system for the full span of two random capacitors arbitrarily positioned for the <i>unloaded</i> coil.	84
5.4	Roughness the of S-parameters at the input of the matching system for the full span of two random capacitors arbitrarily positioned for the <i>loaded</i> coil.	85
5.5	Roughness of min(loss) initially matched	87
5.6	Roughness of min(loss) for random position	88
5.7	Roughness of the diagonal elements of the matrix P^c (unloaded)	91
5.8	Roughness of the diagonal elements of the matrix P^c (loaded)	92
5.9	Roughness of $\text{tr}(X^H X) - \text{tr}(X^H (S^c)^H S^c X)$	93
5.10	Histograms for the <i>minimum reflection</i> optimization	95

5.11	Histograms for the <i>minimum losses</i> optimization . . .	96
5.12	Histograms for the <i>maximum power to the load</i> optimization	97
5.13	Scatter plot of the Euclidean distance for <i>minimum reflection</i>	99
5.14	Scatter plot of the Euclidean distance for <i>minimum losses</i>	100
5.15	Scatter plot of the Euclidean distance for <i>maximum power to the load</i>	101
5.16	Difference of initial and final position vector	102
5.17	Termination step of the sub-space exhaustive search	103
6.1	Total maps of single layer matching	109
6.2	Single layer: Channel 1 contribution	111
6.3	Single layer: Channel 2 contribution	112
6.4	Single layer: Channel 3 contribution	113
6.5	Single layer: Channel 4 contribution	114
6.6	SVD of SNR maps for single layer matching	115
6.7	Comparisons of total maps for array matching	117
6.8	Pairwise comparison of total B_1^+ maps	118
6.9	Comparisons of SNR maps of the array matching. . .	120
6.10	Coupling coefficients after rematching	123
6.11	Multi-channel matching: Channel 1 contribution . .	125
6.12	Multi-channel matching: Channel 2 contribution . .	126
6.13	Multi-channel matching: Channel 3 contribution . .	127
6.14	Multi-channel matching: Channel 4 contribution . .	128

6.15	SVD of SNR maps with the Butler matrix: (a) Loaded and (b) $\min(\tilde{S})$	129
6.16	SVD of SNR maps with the Butler matrix: (a) $\min(\text{loss})$ and (b) $\max(\text{P2L})$	130
6.17	Comparison of B_1^+ maps for the single stage per-channel matching vs. the best result (minimum losses) with the Butler matrix.	132
6.18	Comparison of SNR maps for the single stage per-channel matching vs. the best result (minimum losses) with the Butler matrix.	133

List of Tables

5.1	Statistical analysis of the termination step.	104
6.1	Percentage change of the B_1^+ and the SNR from the unmatched to the matched case.	108
6.2	Statistical analysis of the percentage change of the B_1^+ in array matching.	119
6.3	Statistical analysis of the percentage change of the SNR in array matching.	121
6.4	Percentage change of the B_1^+ and the SNR from the matched single layer to the array matching for the minimum losses optimization.	134
A.1	Individual capacitor statistics	144

Bibliography

- [1] F. Bloch. Nuclear induction. *Phys. Rev.*, 70(7-8):460–474, Oct 1946.
- [2] E. M. Purcell, H. C. Torrey, and R. V. Pound. Resonance absorption by nuclear magnetic moments in a solid. *Physical review*, 69(1-2):37, 1946.
- [3] P. C. Lauterbur. Image formation by induced local interactions: Examples employing nuclear magnetic resonance. *Nature*, 242(5394):190–191, Mar 1973.
- [4] P. Mansfield and P. K. Grannell. Nmr 'diffraction' in solids? *Journal of Physics C: Solid State Physics*, 6(22):L422, 1973.
- [5] P. Mansfield. Multi-planar image formation using nmr spin echoes. *Journal of Physics C: Solid State Physics*, 10(3):L55, 1977.
- [6] Anil Kumar, Dieter Welti, and Richard R Ernst. Nmr fourier zeugmatography. *Journal of Magnetic Resonance (1969)*, 18(1): 69 – 83, 1975.
- [7] P. Veldrine, G. Gilgrass, G. Aubert, J. Belorgey, C. Berriaud, A. Bourquard, P. Bredy, A. Donati, O. Dubois, F. P. Juster, H. Lannou, F. Molinié, M. Nusbaum, F. Nunio, A. Payn, L. Quettier, T. Schild, L. Scola, A. Sinanna, and V. Stepanov. Iseult/inumac whole body 11.7 t mri magnet. *IEEE Transactions on Applied Superconductivity*, 25(3):1–4, June 2015.

-
- [8] Organisation for Economic Co-operation and Development (OECD). Magnetic resonance imaging (mri) units (indicator). doi: 10.1787/1a72e7d1-en, 2016. [Online; accessed on 27 July 2016].
- [9] T. C. Cosmus and M. Parizh. Advances in whole-body mri magnets. *IEEE Transactions on Applied Superconductivity*, 21(3):2104–2109, June 2011.
- [10] J. T. Vaughan, M. Garwood, C. M. Collins, W. Liu, L. De-laBarre, G. Adriany, P. Andersen, H. Merkle, R. Goebel, M. B. Smith, and K. Ugurbil. 7t vs. 4t: Rf power, homogeneity, and signal-to-noise comparison in head images. *Magnetic Resonance in Medicine*, 46(1):24–30, 2001.
- [11] U. Katscher, P. Börnert, C. Leussler, and Johan S. Van Den Brink. Transmit sense. *Magnetic Resonance in Medicine*, 49(1):144–150, 2003.
- [12] Y. Zhu. Parallel excitation with an array of transmit coils. *Magnetic Resonance in Medicine*, 51(4):775–784, 2004.
- [13] Gregor Adriany, Van de Moortele, Florian Wiesinger, Steen Moeller, John P Strupp, Peter Andersen, Carl Snyder, Xiaoliang Zhang, Wei Chen, Klaas P Pruessmann, et al. Transmit and receive transmission line arrays for 7 tesla parallel imaging. *Magnetic resonance in medicine*, 53(2):434–445, 2005.
- [14] M. H. Levitt. *Spin Dynamics: Basics of Nuclear Magnetic Resonance*. Wiley, 2nd edition, 2008.
- [15] M. A. Bernstein, K. F. King, and X. J. Zhou. *Handbook of MRI Pulse Sequences*. Elsevier Science, 2004.
- [16] D. I. Hoult. The principle of reciprocity in signal strength calculations — a mathematical guide. *Concepts in Magnetic Resonance*, 12(4):173–187, 2000.

- [17] International Electrotechnical Commission (IEC). Medical electrical equipment - part 2-33: Particular requirements for the basic safety and essential performance of magnetic resonance equipment for medical diagnosis. International Standard IEC 60601-2-33:2010+A1:2013+A2:2015, IEC, Geneva, CH, 2010.
- [18] D. O. Brunner and K. P. Pruessmann. B1+ interferometry for the calibration of rf transmitter arrays. *Magnetic Resonance in Medicine*, 61(6):1480–1488, 2009.
- [19] J. D. Kraus and D. A. Fleisch. *Electromagnetics: With Applications*. McGraw-Hill series in electrical and computer engineering. WCB/McGraw-Hill, 1999.
- [20] R. E. Collin. *Foundations for Microwave Engineering*. IEEE Press Series on Electromagnetic Wave Theory. Wiley, 2001.
- [21] D. M. Pozar. *Microwave Engineering*. Wiley, 2004.
- [22] J. Dobrowolski. *Microwave Network Design Using the Scattering Matrix*. Artech House microwave library. Artech House, 2010.
- [23] S. J. Orfanidis. *Electromagnetic Waves and Antennas*. Dover, Piscataway, NJ, electronic edition, 2002. URL <http://www.ece.rutgers.edu/~orfanidi/ewa/>.
- [24] B. A. Mishustin. Synthesis of a reactive multiport network using a given scattering matrix. *Radiophysics and Quantum Electronics*, 11(12):1085–1090, 1968.
- [25] B. Widrow and E. Manteu. Adaptive antenna systems. *Proceedings of the IEEE*, 55(12):2143, 1967.
- [26] I. Gupta and A. Ksienski. Effect of mutual coupling on the performance of adaptive arrays. *IEEE Transactions on Antennas and Propagation*, 31(5):785–791, 1983.

- [27] H. Steyskal and J. S. Herd. Mutual coupling compensation in small array antennas. *IEEE Transactions on Antennas and Propagation*, 38:1971–1975, 1990.
- [28] Krishna M Pasala and Edward M Friel. Mutual coupling effects and their reduction in wideband direction of arrival estimation. *IEEE Transactions on Aerospace and Electronic Systems*, 30(4):1116–1122, 1994.
- [29] Yoon-Won Kang and David Pozar. Correction of error in reduced sidelobe synthesis due to mutual coupling. *IEEE transactions on antennas and propagation*, 33(9):1025–1028, 1985.
- [30] Peter B Roemer, William A Edelstein, Cecil E Hayes, Steven P Souza, and OM Mueller. The nmr phased array. *Magnetic resonance in medicine*, 16(2):192–225, 1990.
- [31] J. Andersen and H. Rasmussen. Decoupling and descattering networks for antennas. *Antennas and Propagation, IEEE Transactions on*, 24(6):841 – 846, Nov 1976.
- [32] R. F. Lee, R. O. Giaquinto, and C. J. Hardy. Coupling and decoupling theory and its application to the mri phased array. *Magnetic Resonance in Medicine*, 48(1):203–213, 2002.
- [33] Z. Mahmood, B. Guerin, B. Keil, E. Adalsteinsson, L. L. Wald, and L. Daniel. Design of a robust decoupling matrix for high field parallel transmit arrays. In *Proceedings of the 22nd Annual Meeting and Exhibition of ISMRM, Milan, Italy*, 2014.
- [34] F. David Doty, George Entzminger, Jatin Kulkarni, Kranti Pamarthy, and John P. Staab. Radio frequency coil technology for small-animal mri. *NMR in Biomedicine*, 20(3):304–325, 2007.
- [35] Jacco A. de Zwart, Patrick J. Ledden, Peter Kellman, Peter van Gelderen, and Jeff H. Duyn. Design of a sense-optimized

- high-sensitivity mri receive coil for brain imaging. *Magnetic Resonance in Medicine*, 47(6):1218–1227, 2002.
- [36] Y. Sun and J. K. Fidler. High-speed automatic antenna tuning units. In *Antennas and Propagation, 1995., Ninth International Conference on (Conf. Publ. No. 407)*, pages 218–222 vol.1, Apr 1995.
- [37] S. M. Sohn, J. T. Vaughan, and A. Gopinath. Auto-tuning of the rf transmission line coil for high-fields magnetic resonance imaging (mri) systems. In *Microwave Symposium Digest (MTT), 2011 IEEE MTT-S International*, pages 1–4, June 2011.
- [38] T. L. Muftuler, G. Gulsen, K. D. Sezen, and O. Nalcioglu. Automatic tuned mri rf coil for multinuclear imaging of small animals at 3t. *Journal of magnetic resonance (San Diego, Calif. : 1997)*, 155(1):39–44, March 2002.
- [39] W. C. E. Neo, Y. Lin, X. D. Liu, L. C. N. De Vreede, L. E. Larson, M. Spirito, M. J. Pelk, K. Buisman, A. Akhnoukh, A. De Graauw, and L. K. Nanver. Adaptive multi-band multi-mode power amplifier using integrated varactor-based tunable matching networks. *IEEE Journal of Solid-State Circuits*, 41(9):2166–2176, Sept 2006.
- [40] M. Pavan. *Adaptive detector matching for SNR optimization in MRI*. PhD dissertation, ETH Zurich, 2015. Diss., Eidgenössische Technische Hochschule ETH Zürich, Nr. 22624.
- [41] F. Hwang and D. I. Hoult. Automatic probe tuning and matching. *Magnetic Resonance in Medicine*, 39(2):214–222, 1998.
- [42] Graeme A. Keith, Christopher T. Rodgers, Aaron T. Hess, Carl J. Snyder, J. Thomas Vaughan, and Matthew D. Robson. Automated tuning of an eight-channel cardiac transceive array

- at 7 tesla using piezoelectric actuators. *Magnetic Resonance in Medicine*, 73(6):2390–2397, 2015.
- [43] Florian Wiesinger, Pierre-Francois Van de Moortele, Gregor Adriany, Nicola De Zanche, Kamil Ugurbil, and Klaas P. Pruessmann. Parallel imaging performance as a function of field strength—an experimental investigation using electrodynamic scaling. *Magnetic Resonance in Medicine*, 52(5):953–964, 2004.
- [44] T. J. Vaughan, H. P. Hetherington, J. O. Otu, J. W. Pan, and G. M. Pohost. High frequency volume coils for clinical nmr imaging and spectroscopy. *Magnetic Resonance in Medicine*, 32(2):206–218, 1994.
- [45] Q. X. Yang, J. Wang, X. Zhang, C. M. Collins, M. B. Smith, H. Liu, X. Zhu, T. J. Vaughan, K. Ugurbil, and W. Chen. Analysis of wave behavior in lossy dielectric samples at high field. *Magnetic Resonance in Medicine*, 47(5):982–989, 2002.
- [46] Thomas K. F. Foo, Cecil E. Hayes, and Yoon-Won Kang. An analytical model for the design of rf resonators for mr body imaging. *Magnetic Resonance in Medicine*, 21(2):165–177, 1991.
- [47] T. S. Ibrahim, C. Mitchell, P. Schmalbrock, R. Lee, and D. W. Chakeres. Electromagnetic perspective on the operation of rf coils at 1.5–11.7 tesla. *Magnetic Resonance in Medicine*, 54(3):683–690, 2005.
- [48] K. P. Pruessmann, M. Weiger, M. B. Scheidegger, and P. Boesiger. Sense: Sensitivity encoding for fast mri. *Magnetic Resonance in Medicine*, 42(5):952–962, 1999.
- [49] D. K. Sodickson and W. J. Manning. Simultaneous acquisition of spatial harmonics (smash): Fast imaging with radiofrequency coil arrays. *Magnetic Resonance in Medicine*, 38(4):591–603, 1997.

- [50] M. A. Griswold, P. M. Jakob, R. M. Heidemann, M. Nittka, V. Jellus, J. Wang, B. Kiefer, and A. Haase. Generalized autocalibrating partially parallel acquisitions (grappa). *Magnetic Resonance in Medicine*, 47(6):1202–1210, 2002.
- [51] Q. X. Yang, J. Wang, C. M. Collins, M. B. Smith, X. Zhang, K. Ugurbil, and W. Chen. Phantom design method for high-field mri human systems. *Magnetic Resonance in Medicine*, 52(5):1016–1020, 2004.
- [52] J. Butler and R. Lowe. Beam-forming matrix simplifies design of electronically scanned antennas. *Electronic Design*, 9:170–173, April 1961.
- [53] C. A. Balanis and P. I. Ioannides. Introduction to smart antennas. *Synthesis Lectures on Antennas*, 2(1):1–175, 2007.
- [54] D. G. Fang. *Antenna Theory and Microstrip Antennas*. CRC Press, Inc., Boca Raton, FL, USA, 1st edition, 2009.
- [55] A. W. Rudge. *The Handbook of Antenna Design*. Number v. 1 in Electromagnetics and Radar Series. P. Peregrinus, 1982.
- [56] Y. T. Lo and S. W. Lee. *Antenna Handbook: Volume III Applications*. Antenna Handbook. Springer US, 1993.
- [57] V. Alagappan, J. Nistler, E. Adalsteinsson, K. Setsompop, U. Fontius, A. Zelinski, M. Vester, G. C. Wiggins, F.z Hebrank, W. Renz, F. Schmitt, and L. L. Wald. Degenerate mode band-pass birdcage coil for accelerated parallel excitation. *Magnetic Resonance in Medicine*, 57(6):1148–1158, 2007.
- [58] H Moody. The systematic design of the butler matrix. *IEEE Transactions on Antennas and Propagation*, 12(6):786–788, 1964.

- [59] B. Sheleg. A matrix-fed circular array for continuous scanning. *Proceedings of the IEEE*, 56(11):2016–2027, 1968.
- [60] T. M. Macnamara. Simplified design procedures for butler matrices incorporating 90° hybrids or 180° hybrids. In *IEE Proceedings H-Microwaves, Antennas and Propagation*, volume 134/1, pages 50–54. IET, 1987.
- [61] T. M. Macnamara. Positions and magnitudes of fixed phase shifters in butler matrices incorporating 90 degree hybrids. In *IEE Proceedings H-Microwaves, Antennas and Propagation*, volume 135/5, pages 359–360. IET, 1988.
- [62] P. J. Davis. *Circulant Matrices*. AMS Chelsea Publishing Series. Chelsea, 1994.

Curriculum Vitae

I was born on May 2nd, 1981, in Nea Moudania, Greece, to Nikolaos Katsikatsos and Clio Fakiri-Katsikatsou. I attended high school in Nea Moudania and received my diploma in June 1999.

From 1999 to 2000 I attended the first year at the Polytechnic School of Democritus University of Thrace, Greece, in the school of Electrical & Computer Engineering. From 2000 to 2006 I studied Electrical & Computer Engineering at the Polytechnic School of the Aristotle University of Thessaloniki, Greece, with a specialization in Electronic and Computer Engineering. My diploma thesis, carried out at the Multimedia Understanding Group and supervised by Prof. A. Delopoulos, was entitled ‘Constructing Fuzzy Relations from Word-Net for Word Sense Disambiguation’.

In 2006 I proceeded with my studies specializing in Theory of Computing at the school of Computer Science at the Swiss Federal Institute of Technology (ETH), Zurich. As of June 2008, I worked as a lab assistant at the RF laboratory of the Magnetic Resonance Technology and Methods group, ETH. In 2009, I worked on the thesis, entitled ‘Observation of Dynamics on Social Networks’, under the supervision of Prof. P. Widmayer.

In August 2009, I received the Master in Computer Science from the Swiss Federal Institute of Technology (ETH), Zurich. In September 2009, I joined the group of Prof. Klaas P. Pruessmann in Zurich as a doctoral student and research assistant.

Publications

Conference Publications

- Katsikatsos G., Pruessmann K. P., Automatic Matching of Transmit Arrays with Optically Controlled Capacitors. *In: Proc. Intl. Soc. Mag. Reson. Med., volume 22, 2014, Milan*
- Katsikatsos G., Pruessmann K. P., Closed-loop control for transmit array matching. *In: Proc. Intl. Soc. Mag. Reson. Med., volume 21, 2013, Utah*
- Katsikatsos G., Pruessmann K. P., Low-loss adjustable networks for automated matching of transmit coils. *In: Proc. Intl. Soc. Mag. Reson. Med., volume 20, 2012, Melbourne*
- Haeberlin M., Wilm B., Barmet C., Kozerke S., Katsikatsos G., Pruessmann K. P., Sinusoidal Perturbations Improve the Noise Behavior in Parallel EPI. *In: Proc. Intl. Soc. Mag. Reson. Med., volume 18, 2010, Stockholm*
- Barmet C., Wilm B. J., Pavan M., Katsikatsos G., Keupp J., Mens G., Pruessmann K. P., Concurrent Higher-Order Field Monitoring for Routine Head MRI: An Integrated Heteronuclear Setup. *In: Proc. Intl. Soc. Mag. Reson. Med., volume 18, 2010, Stockholm*

